Modelling Vegetation Demography, Disturbance, and Carbon Storage in Forests

Submitted by:

Arthur Argles

to the University of Exeter as a thesis for the degree of

Doctor of Philosophy in Mathematics

November 2021

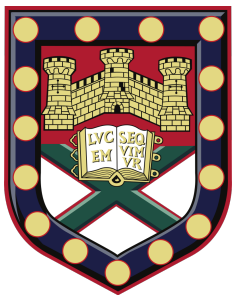

Under the supervision of:

Professor Peter Cox (University of Exeter)

I certify that all material in this thesis which is not my own work has been identified and that no material has previously been submitted and approved for the award of a degree by this or any other University.

Signature: .....

Abstract

Earth System Models (ESM) have a diverse range of approaches when representing vegetation. These differences can lead to uncertainty in inter-model projections under climate change. Plant demography has been increasingly used by Dynamic Global Vegetation Models (DGVMs) to compromise between tractability within the ESM framework against the complexity of ecosystem dynamics.

The primary goal in this thesis is to further develop a new cohort DGVM: The Robust Ecosystem Demography (RED) model. To do this, we review mathematical and modelling techniques that are used to describe the dynamics of forest demography over time.

Demographic Equilibrium Theory (DET) is the notion that the size-structure of forests can be sufficiently describe by the Metabolic Scaling Theory of growth (MST) and mortality at equilibrium. This has been validated at scale using forest inventory data in both temperate and tropical forests. The combination of DET and allometry yields functions that can explain forest properties, such as total carbon or growth density, and why such quantities are skewed towards the largest individuals.

Using the assumptions of DET as a basis, we further develop RED to include recruitment and competition. RED partitions plants into mass classes, where MST dependent growth rates and plant mortality are applied. RED requires only two inputs, total plant carbon assimilate and disturbance mortality. We split carbon assimilate by a fraction, α, into recruitment and, $1-\alpha$, into growing the plants. Using MST we disaggregate plant growth onto each class. Seedlings are constrained by the area not occupied by competing plants, with successful recruits

joining the lowest mass class. RED version 1 was driven by UKESM assimilate rates globally, and can be calibrated to find the required mortality rates to fit remotely sensed observations of plant coverage.

In RED version 2 we introduce a seed pool and improve the flux scheme, which improves the realism of regrowth. We also adjust the competition by allowing plant coverages to overlap, thereby introducing more realistic diversity into the model. We simulate secondary succession from land-use abandonment and size-dependent disturbances of drought and mortality.

Using the RED competition as a guide, we are able to build upon DET by including a competition and recruitment for the lower boundary condition. Closed-Form Demographic Equilibrium Theory (CF-DET) provides insight into how forests are dependent on both their rate of recruitment and mortality. CF-DET suggests forests may optimise certain variables, such as number density or plant height. We also use CF-DET to infer tree demography from top-down site level and remotely sensed observations.

Acknowledgements

Firstly, I would like to thank Prof Peter Cox and Dr Jon Moore, who's previous thesis led to the current RED model. They have both been enthusiastic guides and supporters during this research. Secondly, I would like to thank others who have helped in the development of RED; Dr Andy Wiltshire (who has helped integrate RED into JULES), Dr Anna Harper, Prof Chris Huntingford and Dr Chris Jones, especially in their contributions to the RED model paper. Also thanks for their help and insights with RED version 2 plant-diversity, Mathilda Hancock, Prof Stephen Sitch and Dr Lina Mercado.

Additional thanks for their assistance and/or discussions; the JPEG Mortality team (Dr Doug Kelly, Dr Chantelle Burton, Dr Karina Williams and Dr Sami Rafi (who provided the TropForC-db data)). For JULES/rose help Dr Carolina Duran Rojas, and Simon Jones (who I consider somewhat of a PhD twin) .

Finally, and by no means least, I would also like to pass on my gratitude to my Friends and Family for being so supportive throughout this journey. My parents, Peter and Anne Argles who have a non-exhaustive provisions of impromptu cream teas and dinners. My partner, Rebecca Millington, especially during the turbulence of the recent pandemic, has been incredible to this end.

Contents

List of Figures

List of Tables

Published Papers and Collaboration within the Thesis

Many of the ideas discussed within the thesis occurred through the regular supervisor meetings with Prof Peter Cox and Dr Jon Moore. While these meetings helped steer the direction of research and development, the vast bulk of the thesis is my own original work: the coupling of Demographic Equilibrium Theory and allometric relationships, RED and RED version 2 numerical model ($75,400$ lines of code), and the derivation of Closed Form Demographic Equilibrium Theory.
A list of papers that I have worked on during the PhD:

1 Argles, A. P. K., Moore, J. R., Huntingford, C., Wiltshire, A. J., Harper, A. B., Jones, C. D., and Cox, P. M. (2020). Robust Ecosystem Demography (RED version 1.0): a parsimonious approach to modelling vegetation dynamics in Earth system models. *Geoscientific Model Development*, 13(9):4067–4089

This paper describes the Robust Ecosystem Demography Dynamic Global Vegetation Model. As first author I developed the numerical model, along with the analytical equilibrium solutions, and conducted the global simulation within the paper. The paper is copied and edited for chapter 3 in this thesis.

2 Moore, J. R., Argles, A. P., Zhu, K., Huntingford, C., and Cox, P. M. (2020). Validation of demographic equilibrium theory against tree-size distributions and biomass density in Amazonia. *Biogeosciences*, 17(4):1013–1032

I collaborated with Dr Jon Moore on his work to validate Demographic Equilibrium Theory with the South American dataset (Figure 2.3 in chapter 2). This collaboration was centred on understanding the analytical solutions to the Fokker-Plank equation for forests and the implications with regards to the RED model

and Closed Form Demographic Equilibrium Theory (Chapter 5). In addition to this paper there are elements, such as the allometric theory (section 2.2.1), first produced in the original RED thesis Moore (2016).

Other areas of collaboration:

With RED version 2 we looked into improving the representation of plant diversity. This involved a modification to the competition coefficients within RED (see section 4.3). The original application of Maximum Entropy Theory of Ecology with RED was conducted in collaboration with Mathilda Hancock, a postgraduate research student at the University of Exeter. I contributed with my knowledge of the mathematics (formulation of equation (4.14)) and of the RED model. The results presented in section 4.3 are a further independent application of this theory, with Figure 4.8 being estimated from table 4.2.

1 Introduction and rational of DGVMs and Forest Demography

Rationale for Chapter

This chapter outlines the importance of interactions between the climate and vegetation. The chapter also presents a history of dynamic vegetation models up to the emergence of Dynamic Global Vegetation Models (DGVMs). We review a wide variety of DGVMs ranging from complex to simple modelling approaches, and discuss the important role plant demography may play in addressing common DGVM deficiencies. From this discussion we build objectives for the rest of the thesis.

Climate and human influences are important determinants in the geographic distribution of observed vegetation (Matthews, 1983; Brovkin et al., 1997). Yet the interaction is complex, global forests are a major carbon store and also affects the hydrological-cycle. A reduction in forest cover decreases water recycling, leading to drier regions (Betts et al., 2004). The additional loss of biomass is a source of carbon emissions and could lead to an acceleration of global warming (Cox, 2001; Friedlingstein et al., 2001). Therefore, the future climate is dependent on how global vegetation responds to the anthropocene. To model these interactions, we rely on using Dynamic Global Vegetation Models (DGVMs) within Earth System Models (ESM).

Since the emergence of the first fully couple ESM, the range and detail of biogeophysical processes included has improved significantly (Arora et al., 2020). Vegetation plays an important role in the global biogeochemical and hydrological cycle. Understanding the dynamics of forest ecosystems, how the populations of plants change through time (through fecundity, growth and mortality), will there-

fore better inform researchers and policy makers of the associated risks of anthropogenic land-use and climate change. Recent and historic dieback of forest ecosystems have resulted in losses of biodiversity (Brook et al., 2003; Sahney et al., 2010), social impacts (Olivero et al., 2017; Wright, 2017), and the release of greenhouse gases (Houghton, 2005).

It is estimated that $3.4 \pm 0.9\ \mathrm{PgC\ yr^{-1}}$ ($\pm\sigma$) of carbon was absorbed annually over the last decade by the terrestrial sink, the superset of the sinks of plants and soil (Friedlingstein et al., 2020). This sink represents almost 30% of annual anthropogenic carbon emissions, $11.5 \pm 0.9\ \mathrm{PgC\ yr^{-1}}$. Yet the terrestrial sink remains one of the most uncertain carbon sinks projected into the twenty-first century (Friedlingstein et al., 2014; Arora et al., 2020). Of the ESMs in CMIP6 (Coupled Model Intercomparison Project) that include representation of biogeochemical cycles, cumulative projected land-uptake ranged from $305\ \mathrm{PgC}$ to $1159\ \mathrm{PgC}$ by the end of the $1\mathrm{pct}\mathrm{CO}_2$ experiment[1], with the plant sink ranging being between $173\ \mathrm{PgC}$ to $569\ \mathrm{PgC}$. By comparison, the ocean sink has a much more constrained inter-model range of just $597\ \mathrm{PgC}$ to $763\ \mathrm{PgC}$. $1\mathrm{pct}\mathrm{CO}_2$ experiment does not include the additional ecological forcing of land-use change. Indeed, including land-use change through social economic scenarios could compound the uncertainty in ESM runs (Gasser et al., 2020).

Climate and land-use change could potentially cause a significant loss of regional forest ecosystems (Shukla et al., 2019). For instance, one key risk is Amazonian dieback (Cox et al., 2004; Lenton et al., 2008). Two models in the CMIP5 ensemble predicted dieback under the most extreme radiative forcing scenario (Drijfhout et al., 2015). However, the likelihood is increased when including deforestation, which reduces evapotranspiration and forest resilience to droughts (Zemp et al., 2017).

The risk of regional dieback, along with uncertainties of the climate projections, illustrate the need for more realistic modelling of vegetation. To answer how forests will respond to anthropogenic climate change requires better understanding of processes which drive change. Disturbances such as droughts and fire, the severity and frequency of which are dependent on the temperature (Dale et al.,

[1] $1\mathrm{pct}\mathrm{CO}_2$ is a controlled run where atmospheric CO2 concentration increases gradually at a rate of 1% per year from 1850 until quadrupling.

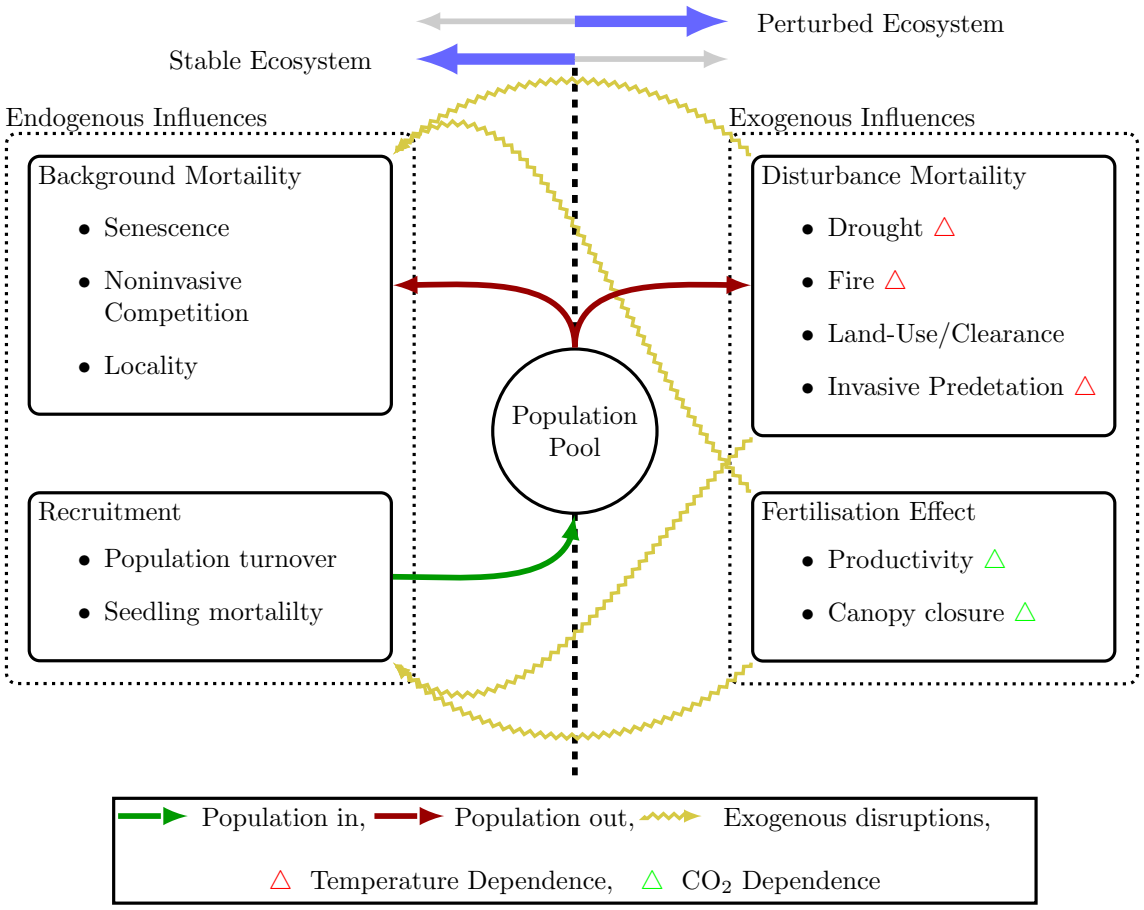

Figure 1.1: The plant ecosystem under the anthropocene. Exogenous disruptions driven by climate change could shift the equilibrium state of the system, providing a source of uncertainty within models.

2001; Dai et al., 2004), against increased growth and competition (via canopy closure; McCarthy et al. (2007)) through CO_2 fertilisation (Figure 1.1). Recently there has been a push to address these issues (Fisher et al., 2018; Burton et al., 2019; Eller et al., 2020). Such processes are heavily dependent on plant size, larger trees grow faster (West et al., 1997), yet are more vulnerable to drought (Nepstad et al., 2007; da Costa et al., 2010; Gora and Esquivel-Muelbert, 2021), while smaller trees and the understory are more at risk to fires (Brando et al., 2012; Gora and Esquivel-Muelbert, 2021). Yet the implementation of plant size or age into DGVMs and the CMIP ensemble is not widespread. Plant demography, the aggregation of plant individuals into age and/or size classes, provides a method of addressing this and allowing for significantly more complex processes to be explored (Fisher et al., 2018).

1.1 The emergence of Forest Dynamics

Forests are often described as heterogenous (Franklin and Van Pelt, 2004; Spies et al., 2006; Kane et al., 2011; Franklin et al., 2020). Complexity is especially prevalent on the subgrid scale. Stands will significantly vary in terms of demographic parameters – diversity, age, size, recruitment, competition, growth, and mortality (Sheil and May, 1996; Phillips et al., 2004; Seydack et al., 2011; Johnson et al., 2016). An important task for the realistic representation of forest response to anthropogenic change is to ask how this complexity scales with geographic scope; from the individual tree to the regional and global scale (Shugart and Smith, 1996; Strigul et al., 2008; Kane et al., 2011; Prentice et al., 2015; Shugart et al., 2020).

Historically, ecologists and geographers have strongly, sometimes even ideologically[2], debated the predictability and classifications of plant ecosystems, mainly from two perspectives (Tansley, 1935; Whittaker, 1953; Bugmann, 2001). F.E. Clements suggested in his work 'Plant Succession' that plant ecosystems would deterministically follow a successional pathway towards a stable "climax" community (Clements, 1916). The eventual composition of the forest would be dependent on the climate of the region. In a similar vein, from continental Europe emerged "Phytosociology" or the "plant society", the theory that species formed an empirical "vegetation unit" of associations dependent on the local climate (Braun-Blanquet et al., 1932). Climax and Phytosociology was challenged by ecologists such as H. Gleason. In the Gleason model, the resultant communities arose as an indeterministic combination of factors at an individual level; migration, environmental sorting and chance (Gleason, 1926). By the 1950s, Climax theory was further criticised as being subjective and not fully capturing the range of influences, while also failing to explain the "complex continuum" of plant species observed spatially (Curtis and McIntosh, 1951; Whittaker, 1953). However, there was recognition for the need of abstractions of individual complexity as a way to push development of plant community dynamics (Watt, 1947; Whittaker, 1953).

The first attempt of give a mathematical explanation of community dynamics came from A. S. Watt in 1947 (Watt, 1947; Van Der Maarel, 1996). Watt attemp-

[2]Whittaker mentions that the USSR researchers rejected the idea of equilibrium from European Phytosociology, to reconstruct it "on the bases of the methodology of Marx and Lenin (Alechin, 1946; Roussin, 1949)".

ted to address the mosaic pattern seen within seven plant communities ranging from heathland to deciduous forest. Each patch would represent a community of species in both patch age and physiology, going through different “phases” of succession. New patches arise as area cleared by mortality or litter from existing vegetation. This is to represent the opening of the canopy caused by falling branches or tree, this process is known as gap formation (Belsky and Canham, 1994). Hence a “gap” is consistent with a young patch. These ecological ideas; the vegetation unit or patches and the Gleason complexity of the individual, would lead to the first numerical models of forest dynamics in the 1960s and 70s (Bugmann, 2001).

A patch based approach was first implemented in the JABOWA (Botkin et al., 1972a,b) and FORET (Shugart and West, 1981) models. These are more commonly known as “gap models”, both simulate a grid of patches within an ecosystem on the scale of 0.01 to 0.1 hectares. Gaps are randomly formed through by disturbances, resetting the patch on its successional pathway. Other forest models sought to represent explicit individuals of tree species in three-dimensional space, to capture vertical heterogeneity, such as the SORTIE model (Pacala et al., 1993; Canham et al., 1994). Environmental variables such as temperature and precipitation drive the photosynthesis and growth of plants. Light competition is implemented using Beer’s law of radiation attenuation; the fraction of photosynthetically active radiation would decrease through the canopy exponentially (Monsi and Saeki, 1953; Hirose, 2005). Age and size are principal variables in determining mortality and competition. The reproduction or recruitment rate is either fixed from a predetermined list of species or dependent on the size of the current plant population. Gap models have proven realistic in predicting the dynamics and distributions of forests in multiple site-level studies of coniferous (Leemans and Prentice, 1987), temperate (Waldrop et al., 1986) and tropical forests (Doyle, 1981; Peng, 2000). They have also been successfully deployed for projecting forestry management yields (Munro, 1974; Mitchell, 1975; Dale et al., 1985).

In parallel, the development of computing saw the introduction of large-scale climate models. The first generation, called General Circulation Models (GCMs), included atmospheric physics (Phillips, 1956) and eventually led to coupled models of atmosphere-ocean circulation (Manabe, 1969). Concern over human impact on the Earth System (Manabe and Wetherald, 1967; Wilson and Matthews,

1971), led to further efforts to study the greenhouse effect and carbon cycle (Manabe and Wetherald, 1975). Initially, atmosphere-land interactions were rudimentary, with GCMs using prescribed values for parameters such as surface albedo, roughness and those describing simple hydrological interactions for the soil (Dorman and Sellers, 1989). Vegetation made an explicit entrance with the modelling of evapotranspiration to improve the representation of the global diurnal cycle of temperature (Dickinson, 1984). Later models would begin to prescribe vegetation types catergorised by the type of leaf and by biology (woody versus herbaceous plants), known as "Plant Functional Types" (PFTs), for example, C3 and C4 Grass or Broadleaf Deciduous Trees (Smith et al., 1993). This allowed for stomatal conductance and phenological diversity to be realistically represented (Sellers and Dorman, 1987; Leuning, 1995; Haxeltine and Prentice, 1996; Cox et al., 1998). However, there were no forest dynamics or demographics, coverage was prescribed and treated as stationary in "equilibrium" biogeographical models, such as the BIOME model (Prentice et al., 1992; Neilson, 1995).

Ecologists have long appreciated the role the climate played in the development of ecosystems (Cowles, 1899), especially on the global scale (Koppen, 1936; Holdridge, 1947). The emphasis of research into plant ecosystems has shifted to be increasingly in terms of climate change. This has led to work investigating the effects of rising temperatures such as – increased frequency of disturbance from droughts (Wigley et al., 1984; Prentice et al., 1991), fire (Clark, 1988, 1990), pests such as bark beetles (Perry and Borchers, 1990), and extreme weather (Overpeck et al., 1990). It was found that rising carbon-dioxide concentrations could lead to increased rates of CO_2 fertilisation, increasing the rate of carbon sequestration (Eamus and Jarvis, 1989; Gifford, 1993). Forest dynamics (modelling aspects such as tree size, age, mortality, reproduction) was deemed of primary importance in the next generation of climate models (Smith and Shugart, 1993). Forest dynamics had effectively moved from scale of hectares to the scale of hundreds of kilometers. This has led to the creation of a new class of ecosystem models known as Dynamic Global Vegetation Models (DGVMs) (Peng, 2000; Cramer et al., 2001; Sitch et al., 2008).

1.2 Dynamic Global Vegetation Models

There are multiple approaches to modelling plant demography at the global scale (Peng, 2000; Fisher et al., 2018). The first generation of DGVMs ranged from the representation of individual trees to simpler, area-averaged based models that represented the mean plant of a PFT. These models could be viewed as having been a propagation of the two earlier viewpoints of forest ecology: Clements determinism versus the complexity and indeterminism of Gleason. There are inherent trade-offs with both approaches. Later "intermediate-complexity" models seek to address some of the earlier issues by capturing the detail of individual based models through statistical modelling. This avoids the stochasticity of individual models, while retaining detail when compared with area-averaged models.

1.2.1 Individual Based Models

Individual based DGVMs are descendants of the original gap models. The earliest iteration of this method was the HYBRID model (Friend et al., 1993, 1997). HYBRID simulates many individual trees established from a fixed density of seeds. In line with vertical and horizontal heterogeneity these individuals would be randomly distributed across a patch. Like the gap models, crown competition for light would be explicitly represented using Beer's law. HYBRID would be driven globally using carbon, water and nitrogeon outputs from the HadCM2 GCM by subdividing each grid-cell into 10 patches (Friend and White, 2000). The SEIB-DGVM model uses a similar methodology at the global scale (Sato et al., 2007). This approach inherits the potential to capture a great number of processes in detail, resulting in very realistic modelling of small scale, site-level dynamics (Sato et al., 2010).

For practical reasons, individual based models use the process of "upscaling" from the scale of the stand to that of the land-surface grid-box. Upscaling is the process of representing detailed models at coarser resolution (Snell et al., 2014). SEIB-DGVM scales 30mx30m plots up to the order of 200kmx200km grid-boxes (Sato et al., 2007). SEIB-DGVM is coupled into the MIROC-ESM (Watanabe et al., 2011) for global climate simulations, and simulates in essence one random patch for one grid-box. Despite this, there are benefits to upscaling. It is a useful

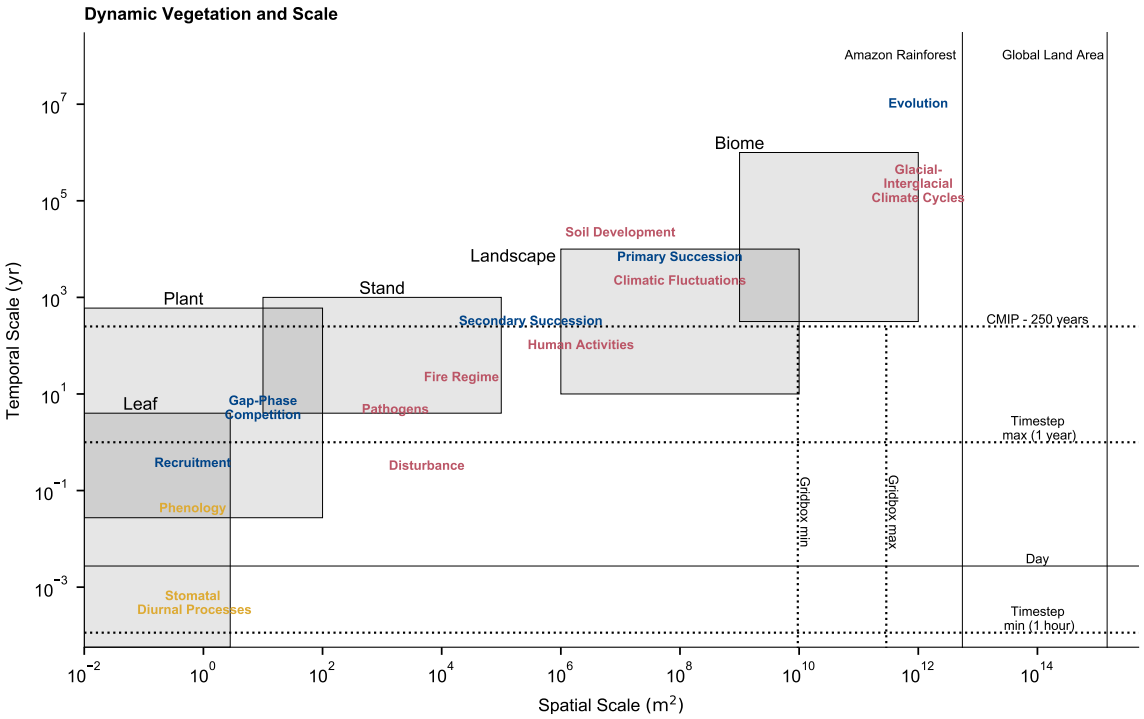

Figure 1.2: Adapted from Shugart et al. (2020), roughly illustrating how processes of dynamic vegetation scale across space and time. Grey boxes classify the biological and community scale. Yellow text describes leaf-based processes. Blue text describes endogenous processes. Red text describes exogenous disturbances and processes. Black dotted lines illustrate the spatial-temporal limits of a Land/Earth System Model with the vegetation component.

method for investigating what small scale processes are significant at the large-scale. For instance, upscailing has been used to highlight the influence of soil variation on high latitude ecosystems (Sato and Ise, 2012), or forecasting typhoon windthrow under climate scenarios in Japan (Wu et al., 2019).

Individual based models have been used to address some of the criticisms of PFTs. Plant species have a wide and diverse continuum of traits as opposed to the discreteness offered by globally implemented PFTs (Díaz and Cabido, 2001). It has been argued that PFTs underplay the resilience of forest ecosystems through the lack of biodiversity (Bellard et al., 2012; Boulangeat et al., 2012), nor do they capture the reality of environmental sorting of species and dynamics at scale (Lavorel and Garnier, 2002; Scheiter et al., 2013). Recently, individual-trait based models have been developed to address this (Fyllas et al., 2014). aDGVM2 (Scheiter et al., 2013) and LPJmL-FIT (Sakschewski et al., 2015) use stochasticity to select the traits of individual plants (carbon allocation, fecundity, etc) from a distribution gathered by huge databases such as TRY (Kattge et al.,

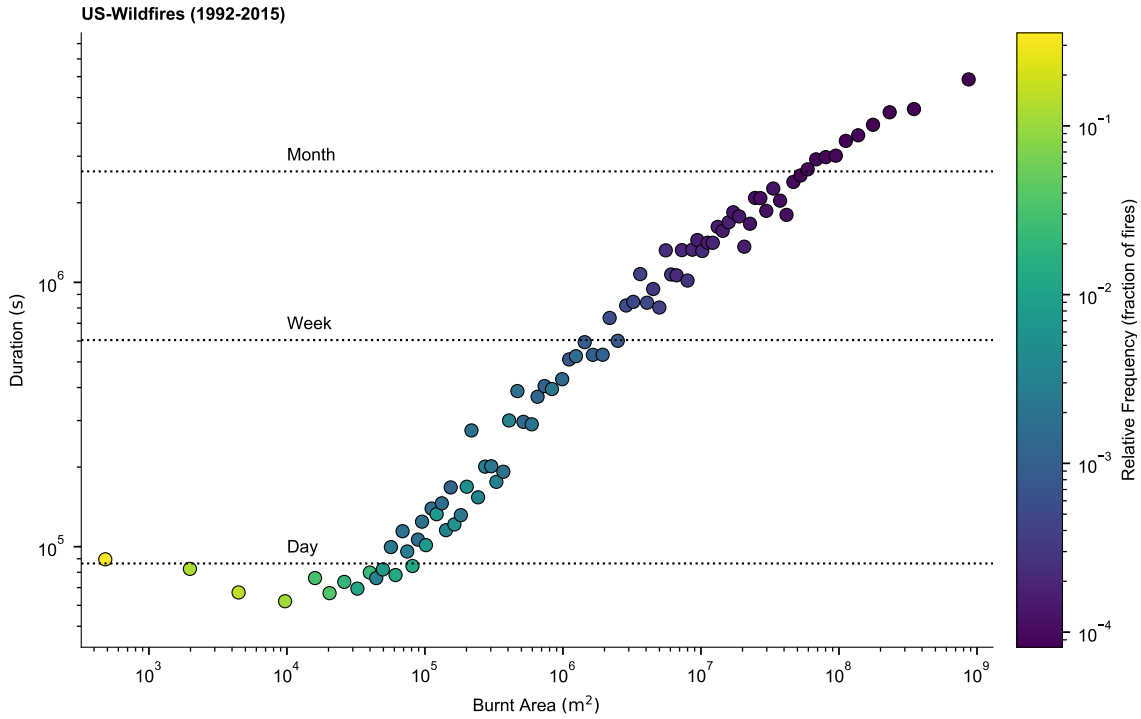

Figure 1.3: The burnt area versus duration of binned data of wildfires within the United States between 1992 and 2015. Colour-scale is indicative of relative fire frequency. For practical reasons, individual based models in ESMs cannot capture large-scale fires without relying on parametrisation. Data from the US Forest Service (Short, 2017).

2011). This method has had some success in reproducing the biodiversity observed within the Amazon rainforest (Fauset et al., 2019).

Individual based models can fail to capture many large scale dynamic processes (Figure 1.2) (Scheiter and Higgins, 2009; Shugart et al., 2020). The influence of forest fires can extend well past single patch scale. Figure 1.3 shows that over the period between 1992-2015 individual forest fires within the US could range up to $10^9 \mathrm{m}^2$, and last for months. A single fire can eliminate an entire patch, especially in savannah, within a few minutes (Rothermel, 1983). Therefore, to include fire, individual based models with a single patch must represent fire through parametrisation. SEIB-DGVM relies on a probabilistic estimation of fire based on environmental factors (Thonicke et al., 2001) at the end of each year, after which the model applies an average fire-resistant fractions on the number of individuals killed. A repeat fire cannot occur afterwards for another year. However, generally individual models that represent patches are able to explicitly simulate fire. In LPJ-GUESS in cohort and individual mode[3], fire mortality is applied daily across

[3]Uniquely, LPJ-GUESS has two modes “population mode”, which is an average-area vegetation model (see section 1.2.2), and “cohort and individual mode” which simulates multiple patches with a three dimensional simulation of trees within each patch.

multiple patches daily (100 patches per 0.1 ha in grid-box size) – removing all individuals within the patch if a fire occurs (Smith, 2001).

1.2.2 Area-averaged Models

An alternative approach to representing global vegetation focuses on the area-averaged plant. For a fraction of area within the grid-box, bio-geophysical properties can be explicitly, or implicitly, representative of the average tree, shrub, or grass. Initially, and without the earlier incarnations of the gap-models, the methodology was climax or environmentally driven, derived from the earlier simple equilibrium models already coupled into ESMs (Prentice et al., 1992).

The VECODE model (Brovkin et al., 1997), sought to represent dynamic vegetation fractions as a consequence of two climate variables – temperature and precipitation. Competition was simply between two PFTs – trees and grass, the fraction of which must always add up to one. This successfully captured the general distribution of tree coverages globally using interpreted data from Olson et al. (1985). However, this approach underplays how fast vegetation cover might change, due to the lack of physical processes such as disturbances or land-use change (Quillet et al., 2010). In an expansion to the VECODE approach, the DYNVEG model simulates PFTs with the inclusion of dynamic disturbances such as fire and windthrow (Reick et al., 2013).

The TRIFFID (Cox, 2001) and CTEM models (Arora and Boer, 2006) represent PFTs with vegetation fractions but employ explicit competition through a Lotka scheme (Freedman, 1980). In TRIFFID, vegetation tiles were simulated with area averaged productivity and carbon biomass. PFTs accumulate carbon into three pools – wood, leaves and litter. For recruitment, TRIFFID uses an LAI (Leaf-Area Index) dependent fraction of carbon mass assimilate to “spread”, or expand, the coverage. PFTs are grouped via a competitive hierarchy, where dominant PFTs (Trees) ignore the space occupied by sub-dominant PFTs (Shrubs and Grasses). The PFT competition between the trees is modelled using height estimated from allometry.

VECODE, TRIFFID, DIVE (Bohn et al., 2011) and DYNVEG provide us with one of the first key large-scale simplifications for dynamic vegetation; the sum of PFT/plant fractional grid-box area, $\sum \nu_i$, and the total unoccupied or bare space,

ν_{bare}, must be equal to one, the total grid box fractional area:

$$\nu_{\mathrm{bare}} + \sum \nu_i = 1. \tag{1.1}$$

Let us call this rule the "*hard exclusion approximation*". The key approximation, is that despite plants competing for many resources (light, water, and below ground nutrients, see Weiskittel et al. (2011)), space is one of the principle limiting resource, along with temperature and precipitation, that explains the vegetation distributions observed at large scales (Brovkin et al., 1997; Ramankutty and Foley, 1999). The "hard" element describes the absence of overlap between spaces occupied by PFTs, in reality there is a degree of tolerated overlaps between plants (Wang et al., 2008).

This method of area exclusion competition has a number of criticisms (McGill et al., 2006; Scheiter et al., 2013). Firstly, this might not realistically capture biome shifts or the ecological sorting one might expect from climate change (Pavlick et al., 2013). Secondly, the abstraction of competition means that such dynamic relationships are hard to relate with field measurements (Higgins et al., 2010).

Lotka approaches that use coverage and hard exclusion for competition have criticisms in terms of biodiversity (Scheiter et al., 2013). For instance, in the steady-state they cannot simulate the observed mixed communities of broadleaf or needleleaf trees seen in temperate latitudes (Arora and Boer, 2006; Liu et al., 2017). In a Lotka context, this is because having a competition coefficient equal to one can generate complete exclusion of sub-dominant PFTs. Having a competition coefficient less than one generates diversity, but this breaks the hard exclusion rule; the overall total vegetation area surpasses the grid-box area. The CTEM achieves diversity by allowing competition coefficients to be dependent on more complex competition-colonisation parametrisation based on inter-PFT invasion rates (Arora and Boer, 2006).

The hard exclusion approximation has been used to represent area-based disturbances from land use change to fire along with controlling the rate of subsequent regrowth (Shevliakova et al., 2009; Kato et al., 2013; Reick et al., 2013; Jain et al., 2013; Stocker et al., 2014; Bayer et al., 2017; Krause et al., 2018; Burton et al., 2019). Area based land-use change is perhaps easiest to simulate, not necessarily needing to represent plant demography. The implementation of land

use change in JULES-TRIFFID is to simply replace the natural PFTs with crop PFTs at an area dependent rate (Littleton et al., 2020). However, the representation of fire or drought disturbance through purely area, can overlook important dependencies with regards to plant size and age (Gora and Esquivel-Muelbert, 2021).

A second approach to area-averaged models is to build dynamics by primarily mechanistic means. The IBIS (Foley et al., 1996), SDGVM (Woodward et al., 1998; Woodward and Lomas, 2004), MC1 (Daly et al., 2000), LPJ (Sitch et al., 2003) and VEGAS (Zeng, 2003; Zeng et al., 2004) models simulate explicit light and/or water competition of mean PFT members within the ecosystems. This would be done by partitioning the population in between different "layers" representing either the canopy heights or root depths of vegetation. Additionally they may use an implementation of the self-thinning rule for competitive based mortality (see section 2.1.2 for an overview). There are benefits to this approach as, unlike the Lotka and area exclusion methods, there is less abstraction and a more direct link to physical processes, allowing for model validation through direct empirical measurements (Thonicke et al., 2001; Beer et al., 2007; Mao et al., 2007; Cunha et al., 2013). However, the cost is that increasing the number of processes, and thereby parameters, also increases issues relating to uncertainty at the regional scales (Zaehle et al., 2005; O'Hagan, 2012; Gustafson, 2013).

Like individual models, a stochastic trait based approach has been implemented in area-averaged models through the JeDi-DGVM (Pavlick et al., 2013). Lotka approaches are generally seen as not appropriate for trait-based stochasticity as the number of selected PFTs means that the competition coefficient matrix can quickly become computationally unwieldly; at rate of I^2, with I being the total PFT number. JeDI-DGVM can generate thousands of randomly sampled growth strategies on a global scale. For grid-box scaling the model uses the "biomass-ratio" hypothesis (Grime, 1998), simulated from the JeDI biogeographical equilibrium model (Kleidon and Mooney, 2000; Reu et al., 2011). The Biomass-ratio hypothesis is where the function (i.e. dominant, sub-dominant growth strategies) of the species is dictated from the relative contribution to the total community biomass. The JeDI-DGVM does not represent mechanistic competition for light or space. Similarly, the DIVE model has uses the original JeDI approach to preselect a distribution of PFT traits, however, DIVE then updates the PFTs area using the

hard-exclusion rule (Bohn et al., 2011). The PFTs in this latter model are prescribed using diversity outputs from the original JeDI trait model (Kleidon and Mooney, 2000; Reu et al., 2011).

1.2.3 Two Dimensional Cohort Models

In some ways, individual and area-averaged based DGVMs are similar. One relies on homogeneity of a 30mx30m plot at scale, the other relies on the homogeneity of the average individual. The landscape at grid-box scale is significantly more varied and beyond the theoretical or practical scope of both these approaches (Kane et al., 2011; Fisher et al., 2018; Shugart et al., 2020).

Recently, in a bid to overcome these shortcomings, development of global vegetation models have focused on producing cohort based models (Fisher et al., 2018). Cohort based models seek to partition plant populations according to demography. This is done by grouping into size – plant height, basal diameter, or mass – and age classes. These models occupy a middle ground in terms of complexity, and seek to capture the statistical distributions of plants and properties of the individual based models while eliminating the stochastic variability. The background theory derives from the application of partial differential equations (pdes) within ecology (Okubu et al., 1982).

The first cohort models focused on the community dynamics across size and age (henceforth: "*cohort 2D models*"). The ED model sought to replicate the statistics outputted by the earlier stochastic gap models (Moorcroft et al., 2001). ED successfully captures both vertical and horizontal heterogeneity of the community by partitioning populations into height and patch-age classes (Hurtt et al., 2004). Much like other vegetation models, mortality is driven by PFT type, self-thinning and resource availability. Light competition is simulated among "infinitely flat crown canopy layers" (Fisher et al., 2018). The patch-age structure is modelled by the equation:

$$\frac{\partial p}{\partial t} = \frac{\partial p}{\partial a} - \lambda p, \quad \int_0^\infty p \, da = 1, \tag{1.2}$$

where a is the age of the given patch, p is the probability distribution, and λ is the rate of patch disturbance or loss function. Equation (1.2) is an application of Von Foerster's cell-age kinetics (von Foerster, 1959; Trucco, 1965), applied to

represent the statical distribution of the patches explicitly represented by grids in the earlier gap models (Shugart and Smith, 1996). Modelling of patch age not only allows for the disturbance history of a region to be represented, but also allows for more realism in modelling of recruitment and disturbances via its dependency on "patch-interconnectedness", representing the effects of forest fragmentation (Fahrig, 2002; Neilson et al., 2005; Fisher et al., 2010).

Additionally in ED and other cohort models, the size-structure is updated through the Fokker-Planck or Kolmogorov forward equation, first formulated in the context of physiological age by Van Sickle (1977). The number density of plants, n, changes through plant size, z. The rate of change in the size dimension is described by the plant growth rate, g. The population is removed through a "sink", or mortality rate, γ:

$$\frac{\partial n}{\partial t} - \frac{\partial}{\partial z}\left[ng\right] = -\gamma n. \tag{1.3}$$

The variable z, could be any physical parameter related to the plant size such as the basal diameter or biomass, or height in the case of ED. Given information relating to how growth and mortality vary with this size variable, equation (1.2) and (1.3) will capture the statistical evolution of both the vertical and horizontal structure of a forest – without the need for individually representing every tree, overcoming one of the practical shortcomings of individual based models. ED and ED2 (Medvigy et al., 2009) have had success in modelling a variety ecosystems: arid (Dashti et al., 2021), boreal (Trugman et al., 2016), temperate (Antonarakis et al., 2014) and tropical vegetation (Zhang et al., 2015; Xu et al., 2016), demonstrating the validity of cohort based approaches down to plot level scales.

However, the modeling of both the size and age structure generates practical difficulties (Fisher et al., 2018). Firstly, by having an unfixed number of discrete patches, the potential number simulated is unbounded. Effectively, as time tends to infinity, $a \to \infty$ and the λ decay would mean that the number of patches, along with their corresponding size profiles, will tend to infinity (Figure 1.4). To get around this issue the ED series of models would arbitrarily merge patches of similar demographic properties (Fisher et al., 2010).

Another cohort 2D approach is to use Perfect Plasticity Approximation, (PPA), to describe light-crown competitive interactions, such as in the LM3-PPA model

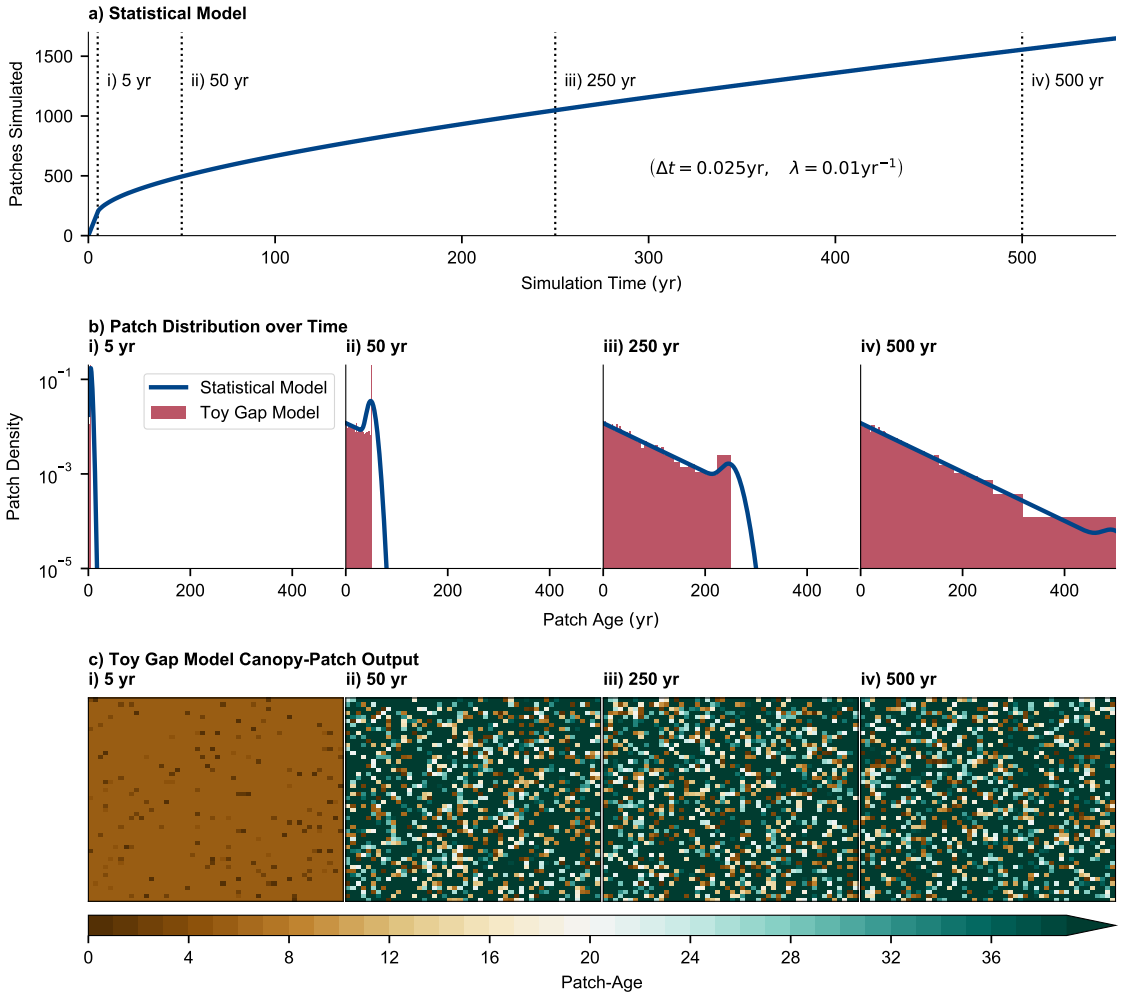

Figure 1.4: A rudimentary simulation of a forest from bare soil for 600 years, using the continuous patch equation (1.2), along with a toy gap model using a fixed 50x50 grid of patches on an arbitrary scale. The rate of disturbance with a fixed patch disturbance rate of $\lambda = 0.01\text{yr}^{-1}$. Panel (a) shows how without merging patches, the number of patches simulated can increase substantially, with a new patch added each time-step. Panel (b) shows how the age-distribution of patches changes through time for both the gap and statistical model. (c) shows the spatial age output from the fixed number of grids.

(Weng et al., 2015) or in the CLM(ED) model (Fisher et al., 2015). LM3-PPA simulates both size via basal diameter (dbh) and patch age cohorts, but also aggregates across PFTs into canopy layers for competition for light. PPA assumes that for each canopy layer, plant crowns will perfectly morph to fill out space. This is known as phototropism or plasticity (Purves et al., 2008; Strigul et al., 2008). PPA is in essence a more tractable, semi-analytical approximation to earlier individual approaches, such as the TASS model (Mitchell, 1975), to crown competition and morphology (Hallé et al., 2012). In each canopy layer of height z^*, the integrated product of number density and crown area, a, across the ordered height h, of the

plants must be less than or equal to the available fraction, F:

$$\int_{h>z^*}^{\infty} na\ dh \leq \mathrm{F}. \tag{1.4}$$

For the top layer, $\mathrm{F} = 1$. The available fraction may decreases through each layer (Weng et al., 2015). The fraction of photosynthetically active radiation attenuates through the canopy layer according to Beer's law. PPA can be viewed as at least partly related to the hard exclusion approximation. In essence both assumptions use either the plot/patch or grid-box area as a hard limit to the total vegetation area. In LM3-PPA, the mortality rate is the combination of size-independent mortality along with the additional height dependent mortality arising from being beneath the canopy layers. A later version LM3-PPA has also been successful in capturing the demographic distribution of both size and age within tropical forest using allometric power-law relationships for physical parameters (Martínez Cano et al., 2020).

Cohort 2D models have historically struggled with integration into ESMs or LSMs. The ED model was originally planned to be integrated into the JULES LSM in 2010 (Fisher et al., 2010), but this stalled partly because of the difficulties arising from coupling; the aforementioned unbounded age dimension and the fact that the dynamics were dependent on the physiology caused developmental issues (as highlighted in the talk Moore et al. (2013)). However, the recent GFDL-ESM4.1 does use the LM4.0-PPA dynamic vegetation model (Shevliakova et al., 2020) with results presented in the CMIP6 model ensemble (Arora et al., 2020).

1.2.4 One Dimensional Cohort Models

Recent developments have focused on taking a reductionist approach to two-dimensional cohort models by eliminating explicit representation of size or age classes. The benefit of this is easier integration into ESMs due to reducing the number of parameters and variables. For instance, the POP model (Haverd et al., 2014) eliminates size cohorts for an age based approach. POP performs processes at the grid-box scale, such as carbon assimilation, and then uses allometric relationships to infer the disaggregation into the age cohorts. Mortality arises from two components – stand crowding and resource limitation. This was included to reproduce the observation of self-thinning seen within forest com-

munities. POP has successfully been coupled into the CABLE ESMs (Haverd et al., 2018).

An additional approach is to simulate multiple types of PFT patches, such as in ORCHIDEE-MICT (Yue et al., 2018). The ORCHIDEE-MICT model partitions PFTs into age based sub-grid “Cohort Functional Types”. Plants move up into older classifications once the basal diameter surpasses a threshold. When this occurs patches are merged, with the new functional traits being the area weighted average. Another way to represent age is used in the JSBACH4 (Nabel et al., 2020) and LPJ-wsl2.0 models (Calle and Poulter, 2021), known as “vector tracking of fractional transitions”. In this approach, there is a fixed number of age classes containing several sub-divisions dependent on the timestep. The sum of fractions across all classes must equal one, to normalise with respect to patch population; equation (1.2). After a disturbance, such as deforestation or fire, the affected patch fraction is then substituted back into the lowest age class. The physiology or state variables within the age class is, again, the area weighted average. Much like cohort 2D models, the explicit representation of age requires a balance between realism and computational practicality.

An explicit size only approach is in the RED model (Argles et al., 2020), which is described in the later chapters of this thesis.

1.3 Discussion

The study of plant ecology and vegetation dynamics has progressed significantly since the early twentieth century. Early computational modelling included numerical evaluation of dynamical concepts such as the forest patch in competitive gap-succession models (Botkin et al., 1972b,a; Shugart and West, 1981). Forests play an important role in the climate system in general, such as the carbon and hydrological cycle. This has led to increased emphasis on understanding how forests change over large earth system scales (Peng, 2000). At the start of the twenty first century, climatologists and ecologists included vegetation dynamics into the climate models with the emergence of DGVMs (Cox et al., 2000; Cramer et al., 2001).

In an echo of earlier ecological debates, there were two principle modelling philosophies within the first applied DGVMs; individual and area-averaged;

complexity versus simplicity. There are simple top-down approaches that rely on reproducing the large scale, total area coverage or PFT spatial distributions, using the hard exclusion approximation (Brovkin et al., 1997; Cox, 2001; Arora and Boer, 2006). Other average area models attempted to simulate competition mechanistically through light and water (Foley et al., 1996; Woodward et al., 1998; Daly et al., 2000; Sitch et al., 2003; Woodward and Lomas, 2004). However, they only have a limited capacity to represent important sub-grid heterogeneity of forests; demography and diversity (Scheiter et al., 2013; Fisher et al., 2018). Demography is a significant factor in key processes of forested ecosystems that DGVMs strive to emulate; such as drought or fire and subsequent regrowth (Gora and Esquivel-Muelbert, 2021). Thus, area-averaged models may not be as accurate in the representation of ecosystem response to climate change.

In contrast, there are the bottom-up approaches of the gap-models. As expected, when it comes to capturing site-level dynamics, the scope and realism of gap models surpasses their simpler counterparts (Sato et al., 2010). Many of these site-level studies discuss the need to improve the representation of these processes in large scale climate and land-surface models (Kucharik et al., 2006; Sato, 2009). Yet in order to deal with computational cost, some of these models still make sacrifices in terms of large scale dynamical processes such as fire (Figures 1.2 & 1.3).

In recent years there has been an overall trend towards intermediate complexity DGVMs classed as cohort models (Figure 1.5). These attempt to address the major criticisms of both individual and area-averaged models by capturing the statistics and dynamics of forest populations using demography. The benefit of this is principally to overcome the stochastic variability and upscaling issues of individual based models. However, there are still some shortcomings with a significant proportion of these DGVMs in terms of tractability. Almost all cohort models seek to represent demographic patch age as a driving dimension. In a practical sense there are a few issues, firstly the arbitrariness of merging patches. Secondly, the difficulty of integration into ESMs. Finally, in a theoretical sense, large scale horizontal heterogeneity and patch-interconnectedness could potentially benefit from using a simpler approach. For instance, percolation theory can be used to infer the sub-grid spatial arrangement of forest fragments from total forest cover (Taubert et al. (2018); Saravia et al. (2018); and outlined in section

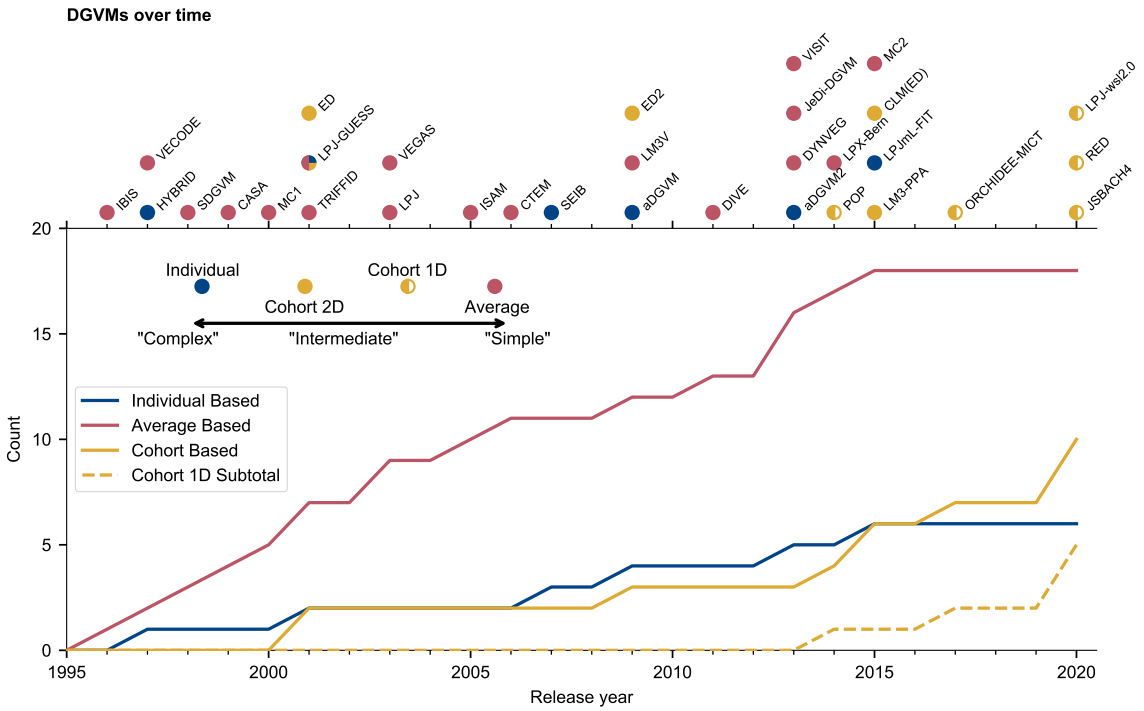

Figure 1.5: Broad modelling trends over time within the Dynamic Global Vegetation Model community (DGVM). Models are categorized into three types: Average, Intermediate, and Complex. (1) Simple - plant size or age demographics are not included beyond the "average" case. (2) Intermediate - models include the representation of size and/or age within cohorts. (3) Complex, demography is modelled in terms of explicit individuals.

2.1.1).

Within the latest CMIP6 model ensemble, that is currently being used to inform policy via the IPCC (International Panel on Climate Change), only a few ESMs (three out of eleven) have dynamic vegetation (Arora et al., 2020). Curiously more models have disturbances such as fire turned on, which neglects the role dynamic vegetation has on subsequent regrowth and ecosystem resilience. Out of the three that do, two models UKESM/JULES through TRIFFID, and MPI/JSBACH through DYNVEG, have simplistic average area approaches to modelling dynamics. The third, GFDL/LM4, is the latest iteration of the cohort approach from LM3-PPA. CMIP6 should be viewed as a transitional process with the steady implementation of more advanced and realistic models into the next generation of ESMs. There is a general acceptance for the need to include cohort models to "bridge" the divide (Figure 1.5) between the small scale and large scales.

The original and principle goal of DGVMs was to simulate dynamical processes of vegetation at the global level. For increasing realism to be success-

fully implemented, future models need to also weigh up tractability (Fisher et al., 2018). Let us set out some initial principles, (i) The long term geographic distribution of vegetation is ultimately governed by climatic and human factors (Clements, 1916). (ii) Large scale competition across space can represented by the hard exclusion approximation. From here let us, tentatively, expand the sphere of this understanding to encompass regional demography.

1.4 Objectives

The research aim of this PhD is to investigate and model the demographic dynamics of vegetation. To this end, we have set two primary objectives. Firstly, the thesis will examine a selection of statistical theories that describe the distribution of trees within forest. Additionally, we will investigate the implications arising from such theories in terms of carbon storage and ecosystem characteristics. Secondly, and most importantly, using such theories as a foundation we will further develop the Robust Ecosystem Demography (RED) Dynamic Global Vegetation Model for integration into Earth System Models. By including a tractable representation of tree demography through RED we will provide a more realistic framework for future modelling and research on key processes for ecosystem stability, such as drought or fire.

2 Demographic and Allometric Scaling in Forests

Rationale for Chapter

This chapter will review a variety of approaches to modelling horizontal and vertical (demographic) forest distributions. In particular we investigate a promising theory of demography that seems to explain large-scale demography of a variety of forests: Demographic Equilibrium Theory (DET). To expand on DET, we combine with allometric scaling relationships to produce relationships for forests quantities, such as carbon density or mean tree height. DET highlights how such quantities are unequally shared across a forest, holding true to the general rule that most of the forest biomass is within a few large individuals. From this chapter we start to answer our first thesis objective - a descriptions of forest demography and statistics and the implications for carbon storage and forest characteristics.

The main objective of cohort models (Figure 1.5) has been to reproduce the results of individual based models by understanding the statistical distributions of trees within forests. Growth and mortality can be highly variable at small scales and there could be many factors which influence these terms and resultant size and spatial profile of trees. It is widely understood that growth and mortality vary through competition, hydrology, elevation, nutrients, and many other factors (Baker et al., 2003). Despite this, forests and trees appear to exhibit shared, or "robust", statistical and physical characteristics (Niklas and Spatz, 2004; Moore et al., 2018, 2020; Mrad et al., 2020).

2.1 Overview of spatial and demographic dimensions

Cohort models try to reproduce horizontal (spatial) and vertical (e.g. height, size) distributions of forests. Until recently, our current understanding of forest statistics has been driven by a couple of concepts. Firstly, the use of patch-age to represent the distribution of horizontal heterogeneity (section 1.2.3). Secondly, the mechanistic implications of "self-thinning"; competition among trees causing increased mortality and limiting growth, resulting in the vertical/size distribution of forests being described via a power-law (Mrad et al., 2020). An alternative observation has been that a Weibull distribution describes the size-distribution of trees (Bailey and Dell, 1973). A physical derivation of the Weibull distribution has been offered by the recent concept of Demographic Equilibrium Theory (DET); that, rather than inter tree competition, it is the metabolic scaling of growth with size coupled with mortality that dictates the size-structure of forests (Kohyama et al., 2003; Moore et al., 2018, 2020).

2.1.1 Horizontal Heterogeneity

The spatial arrangement of forests plays an important role in ecosystem dynamics, such as species migration (Honnay et al., 2002) or disturbances such as severity of droughts and frequency of fire (Laurance and Williamson, 2001). The rate of gap formation (a gap being an opening within the canopy) and resultant fragmentation (how interconnected patches of trees are) can lead to consequences for biodiversity (Haddad et al., 2015), and general ecosystem resilience (Oliver et al., 2013). As previously outlined when discussing DGVMs (Figure 1.4), cohort models rely on Von Foerster statistics through patch-age to reproduce the statistical layout of the sub-grid distribution (Figure 2.1). Patch-age as a concept has been around long before the first numerical gap models (Watt, 1947; Bugmann, 2001), and is an important dimension within a number of DGVMs (Moorcroft et al., 2001; Smith, 2001; Medvigy et al., 2009). The concept of the patch is generally a level above an individual tree, such as a stand of trees. The age of the patch refers to time since the last disturbance, the rate of which demonstrates gap-formation. How gaps form is therefore a key process within

these models and essentially represents an additional area-based layer of mortality.

Clearing size distribution is indicative of the characteristics of disturbances and generally follows a power-law distribution. This has been validated in natural tropical (Nelson et al., 1994; Solé and Manrubia, 1995; Fisher et al., 2008; Asner et al., 2013; Lobo and Dalling, 2013), temperate (Nakashizuka et al., 1995; Gaudel et al., 2019), and boreal forests (Goodbody et al., 2020). Similarly, the distribution of patch size also follows a power law distribution and generally converges to similar distributions at regional scales, even in significantly different disturbance regimes (Taubert et al., 2018; Saravia et al., 2018). There are some similarities between patch disturbance rate and tree mortality. In tropical old-growth forests, there is a power-law relationship between the size and frequency of patch disturbance in relation to the number of trees killed in the disturbance (Chambers et al., 2013), with most mortality events happening at very small spatial scales. In terms of the regional carbon cycle, it has been estimated (using remotely sensed lidar and inventory data) that the vast majority ($\sim 98.6\%$) of above ground carbon losses of the Amazon occur at the sub $0.01\mathrm{ha}$ scale (Espírito-Santo et al., 2014).

It has been theorised that forest-fragmentation is a self-critical phenomena occupying a quasi equilibrium point determined by percolation theory (Shante and Kirkpatrick, 1971; Taubert et al., 2018; Saravia et al., 2018). Percolation theory predicts that for a randomly distributed grid of pixels that can exist in two or more states (such as forest patch versus clearing), and that there is a critical probability where the entropy is maximised. The number of interconnected patches is in a phase-transition between a few large patches, versus many disconnected patches.

To demonstrate percolation theory we investigate observations of forest cover. We use $30\mathrm{m} \times 30\mathrm{m}$ Global Forest Watch 2000 dataset (Hansen et al., 2013) for the Amazon: intact ($10°\mathrm{S}$ to $0°\mathrm{S}$ and $70°\mathrm{W}$ to $60°\mathrm{W}$) and fragmented rainforest ($20°\mathrm{S}$ to $10°\mathrm{S}$ and $60°\mathrm{W}$ to $50°\mathrm{W}$). To be more representative of the ESM land grid-box, these $10° \times 10°$ resolution datasets were further subdivided into a $1° \times 1°$ lattice (Figure 2.1.a). We define two possible states of forest cover on the $30\mathrm{m} \times 30\mathrm{m}$ resolution, firstly a patch being greater than 30% tree cover, otherwise the space is defined as clearing. For each $1° \times 1°$ grid-box we then aggregate the total fractional tree cover and compare with the mean fractional area and total number

of unique disconnected patches and clearings (Figure 2.1.b-c).

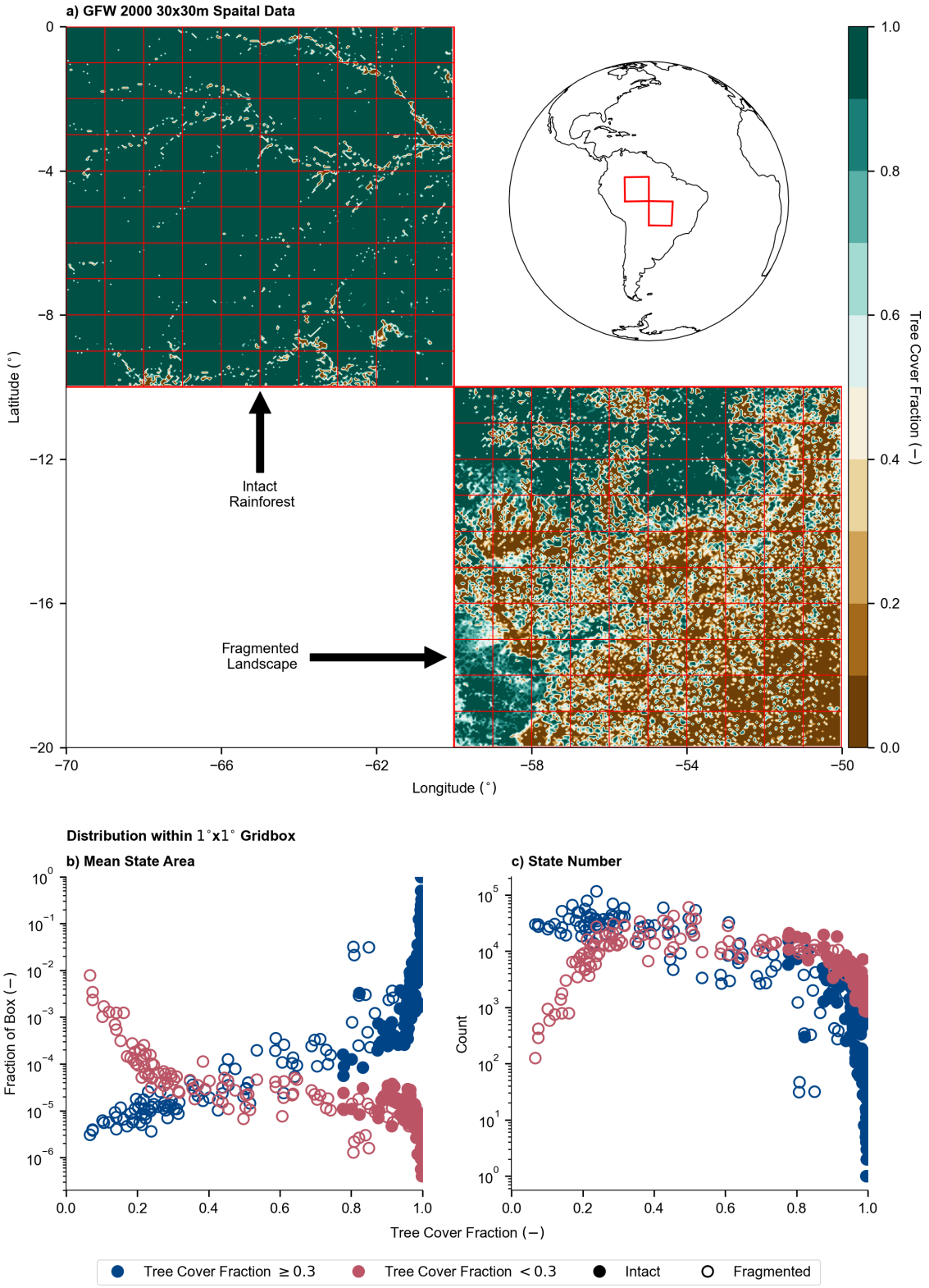

Figure 2.1: An analysis of $30\text{m} \times 30\text{m}$ spatial tree cover data at 2000 from the Global Forest Watch (GFW) (Hansen et al., 2013). (a) Picking two $10^\circ \times 10^\circ$ boxes from the large dataset representing both intact Amazonian rainforest and neighbouring fragmented landscape. We subdivide into finer $1^\circ \times 1^\circ$ resolution to investigate how the mean patch (tree cover fraction ≥ 0.3) or clearing (tree cover fraction < 0.3) area (b), and how the number of patches and clearings (c) varies with overall gird-box forest cover.

From figure 2.1 we see that there is a clear relationship and constraint between the total fractional tree cover and sub-grid spatial distribution of the landscape. When the $1^\circ \times 1^\circ$ grid-box tree cover fraction approaches 1, the number and mean fraction size of patches tends to 1, while the number and mean fraction area of clearings approaches 0. While the opposite is true when total tree cover approaches 0.

While percolation theory appears to show a relationship between forest cover and the fragmentation of a landscape, it has not been implemented within a dynamical vegetation model. Parametrisation of the forest-cover fragmentation relationship could potentially bypass the need to represent age since last disturbance as a demographic dimension. However, this concept could be difficult to implement due to non-linearity in the dynamics (Da Silveira Lobo Sternberg, 2001; Kinzig et al., 2006; Staal et al., 2020).

2.1.2 Self-Thinning

Alongside the early debate about successional dynamics, the concept of self-thinning was established to describe the distribution of the forest size-structure. In 1933, L.H. Reineke, showed that undisturbed, even-aged forests would exhibit a power-law relationship (with exponent $-\phi$) between number density, n, and the diameter of the tree, d (Reineke, 1933):

$$n \propto d^{-\phi} \tag{2.1}$$

Self-thinning is usually assumed to describe how individual trees may shade each other, restricting their growth and resulting in an increases in mortality (Perry, 1984; Westoby, 1984; Dewar, 1993). One common mechanistic explanation is that decreases in photosynthesis caused by crown competition is not compensated by respiration resulting in carbon starvation of individuals (Mrad et al., 2020). In 1963, K. Yoda conducted an analysis by looking at how the number density varied with respect to Above Ground Biomass (AGB) (Yoda, 1963). Yoda (1963) found a power-law relationship of 2/3 (usually represented in terms of 3/2 number density to biomass “Yoda’s 3/2 rule”):

$$n \propto \mathrm{AGB}^{-2/3}. \tag{2.2}$$

Equation (2.2) can be derived from allometric, metabolic, and dynamical relationships, and in many cases without reference to competition for space (Reynolds and Ford, 2005; Mrad et al., 2020). These derivations provide a wide range for the number density-biomass exponent; between 0.67 and 1.8 for biomass (Mrad et al., 2020).

Self-thinning has mainly been perceived as a consequence of resource limitation within a patch (Zhang et al., 2011). Growth or resource use efficiency has been used as a mechanism to link additional mortality in dynamic models (Daly et al., 2000; Moorcroft et al., 2001; Sitch et al., 2003; Haverd et al., 2014). The power law relationship has been derived via Metabolic Scaling Theory (MST). First introduced by G.West, B.J. Brown and E. Enquist (West et al., 1997), MST assumes growth, g, scales with mass, m, to the power of $3/4$:

$$g = g_0 \left(\frac{m}{m_0}\right)^{\phi_g}, \quad \phi_g = \frac{3}{4}. \tag{2.3}$$

g_0 is the growth rate at lowest mass m_0. MST has been used to derive tree density assumed under dynamic equilibrium (Enquist et al., 1998, 2009):

$$n \propto m^{-\frac{3}{4}} \tag{2.4}$$

We know how the forest size-structure is dependent on both the mortality and growth through the Fokker-Planck equation (1.3). Yet an oversight of self-thinning is the lack of dependence of number density on mortality. We can show this by substituting the MST growth relationship into the Fokker-Planck equation and setting the mortality, γ and $\partial n/\partial t$ to zero:

$$\frac{\partial n}{\partial t} - \frac{\partial}{\partial z}\left[ng\right] = -\gamma n \rightarrow \frac{d}{dz}\left[ng\right] = g\frac{dn}{dz} + n\frac{dg}{dz}, \tag{2.5}$$

$$\frac{1}{n}\frac{dn}{dz} = \frac{1}{g}\frac{dg}{dz}. \tag{2.6}$$

Integrating equation 2.6 gives us a number density dependence on only the metabolic scaling of growth, $g \propto z^{\phi_z}$, which when integrated gives us our self-thinning number density relationship:

$$n = n_0 \left(\frac{z}{z_0}\right)^{-\phi_z}, \quad n = n_0 \left(\frac{m}{m_0}\right)^{-\frac{3}{4}}. \tag{2.7}$$

In a sense self-thinning gives us a theoretical maximum number density for forests stands. This has been one of self-thinnings practical uses in planning even-age plantations (Drew and Flewelling, 1977; Monserud et al., 2004).

2.1.3 Demographic Equilibrium Theory

Self-thinning does not adequately explain parts of the forest size-structure. The theory does not account for the increased rate of decline in the number density for larger sized trees. There have been multiple studies which have shown this inadequacy; in pan-tropical forests (Kohyama et al., 2003; Muller-Landau et al., 2006; Moore et al., 2020), temperate forests (Coomes et al., 2003; Moore et al., 2018; Zhou and Lin, 2018) and in forest plantations (Monserud et al., 2004). The shape of forest-size profiles have been shown to be driven by both mortality and growth.

Demographic Equilibrium Theory (DET) is comparably a recent concept. DET explores the steady state size-structure from the Fokker-Plank equation (1.3). The steady state (equilibrium) size-structure number density is where the number of individuals growing into a size is balanced by the number dying and growing past said size, this happens across all sizes. In the simplest form of DET there are two key assumptions: that growth follows metabolic scaling theory and that the mortality is size invariant. Therefore, we integrate a modified equation (2.5) for the number density across size:

$$\frac{1}{n}\frac{dn}{dz} = \frac{\gamma}{g} + \frac{1}{g}\frac{dg}{dz}, \tag{2.8}$$

which integrates into a Left Truncated Weibull Distribution (LTWD):

$$n = n_0 \left(\frac{z}{z_0}\right)^{-\phi_z} \exp\left\{\frac{\gamma z_0}{g_0\left(1-\phi_z\right)}\left[1-\left(\frac{z}{z_0}\right)^{1-\phi_z}\right]\right\}. \tag{2.9}$$

The resulting Weibull distribution has been validated in tropical and temperate forests (Coomes et al., 2003; Kohyama et al., 2003; Muller-Landau et al., 2006; Moore et al., 2018, 2020). Even before the dynamic derivation of DET was established, foresters have been using the Weibull equation to predict stand density (Bailey and Dell, 1973). On average, at large scale and across a variety of types, forests conform to the emergent Weibull distribution of DET (Figures 2.2 & 2.3).

Given the validation of DET to demographic data, the theory offers both a simple theoretical foundation of demography, that is improved over the power-law offered by self-thinning, along with a low number of parameters that can be easily calibrated for dynamic models (see chapters 5 & 3)).

The result that forest size-structure follows a Weibull distribution does not apply in certain instances. For example, distributions of forest size-structure can be multi-modal (Zhang and Liu, 2006). We see divergence in particular categories of forests in North America (Figure 2.2.a-c), which could be a result of historically disturbed forests; there is a local maximum of number density occurring roughly at $60\mathrm{cm}$ diameter for Broadleaf Evergreen Species and Needleleaf Deciduous Species (Moore et al., 2018). This divergence from DET could be indicative of a forest out of equilibrium. Disequilibrium is generally seen as a result of succession, competition and disturbances (Maltamo et al., 2000; Coomes and Allen, 2007).

Size-invariant mortality is not necessarily seen in observations. The functional form of mortality across size can vary depending on abiotic and biotic processes (Lu et al., 2021). Mortality across size has been shown to follow a parabolic "u" shape at a community level, such that small and large trees experience additional mortality with a minimum rate for medium sized trees (Coomes and Allen, 2007; Lines et al., 2010; Lu et al., 2021). The smaller tree increase in mortality has been attributed to competition and pests (Iida et al., 2014). While the additional larger tree mortality has been attributable to increased susceptibility from disturbances such as drought or wind-throw (Coomes et al., 2003; Rowland et al., 2015).

The assumption of metabolic scaling of growth implies independence of growth from the demographic effects of light competition. Forests can have distinct "canopy layers". Ecologists have generally described this arising from "canopy closure" (Jennings et al., 1999) and it can generate a bimodal height distribution (Harding et al., 2001). Trees in the lower canopy have a lower growth rate (Stark et al., 2015). The diameter-growth exponent can vary significantly from that predicted by MST at the species level (Reich et al., 2006; Coomes et al., 2011; Rüger and Condit, 2012). However, at the community average there is convergence to MST exponents (Rüger and Condit, 2012), which suggests at the PFT and regional scale, MST is a valid assumption.

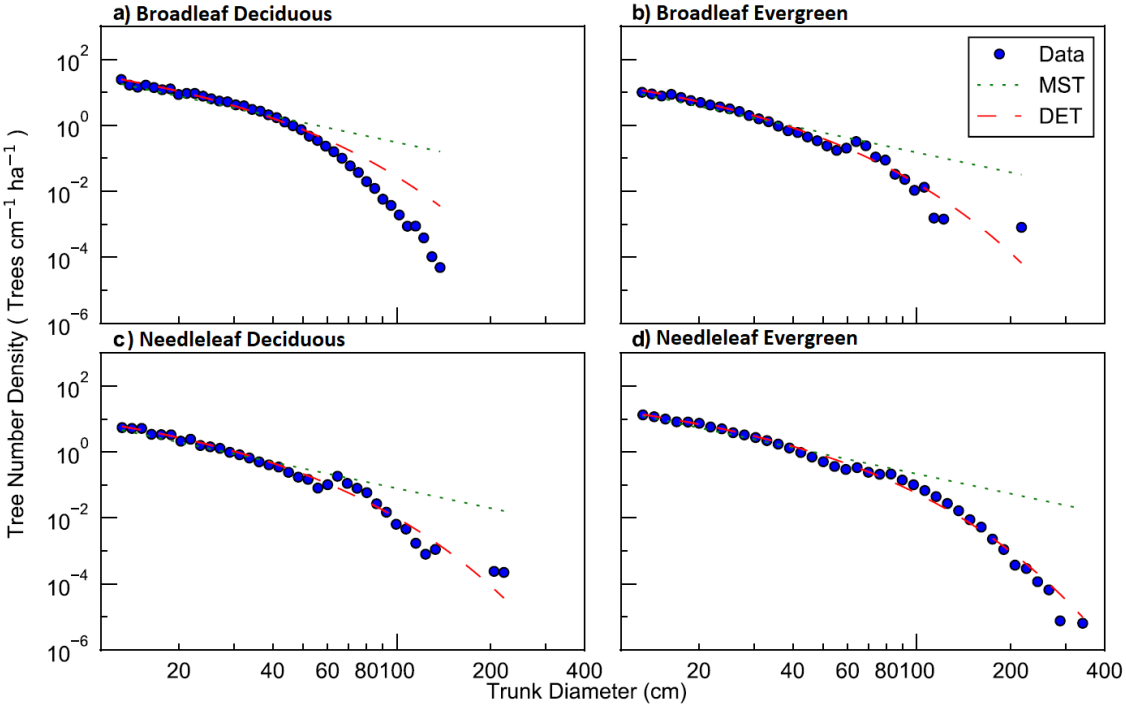

Figure 2.2: From Moore et al. (2018), showing the predictions of DET (Demographic Equilibrium Theory, equation (2.9)) against that of MST (Metabolic Scaling Theory or Self-Thinning via equation (2.4)) for trunk diameters in North America. The dataset is from the USDA Forest Service FIA program (Oswalt et al., 2014). Panels show (a) Broadleaf Deciduous Species, (b) Broadleaf Evergreen Species, (c) Needleleaf Deciduous Species, and (d) Needleleaf Evergreen Species.

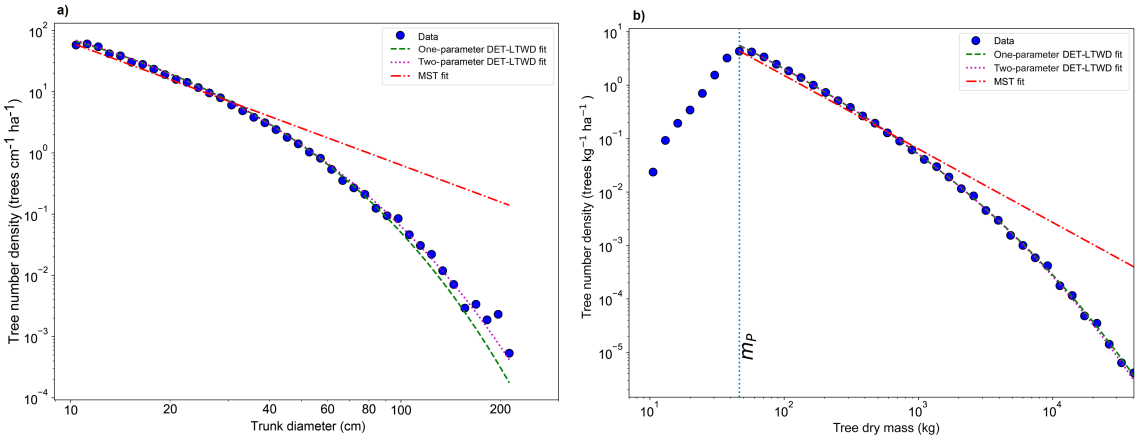

Figure 2.3: From Moore et al. (2020), predictions for South America of MST (Metabolic Scaling Theory or Self-Thinning via equation (2.4)) and DET from the RAINFOR dataset (Peacock et al., 2007). Panels (a) plots number density against empirical measurements of basal diameter. Panel (b) plots number density against inferred tree dry mass using allometric formula (Feldpausch et al., 2012). Data to the left of m_p is affected by an artefact from the conversion from basal diameter to mass; measurements from RAINFOR do not go bellow 10cm dbh and thus "miss" the complete range of valid masses. LTWD is the Distribution derived Left Truncated Weibull Distribution through equation (2.9). Fits are maximum likelihoods estimations for single parameter - μ_0, and two parameter - μ_0 and ϕ, from equation (2.9).

2.2 Some Implications of DET

Some DGVMs assume a relationship between crowding and mortality, principally to replicate the size-structure implied by self thinning, but when compared to large-scale data there is clear divergence away from the self-thinning power-law (Figures 2.2 & 2.3). DET has been shown to diverge from site-level observations in terms of both growth and mortality (Maltamo et al., 2000; Coomes and Allen, 2007). DET provides an opportunity to move past simpler area-averaged models and include a parameter-sparse framework for realistic large-scale demography models in the next generation of DGVMs, all without the complexity of two-dimensional cohort approach, such as ED (Moorcroft et al., 2001). Indeed, studying the situations where the demography diverges from DET can potentially inform how processes, such as competition and diversity, scale with model resolution. In this section, we outline some of the implications of coupling DET to allometric power-laws. This approach has been used to estimate regional biomass densities in the Amazon (Moore et al., 2020), and has been used to investigate the coupling of the self-thinning number density to allometric relationships (Pretzsch, 2006).

2.2.1 Allometric Relationships

We can use some allometric power laws to describe how the mean physical characteristics of a stand depend on size. Initially, allometry relationships were derived by investigating the structural limits of trees. The basal diameter, height, wood density and gravity dictate tree morphology in relation to other dimensions, these consist of non-linear power-law relationships of varying complexity (Chave et al., 2005) and have been used in a variety of dynamic models. These relationships, in their simplest forms, follow a isometric power-law; trees (much like other organisms) are in general self-similar versions of their younger selves (McMahon, 1973; McMahon and Kronauer, 1976). McMahon and Kronauer (1976) first used the Euler-Greenhill formula to predict how the height of a tree, h, would vary with basal diameter, d:

$$h = h_0 \left(\frac{d}{d_0} \right)^{\frac{2}{3}}. \tag{2.10}$$

Equation (2.10) was formulated from structural considerations. Organisms are limited to a maximum height due to compressive stress under gravity, beyond which they would buckle. Trunk tapering is also be an important consideration, and would feature as an additional parameter. This implies that the height would always operate close to this gravitational limit until the trunk grew to sufficient diameter to support extra height. McMahon and Kronauer (1976) also found that, in general the diameter varied with mass by the power of $3/8$:

$$d = d_0 \left(\frac{m}{m_0} \right)^{\frac{3}{8}}. \tag{2.11}$$

The $d \propto m^{\frac{3}{8}}$ relationship has been evaluated by numerous authors (Chave et al., 2005). Substituting equations (2.10) and (2.11) for the relationship between mass and height gives us:

$$h = h_0 \left(\frac{m}{m_0} \right)^{\frac{1}{4}}, \tag{2.12}$$

the power of which has been independently derived and validated (Niklas and Enquist, 2001). Although the power can vary significantly dependent on geographic region (Feldpausch et al., 2011).

There are alternative derivations of tree allometry through growth and hydrological constraints (Niklas and Spatz, 2004). In the Niklas and Spatz (2004) method, they use two observations relating to the growth rate of a plant; isometric/linear scaling with the plant's total leaf mass, m_l, (Bond-Lamberty et al., 2002) and MST assumptions of growth:

$$g = g_0 \left(\frac{m_l}{m_{l,0}} \right) = g_0 \left(\frac{m}{m_0} \right)^{\frac{3}{4}}. \tag{2.13}$$

The next step relates to how vascular plants partition biomass between their pools (steam - m_s, leaf and roots - m_r), the sum of which is equal to m:

$$m = m_l + m_s + m_r. \tag{2.14}$$

By assuming proportionality between leaf area with the xylem cross sectional

area, which in turn is proportional to the square of the stem diameter:

$$m_l = m_{l,0} \left(\frac{d}{d_0} \right)^2, \tag{2.15}$$

along with the assumption that the root mass is proportional to the stem mass:

$$m_r = m_{r,0} \left(\frac{m_s}{m_{s,0}} \right), \tag{2.16}$$

Niklas and Spatz (2004) showed that the stem mass is proportional to:

$$m_s = \left(\frac{1}{1 + \frac{m_{r,0}}{m_{s,0}}} \right) \left(m_0 \left(\frac{d}{d_0} \right)^{\frac{8}{3}} - m_{l,0} \left(\frac{d}{d_0} \right)^2 \right). \tag{2.17}$$

Equation (2.17) illustrates that for $m_0 >> m_{l,0}$ and $d >> d_0$, we have approximatley the same relationship for stem mass derived from gravitational constraints; equation (2.11)). Niklas and Spatz (2004) also modelled how the height would vary in relation to the basal diameter by taking that the stem mass is proportional to the cross-sectional area multiplied by the height:

$$m_s = m_{s,0} \left(\frac{d}{d_0} \right)^2 \left(\frac{h}{h_0} \right). \tag{2.18}$$

Putting equation (2.17) with equation (2.18) gives us a new allometric height relationship:

$$h = \frac{h_0}{m_0 - m_{l,0}} \left(m_0 \left(\frac{d}{d_0} \right)^{\frac{2}{3}} - m_{l,0} \right). \tag{2.19}$$

A final Niklas and Spatz (2004) model result is that substituting equation (2.13) into equation (2.15) we find the same mass-height relationship that McMahon (1973) found in equation (2.11). Niklas and Spatz generally found better agreement with stem mass and height data than the classical Euler-Greenhill formula for smaller trees, although their allometric relationships are remarkably similar for large trees. Niklas and Spatz (2004) concluded that growth and hydraulic assumptions seem to explain size-allometry in trees. However, some of the assumptions, such as equation (2.15), do not necessarily explain certain allometric behaviour for small and large trees (Chave et al., 2014).

In general and for the sake of simplicity, let us assume some power-law relationship relating plant mass to basal diameter, crown area, a (Alves and Santos,

2002), and height, in addition to MST; equation (2.3). Respectively:

$$d = d_0 \left(\frac{m}{m_0}\right)^{\phi_d}, \tag{2.20}$$

$$a = a_0 \left(\frac{m}{m_0}\right)^{\phi_a}, \tag{2.21}$$

$$h = h_0 \left(\frac{m}{m_0}\right)^{\phi_h}. \tag{2.22}$$

Where ϕ is the rate of scaling of the given variable. d_0, a_0, h_0 are boundary values of physical properties at mass m_0.

2.2.2 Integrating the Weibull Distribution

If we combine the allometric relationships with the DET Weibull distribution from equation (2.9), we are able to get the average or total density properties of an ecosystem, such as the mean height or total biomass per unit area. Let us start by using mass as our size dimension, $z \to m$:

$$n = n_0 \left(\frac{m}{m_0}\right)^{-\phi_g} \exp\left\{\frac{\mu_0}{1-\phi_g}\left[1 - \left(\frac{m}{m_0}\right)^{1-\phi_g}\right]\right\}. \tag{2.23}$$

μ_0 is a key parameter which describes the shape of the curve. μ_0 is a metric of turnover describing the ratio of mortality to the growth:

$$\mu_0 = \frac{\gamma m_0}{g_0}. \tag{2.24}$$

The higher the value of μ_0, i.e. through increased mortality, the quicker the drop-off in the Weibull shape - we would see fewer big trees (Figure 2.4). Due to the assumptions of MST, there is a relationship between μ_0 and the boundary mass. Therefore, to remove this dependence, we refer to μ_0 at a specific mass, μ_{ref}, such that:

$$\mu_0 = \mu_{\mathrm{ref}} m_0^{1-\phi_g}. \tag{2.25}$$

The typical reference mass we assume for μ_{ref} is $1\mathrm{kgC}$ (Argles et al., 2020). When fitting of the RAINFOR South American dataset (Figure 2.3.b), this was found to be $\mu_{1\mathrm{kgC}} \approx 0.235$, after converting from total biomass into carbon mass, which scales by a factor of two (Moore et al., 2020).

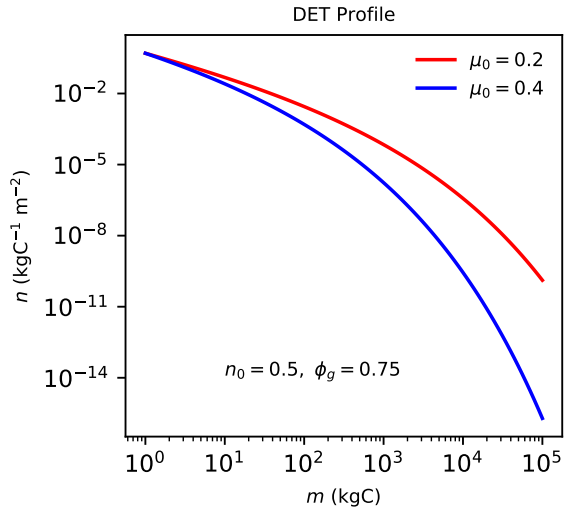

Figure 2.4: The size profile for different values of demographic turnover, μ_0 - assuming fixed n_0 and ϕ_g.

Number Density

We can estimate the binned number density between two masses if we integrate across mass using equation (2.23) between m_a to m_b:

$$N = n_0 \exp\left\{\frac{\mu_0}{1-\phi_g}\right\} \int_{m_a}^{m_b} \left(\frac{m}{m_0}\right)^{-\phi_g} \exp\left\{-\left(\frac{\mu_0}{1-\phi_g}\right)\left(\frac{m}{m_0}\right)^{1-\phi_g}\right\} dm, \quad (2.26)$$

using the substitution:

$$\begin{aligned} u &= \left(\frac{\mu_0}{1-\phi_g}\right)\left(\frac{m}{m_0}\right)^{1-\phi_g}, \quad m = m_0 \left(\frac{1-\phi_g}{\mu_0}\right)^{\frac{1}{1-\phi_g}} u^{\frac{1}{1-\phi_g}}, \\ dm &= m_0 \mu_0^{-\frac{1}{1-\phi_g}} (1-\phi_g)^{\frac{\phi_g}{1-\phi_g}} u^{\frac{\phi_g}{1-\phi_g}} du, \quad u_0 = \frac{\mu_0}{1-\phi_g}, \end{aligned} \quad (2.27)$$

$$N = \left(\frac{n_0 m_0}{\mu_0}\right) \exp\{u_0\} \int_{u_a}^{u_b} \exp\{-u\} du, \quad (2.28)$$

$$N = \left(\frac{n_0 m_0}{\mu_0}\right) \exp\{u_0\} [\exp\{-u_a\} - \exp\{-u_b\}]. \quad (2.29)$$

In the limit of $m_a \to m_0$ and $m_b \to \infty$ the total stand density becomes:

$$N = \frac{n_0 m_0}{\mu_0} = \frac{n_0 g_0}{\gamma}. \quad (2.30)$$

Equation (2.30) makes intuitive sense as the total number of deaths, γN, is equal to the recruited (boundary) flux, $n_0 g_0$, which should be the case at demographic equilibrium. If we divide the original Weibull distribution, equation (2.23), by the

total number density we find the Probability Density Function (PDF), f_n:

$$f_n = \left(\frac{\mu_0}{m_0}\right)\left(\frac{m}{m_0}\right)^{-\phi_g} \exp\left\{\frac{\mu_0}{1-\phi_g}\left[1-\left(\frac{m}{m_0}\right)^{1-\phi_g}\right]\right\}. \tag{2.31}$$

By dividing equation (2.29), with $u_a \to u_0$, and the total number density, we also find the Cumulative Density Function (CDF), F_n:

$$F_n = 1 - \exp\left\{\frac{\mu_0}{1-\phi_g}\left[1-\left(\frac{m}{m_0}\right)^{1-\phi_g}\right]\right\}. \tag{2.32}$$

General Scaling Total, Mean, PDF, CDF

Given the consistency of the power-law functional form for growth, equation (2.3)), and the allometry, equations (2.20-2.22)) , we assume the substitute power law:

$$z = z_0\left(\frac{m}{m_0}\right)^{\phi_z}, \tag{2.33}$$

where z is a dummy variable. Integrating the product of $\int nz\, dm$, the total quantity Z between m_a and m_b:

$$Z = z_0 n_0 \exp\left\{\frac{\mu_0}{1-\phi_g}\right\}\int_{m_a}^{m_b}\left(\frac{m}{m_0}\right)^{\phi_z-\phi_g}\exp\left\{-\left(\frac{\mu_0}{1-\phi_g}\right)\left(\frac{m}{m_0}\right)^{1-\phi_g}\right\}dm. \tag{2.34}$$

Using the substitutions of equation (2.27), along with the total number density, $n_0 m_0/\mu_0$, we get:

$$Z = z_0 N\left(\frac{1-\phi_g}{\mu_0}\right)^{\frac{\phi_z}{1-\phi_g}}\exp\{u_0\}\int_{u_a}^{u_b} u^{\frac{\phi_z}{1-\phi_g}}\exp\{-u\}du. \tag{2.35}$$

The integral of equation (2.35) can be solved using the definition of the upper incomplete gamma function:

$$\Gamma(c,x) = \int_x^\infty t^{c-1}\exp\{-t\}dt, \tag{2.36}$$

or in the case of integrating between x_a and x_b:

$$\Gamma(c,x_a) - \Gamma(c,x_b) = \int_{x_a}^{x_b} t^{c-1}\exp\{-t\}dt, \tag{2.37}$$

which gives us:

$$Z = z_0 N \left(\frac{1-\phi_g}{\mu_0}\right)^{\frac{\phi_z}{1-\phi_g}} \exp\{u_0\} \left[\Gamma\left(\frac{\phi_z}{1-\phi_g}+1, u_a\right) - \Gamma\left(\frac{\phi_z}{1-\phi_g}+1, u_b\right)\right]. \tag{2.38}$$

For across the entire size-structure, $m_a \to m_0$ and $m_b \to \infty$:

$$Z = z_0 N \left(\frac{1-\phi_g}{\mu_0}\right)^{\frac{\phi_z}{1-\phi_g}} \exp\left\{\frac{\mu_0}{1-\phi_g}\right\} \Gamma\left(\frac{\phi_z}{1-\phi_g}+1, \frac{\mu_0}{1-\phi_g}\right). \tag{2.39}$$

We define the function $\mathcal{F}_z$ as:

$$\mathcal{F}_z = \left(\frac{1-\phi_g}{\mu_0}\right)^{\frac{\phi_z}{1-\phi_g}} \exp\left\{\frac{\mu_0}{1-\phi_g}\right\} \Gamma\left(\frac{\phi_z}{1-\phi_g}+1, \frac{\mu_0}{1-\phi_g}\right) \tag{2.40}$$

$\mathcal{F}_z$ is a factor which describes how the total quantity Z, scales in relation to total number density. The expected value of z per plant, $\langle z \rangle_N$, is given by dividing equation (2.39) by N, which is just:

$$\langle z \rangle_N = z_0 \mathcal{F}_z. \tag{2.41}$$

For the PDF of variable z, f_z, we divide nz by the total, equation (2.39):

$$f_z = \frac{\left(\frac{\mu_0}{m_0}\right)\left(\frac{m}{m_0}\right)^{\phi_z-\phi_g} \exp\left\{-\left(\frac{\mu_0}{1-\phi_g}\right)\left(\frac{m}{m_0}\right)^{1-\phi_g}\right\}}{\left(\frac{1-\phi_g}{\mu_0}\right)^{\frac{\phi_z}{1-\phi_g}} \Gamma\left(\frac{\phi_z}{1-\phi_g}+1, \frac{\mu_0}{1-\phi_g}\right)}. \tag{2.42}$$

The corresponding CDF, $u_a \to u_0$, is given by:

$$F_z = 1 - \frac{\Gamma\left(\frac{\phi_z}{1-\phi_g}+1, \frac{\mu_0}{1-\phi_g}\left(\frac{m}{m_0}\right)^{1-\phi_g}\right)}{\Gamma\left(\frac{\phi_z}{1-\phi_g}+1, \frac{\mu_0}{1-\phi_g}\right)} \tag{2.43}$$

Total Growth

The community growth, G, is given by substituting in the MST relationship, equation (2.3), $z \to g$, $\phi_z \to \phi_g$:

$$G = g_0 N \mathcal{F}_g = g_0 N \left(\frac{1-\phi_g}{\mu_0}\right)^{\frac{\phi_g}{1-\phi_g}} \exp\left\{\frac{\mu_0}{1-\phi_g}\right\} \Gamma\left(\frac{1}{1-\phi_g}, \frac{\mu_0}{1-\phi_g}\right). \tag{2.44}$$

By assuming that $\phi_g = 3/4$ and using the series definition of the incomplete gamma function:

$$\Gamma(c, x) = (c-1)! \exp\{-x\} \sum_{k=0}^{c-1} \frac{x^k}{k!}, \tag{2.45}$$

the gamma function expands out to:

$$\Gamma(4, 4\mu_0) = 6 \exp\{-4\mu_0\} \left(1 + 4\mu_0 + 8\mu_0^2 + \frac{32\mu_0^3}{3}\right), \tag{2.46}$$

which gives us the polynomial equation:

$$G = g_0 N \left(1 + \frac{3}{4\mu_0} + \frac{3}{8\mu_0^2} + \frac{3}{32\mu_0^3}\right). \tag{2.47}$$

Total Carbon Density

For the total carbon density, M, $z \to m$ and $\phi_z \to 1$, therefore:

$$M = m_0 N \mathcal{F}_m, \tag{2.48}$$

or in terms of $\phi_g = 3/4$:

$$M = m_0 N \left(1 + \frac{1}{\mu_0} + \frac{3}{4\mu_0^2} + \frac{3}{8\mu_0^3} + \frac{3}{32\mu_0^4}\right). \tag{2.49}$$

Total Coverage (Canopy Area) and Mean per Coverage

Assuming total coverage is consistent with the total canopy area, the total coverage, ν, with $z \to a$ and $\phi_z \to \phi_a$ is given as:

$$\nu = a_0 N \mathcal{F}_a. \tag{2.50}$$

or when $\phi_a = 1/2$ (West et al., 2009) and $\phi_g = 3/4$:

$$\nu = a_0 N \left(1 + \frac{1}{2\mu_0} + \frac{1}{8\mu_0^2}\right). \tag{2.51}$$

For the mean of a scaling quantity per unit vegetation area, $\langle z \rangle_\nu$, we must first integrate the equation (2.34):

$$z_0 a_0 n_0 \exp\left\{\frac{\mu_0}{1-\phi_g}\right\} \int_{m_0}^{\infty} \left(\frac{m}{m_0}\right)^{\phi_z+\phi_a-\phi_g} \exp\left\{-\left(\frac{\mu_0}{1-\phi_g}\right)\left(\frac{m}{m_0}\right)^{1-\phi_g}\right\} dm, \tag{2.52}$$

as the coverage over mass is given by the product; na. By using the subsitution into equation (2.39) we get:

$$Z = z_0 a_0 N \left(\frac{1-\phi_g}{\mu_0}\right)^{\frac{\phi_z+\phi_a}{1-\phi_g}} \exp\left\{\frac{\mu_0}{1-\phi_g}\right\} \Gamma\left(\frac{\phi_z+\phi_a}{1-\phi_g}+1, \frac{\mu_0}{1-\phi_g}\right). \tag{2.53}$$

Finally, dividing by the total coverage, equation (2.50) we get a relationship for the coverage weighted mean, $\langle z \rangle_\nu$:

$$\langle z \rangle_\nu = z_0 \left(\frac{1-\phi_g}{\mu_0}\right)^{\frac{\phi_z}{1-\phi_g}} \left(\frac{\Gamma\left(\frac{\phi_z+\phi_a}{1-\phi_g}+1, \frac{\mu_0}{1-\phi_g}\right)}{\Gamma\left(\frac{\phi_a}{1-\phi_g}+1, \frac{\mu_0}{1-\phi_g}\right)}\right). \tag{2.54}$$

Mean Basal Diameter

The total basal diameter density or total height density for an ecosystem is not an important measurement. The mean basal diameter per plant could be useful for model validation. For now, let us assume that $z \to d$, and $\phi_z \to \phi_d$, applying the mean dbh per plant: (2.41) gives us:

$$\langle d \rangle_N = d_0 \mathcal{F}_d. \tag{2.55}$$

For the power of $\phi_d = 3/8$ and $\phi_g = 3/4$, equation (2.55) gives a infinite series of polynomials as $\Gamma(5/2, 4\mu_0)$.

Mean Height

For estimating the mean height we could use both the mean plant, equation (2.41), or mean canopy height, equation (2.54). So for the mean plant height, with $z \to h$ and $\phi_z \to \phi_h$, we get:

$$\langle h \rangle_N = h_0 \mathcal{F}_h. \tag{2.56}$$

Which for $\phi_h = 1/4$ and $\phi_g = 3/4$ we end up with:

$$\langle h \rangle_N = h_0 \left(1 + \frac{1}{4\mu_0}\right). \tag{2.57}$$

Or in terms of mean coverage area - which is useful for estimating the surface roughness of a forest (Nakai et al., 2008):

$$\langle h \rangle_\nu = h_0 \left(\frac{1-\phi_g}{\mu_0}\right)^{\frac{\phi_h}{1-\phi_g}} \left(\frac{\Gamma\left(\frac{\phi_h+\phi_a}{1-\phi_g}+1, \frac{\mu_0}{1-\phi_g}\right)}{\Gamma\left(\frac{\phi_a}{1-\phi_g}+1, \frac{\mu_0}{1-\phi_g}\right)}\right). \tag{2.58}$$

With $\phi_h = 1/4$, $\phi_a = 1/2$ and $\phi_g = 3/4$:

$$\langle h \rangle_\nu = h_0 \left(\frac{32\mu_0^3 + 24\mu_0^2 + 12\mu_0 + 3}{32\mu_0^3 + 16\mu_0^2 + 4\mu_0}\right). \tag{2.59}$$

2.2.3 Characterising Forest Quantities under DET

Using our derived formulas that describe the distribution of trees, we can further investigate how a quantity (e.g. biomass or growth-rate) may vary purely in terms of population and without use of explicit mass space.

It is possible to get the CDF of an allometric quantity, equation (2.43), in terms of the CDF of the number density, equation (2.32). Firstly we must invert equation (2.32) to find:

$$\frac{\mu_0}{1-\phi_g}\left(\frac{m}{m_0}\right)^{1-\phi_g} = \frac{\mu_0}{1-\phi_g} - \ln\{1 - F_n\}. \tag{2.60}$$

Substituting into equation (2.43) gives:

$$F_z = 1 - \frac{\Gamma\left(\frac{\phi_z}{1-\phi_g}+1, \frac{\mu_0}{1-\phi_g} - \ln\{1-F_n\}\right)}{\Gamma\left(\frac{\phi_z}{1-\phi_g}+1, \frac{\mu_0}{1-\phi_g}\right)}. \tag{2.61}$$

Equation (2.61) gives us a dimensionless understanding of where forest quantities lie in terms of the cumulative population ranked by size. We look at carbon density, growth and coverage with $\mu_0 = 0.235$, $m_0 = 1\mathrm{kgC}$, $g_0 = 0.2\mathrm{kgC\ yr^{-1}}$ and $a_0 = 0.5\mathrm{m}^2$ along with $\phi_g = 3/4$, $\phi_a = 1/2$. The carbon density is the most unequal quantity, followed by growth, with coverage being more equally distributed across population (Figure 2.5.a).

For an estimate of a quantity inequality we can use the Gini coefficient - a

measure that economists use for wealth or income equality. The definition looks at the area under the curve of F_z versus F_n, and subtracting it from the line of equality - where there is direct proportionality between quantity and population (Dorfman, 1979):

$$\mathrm{GINI} = 1 - 2\int_0^1 F_z dF_n. \tag{2.62}$$

If a forest quantity is only within a small segment of the population the integral on the right hand-side of equation (2.62) drops to zero, $\mathrm{GINI} \to 1$, indicating perfect inequality. If a quantity is shared equally between the population, $\mathrm{GINI} \to 0$, perfect equality. The Gini coefficent has been used to investigate biomass distributions within rainforests (Weiner and Solbrig, 1984), and is especially of interest in forestry management and remote sensing (Lexerød and Eid, 2006; Pach and Podlaski, 2015; Valbuena et al., 2016). The Gini coefficient is a useful metric to understand how natural or close to equilibrium a forest is. Forest plantations of even-age stands will have initially have a greater Gini coefficient than natural forests, before transitioning into a more natural state (Kadavỳ et al., 2017).

To find the Gini coefficient of an allometric quantity, we must first integrate equation (2.61) with respect to F_n between 0 and 1. The integral of equation (2.61), is given as:

$$\int_0^1 F_z dF_n = \int_0^1 1 - \frac{\Gamma\left(\frac{\phi_z}{1-\phi_g} + 1, \frac{\mu_0}{1-\phi_g} - \ln\{1-F_n\}\right)}{\Gamma\left(\frac{\phi_z}{1-\phi_g} + 1, \frac{\mu_0}{1-\phi_g}\right)} dF_n. \tag{2.63}$$

Using the substitution:

$$\begin{aligned} u = \ln\{1-F_n\}, \quad F_n = 1 - \exp\{u\}, \\ dF_n = -\exp\{u\}du, \quad u_{F_n=0} = 0, \quad u_{F_n=1} = -\infty, \end{aligned} \tag{2.64}$$

we get:

$$\int_0^1 F_z dF_n = [F_n]_0^1 + \int_0^{-\infty} \frac{\Gamma\left(\frac{\phi_z}{1-\phi_g} + 1, \frac{\mu_0}{1-\phi_g} - u\right)}{\Gamma\left(\frac{\phi_z}{1-\phi_g} + 1, \frac{\mu_0}{1-\phi_g}\right)} \exp\{u\}du \tag{2.65}$$

The definition of the indefinite integral of a incomplete gamma function, with con-

stants, c, is given by:

$$\int \Gamma(c_1, c_2 - x)dx = (c_2 - x)\Gamma(c_1, c_2 - x) + \Gamma(c_1, c_2 - x) + c_3. \tag{2.66}$$

Using integration by parts for:

$$\int \Gamma(c_1, c_2 - x) \exp\{x\}dx = \Gamma(c_1, c_2 - x) \exp\{x\} + \int \exp\{2x - c_2\} (c_2 - x)^{c_1 - 1} dx, \tag{2.67}$$

where by the definition of the original gamma function (2.36) (and another substitution $u = c_2 - 2x$) gives us:

$$\int \Gamma(c_1, c_2 - x) \exp\{x\}dx = \Gamma(c_1, c_2 - x) \exp\{x\} - 2^{-c_1} \exp\{c_2\}\Gamma(c_1, 2c_2 - 2x) + c_3. \tag{2.68}$$

Substituting equation (2.68) into equation (2.65) gives us:

$$\begin{aligned}\int_0^1 F_z dF_n = 1 + \frac{1}{\Gamma\left(\frac{\phi_z}{1-\phi_g} + 1, \frac{\mu_0}{1-\phi_g}\right)} \Bigg[\Gamma\left(\frac{\phi_z}{1-\phi_g} + 1, \frac{\mu_0}{1-\phi_g} - u\right) \exp\{u\} \\ -2^{-\frac{\phi_z}{1-\phi_g}-1} \exp\left\{\frac{\mu_0}{1-\phi_g}\right\}\Gamma\left(\frac{\phi_z}{1-\phi_g} + 1, 2\left(\frac{\mu_0}{1-\phi_g} - u\right)\right)\Bigg]_0^{-\infty},\end{aligned} \tag{2.69}$$

which simplifies to:

$$\int_0^1 F_z dF_n = 2^{-\frac{\phi_z}{1-\phi_g}-1} \exp\left\{\frac{\mu_0}{1-\phi_g}\right\} \left(\frac{\Gamma\left(\frac{\phi_z}{1-\phi_g} + 1, \frac{2\mu_0}{1-\phi_g}\right)}{\Gamma\left(\frac{\phi_z}{1-\phi_g} + 1, \frac{\mu_0}{1-\phi_g}\right)}\right). \tag{2.70}$$

Therefore the Gini coefficient of a allometric quantity under the assumption of DET is given as:

$$\text{GINI} = 1 - 2^{-\frac{\phi_z}{1-\phi_g}} \exp\left\{\frac{\mu_0}{1-\phi_g}\right\} \left(\frac{\Gamma\left(\frac{\phi_z}{1-\phi_g} + 1, \frac{2\mu_0}{1-\phi_g}\right)}{\Gamma\left(\frac{\phi_z}{1-\phi_g} + 1, \frac{\mu_0}{1-\phi_g}\right)}\right). \tag{2.71}$$

Figure 2.5 demonstrates how a power-law quantity like coverage, growth and carbon biomass varies with population. The figure also plots the fitted values of ϕ_g and $\mu_{1\text{kgC}}$ for the RAINFOR sites (Moore et al., 2020). We can see from figure 2.5, that $\phi_g = 3/4$ and $\mu_{1\text{kgC}} = 0.235$ captures the distribution of quantities implied in the fitted sites. In panel 2.5.b, the total carbon density inequality is relatively stable, with most of mass density being in the top 5% of largest individuals for the

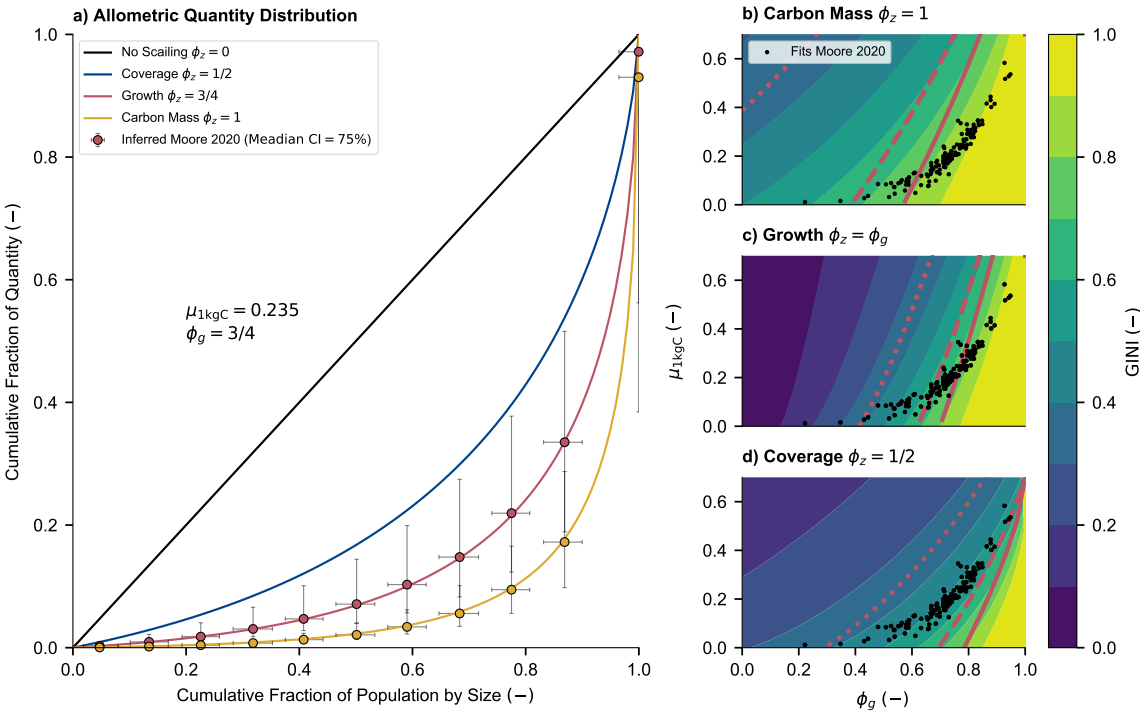

Figure 2.5: The forest quantity distribution from DET and the allometric integrals. Panel (a) shows how the cumulative fraction of plants ranked by size varies with the cumulative fraction of no scaling or the "line of equality" (black line, with $\phi_z = 0$), coverage (blue line, $\phi_z = 1/2$), growth (red line, $\phi_z = 3/4$) and carbon mass (yellow line, $\phi_z = 1$) across the size-structure using equation (2.61). The continuous lines are made under the assumption of $\phi_g = 3/4$ and $\mu_{1\mathrm{kgC}} = 0.235$, while the coloured dots are the corresponding two parameter (ϕ_g and $\mu_{1\mathrm{kgC}}$ fits across the RAINFOR sites from Moore et al. (2020), bars indicate the scope of 75% of the range of the binned outputs. Panels (b-c) show how the Gini equality coefficient varies with respect to $\mu_{1\mathrm{kgC}}$ and ϕ_g for carbon mass (b), growth (c) and coverage (d). The red line indicate where at least 50% of the quantity is in the top 5% (solid), 10% (dashed) and 25% (dotted) of the largest individuals.

RAINFOR sites.

There is significantly more variability of inequality for growth density than for carbon density. The variability is partly due to the fitting method employed by Moore et al. (2020), with the two parameter fit allowing ϕ_g to vary, as opposed to carbon density where ϕ_z always equal to 1 (i.e. carbon density perfectly correlates with carbon density). With a steeper slope for increasing ϕ_g (Figure 2.5.c). From the Gini relationship, equation (2.71), and figure 2.5 we can conclude that in general, the greater the size-scaling of growth rate or the allometric variable, or increases in longevity; $\mu_0 \to 0$, the more the ecosystem quantity is attributable to the largest individuals.

2.3 Conclusion

This chapter explores how trees are distributed through size and space. The sub-grid distribution of forest patches and gaps follows a power-law distribution, and could potentially be parametrised with respect to tree cover through percolation theory (Figure 2.1). The metabolic scaling of growth and size-invariant mortality under Demographic Equilibrium Theory appears sufficient to describe large datasets of tree inventories (Moore et al. (2018, 2020) and figures 2.2 & 2.3). The Weibull distribution of DET can be integrated with allometric equations to find relationships for the macroscopic qualities of a forest; such as total carbon density or average plant height. These relationships demonstrate how such quantities vary with tree population ordered against size. Figure 2.5 suggests that allometric variables within forests, such as the carbon density, are weighted towards larger trees. The rule that at least 50% of biomass being in the top 10% of largest individuals, seems to hold across the fitted South American RAINFOR data. As outlined in figure 2.5 and later in chapter 4, disturbances which target the largest individuals will disproportionately affect the total ecosystem carbon density and growth.

3 Robust Ecosystem Demography: a parsimonious approach to modelling vegetation dynamics

Rationale for Chapter

The results of the previous chapter suggests that at big enough scales, forest demography adheres to the assumptions of Demographic Equilibrium Theory (DET). Given this, and the complexities of using patch-age as a dimension, we explore the dynamic implementation of the DET, by relying on the Fokker-Planck and Metabolic Scaling Theory we dynamically update changes in the forest size structure.

This chapter was adapted from the RED model paper (Argles et al., 2020).

3.1 Background

Within the context of modelling vegetation at a global level, there is a trade-off between the complexity of ecological process representation and the necessity of parsimony at scale (Fisher et al., 2018). DGVMs range from the simplistic, older, top-down approaches to that of complex individual-based DGVMs. For example, in the first instance the TRIFFID model (Cox, 2001) simulates the fractional area of each Plant Functional Type (PFT) using phenomenological Lotka equations. The benefit of the TRIFFID approach is its simplicity and robustness. However, the model suffers from the lack of size representation and other processes which results in the over-estimation of regrowth time (Burton et al., 2019). In the second-instance, individual based models can explicitly represent a multitude of biological

and ecosystem processes at an individual plant level (Smith, 2001; Sato et al., 2007). The benefit of this is that size-dependent physiology and spatial heterogeneity can be explicitly represented. For example, SEIB-DGVM estimates light interception through three-dimensional crowns of individuals (Sato et al., 2007). However, multiple ensemble-members are often needed to construct meaningful forest statistics, which makes such models computationally expensive to run at large scales.

Compromises between the complexity of individual-based and top-down DGVMs exist as a class of tree cohort 2-d models. In the ED model (Moorcroft et al., 2001; Medvigy et al., 2009) the tree population is partitioned between patch disturbance and biomass classes allowing for the scaling of process to be represented in both age and size. ED2 can realistically model forests around the world (boreal, rainforest and temperate) (Medvigy et al., 2009; Fisher et al., 2018). However, parameterisation of competition within cohort DGVMs can result in a wide spread of outcomes when simulating climate change (Fisher et al., 2010; Scheiter et al., 2013). In Fisher et al. (2010), in the ED model the ecosystem carbon density across the Amazon was particularly sensitivity to competition and mortality parameters for HADCM3-LC projections.

In a similar vein other models have limited the number of cohort dimensions. The POP model (Haverd et al., 2014), uses stand-age cohorts as the dimension for population dynamics, every time-step applying crowding and resource limited mortality rates. Another example is the ORCHIDEE-MICT (Yue et al., 2018), which disaggregates the populations of a PFT into patch cohort functional types, with transitions between cohorts diagnosed when the average basal diameter passes a threshold.

The response of the land surface to climate change is a key uncertainty in climate projections. Ambitious climate targets also rely on land management practices such as reforestation and afforestation to increase the storage of carbon on land. Area-Averaged Dynamic Global Vegetation Models (DGVMs) attempted to model the the land surface in terms of bulk properties such as mean vegetation cover, vegetation carbon and leaf area index. These models lack information about the plant size-distribution, which compromised their ability to represent recovery from disturbance and the impact of land management. Providing useful guidance on these issues requires improved DGVMs which can repres-

ent changes in tree size distributions within forests (so called 'demography'). A number of much more sophisticated second-generation DGVMs are now under development. These models often explicitly simulate the number of plants within different size or mass classes, and on different patches of land, which are defined by the time since a disturbance event. Two dimensional cohort models are therefore in principle able to simulate variations in plant number density as both a function of patch age and plant size. However, this completeness is at the expense of much computational and parameter complexity. Our objective is to build a parameter sparse one-dimensional cohort DGVM that is focused on the plant size dimension. Therefore, we introduce the Robust Ecosystem Demography (RED) DGVM in the next sections.

3.2 Model Description

A full list of variables, parameters and units are given in Table 3.1.

Table 3.1: RED Model variables, parameters and units

Symbol	Definitions	Units
	Dimensions	
t	Time	year
m	Carbon mass of an individual within a PFT	kgC
	ESM Inputs	
P	Total assimilate of Net Primary Productivity minus local (leaves, wood and roots) litterfall	$\mathrm{kgC\ m^{-2}\ yr^{-1}}$
γ_{d}	Disturbance mortality rate, the fraction of population dying over a year due to explicitly modelled reasons	$\mathrm{yr^{-1}}$
	Individual	
m_0	Lowest/sapling mass boundary	kgC
g	Structural growth of an individual at a given mass and time	$\mathrm{kgC\ yr^{-1}}$
g_0	Structural growth of an individual at the lowest mass boundary at a specific time	$\mathrm{kgC\ yr^{-1}}$
a	Crown area of an individual at a given mass	$\mathrm{m^2}$
a_0	Crown area of an individual at the lowest mass boundary	$\mathrm{m^2}$
ϕ_g	Constant describing the power law scaling of structural growth across mass	$-$
ϕ_a	Constant describing the power law scaling of crown area across mass	$-$
α	The fraction of total growth going into seedling recruitment	$-$

Symbol	Definitions	Units
	Cohort	
n	Number density across mass space, the derivative of N with respect to mass	$(\mathrm{kgC})^{-1}\mathrm{m}^{-2}$
N	Number density	m^{-2}
G	Growth density	$\mathrm{kgC\ m^{-2}\ yr^{-1}}$
ν	The fractional coverage	$-$
γ	Mortality rate, the summation of the baseline and additional mortalities across mass	yr^{-1}
γ_b	Baseline mortality rate, the fraction of population dying over a year due to non-explicitly modelled reasons	yr^{-1}
s	The fraction of space available for seedlings	$-$
F	The flux of population density over time	$\mathrm{m^{-2}yr^{-1}}$
Λ_d	Demographic litter, the loss of carbon due to competition and mortality	$\mathrm{kgC\ m^{-2}\ yr^{-1}}$
M	Biomass density	$\mathrm{kgC\ m^{-2}}$
$c_{k,l}$	Competition coefficient, the fraction a PFT, k, that is shaded by the canopy of PFT l	$-$
	Equilibrium	
μ_0	The boundary turnover parameter - the ratio of mass lost to gained due to growth in the boundary mass class	$-$
λ_i	The proportional population of the i^th class to the $i^\mathrm{th}-1$ class at equilibrium	$-$
eq	Subscript denoting a variable in equilibrium	$-$
	Numerical	
k,l	Indices representing the PFT number	$-$
i,j	Indices representing mass class number	$-$
I	The largest mass class	$-$
(k)	The current time-step	$-$
ξ	The size-scaling coefficient, where mass classes are defined as $m_j = \xi\, m_{j-1}$, with $\xi > 1$	$-$

3.2.1 Theory

The underlying theoretical model for RED is a continuity equation, for each PFT and spatial location, which describes the time-evolution of the number density n of plants per unit area per unit mass m, as described by the previous general equation (1.3) with $z \to m$:

$$\frac{\partial n}{\partial t} + \frac{\partial}{\partial m}\, n\, g = -\gamma\, n. \tag{3.1}$$

Here g is the growth rate and γ is the mortality rate of a plant of mass m. In general, g and γ could be any reasonable function of tree size. Equation (3.1)

is commonly known as the Fokker-Plank or Kolmogorov forward equation, it was applied to model population dynamics by Van Sickle in 1977 (Van Sickle, 1977). Plants at a given mass will grow across the size dimension at a "flux": $\partial ng/\partial m$, while the number of plants doing so will decrease due to the sink term: $-\gamma\, n$. For large-scale applications we make simplifying assumptions for these functions consistent with observed n from forest inventory data (Moore et al., 2018, 2020). By default we assume that γ is independent of plant mass, and that g follows a power-law of plant mass:

$$g = g_0 \left(\frac{m}{m_0} \right)^{\phi_g}. \tag{3.2}$$

Here g_0 is the growth rate of a plant with the reference mass, m_0. A value of $\phi_g = 3/4$ is assumed by default, consistent with the analysis of field-based measurements by Niklas and Spatz (2004). We also assume the scaling of plant canopy area a with plant mass:

$$a = a_0 \left(\frac{m}{m_0} \right)^{\phi_a}, \tag{3.3}$$

where $\phi_a = 1/2$ by default. Solutions for n can be integrated over mass to derive the total plant number, $N = \int_0^\infty n\, dm$, the total growth rate, $G = \int_0^\infty g\, n\, dm$, the total biomass, $M = \int_0^\infty m\, n\, dm$, and the fractional area covered $\nu = \int_0^\infty a\, n\, dm$.

3.2.2 Discrete Mass Classes

We wish to produce a model of vegetation demography that can be updated numerically and which explicitly conserves vegetation carbon, providing a constraint on the number of plants moving between mass classes in the discrete form. In order to do this we integrate equation (3.1) over finite mass ranges:

$$\frac{\partial N_i}{\partial t} + F_i - F_{i-1} = -\gamma\, N_i, \tag{3.4}$$

where i denotes the i^{th} mass class; F_i is the flux of plants growing out of the i^{th} mass class and into the $(i+1)^{th}$ mass class; F_{i-1} is the flux of plants growing out of the $(i-1)^{th}$ mass class and into the i^{th} mass class; and N_i is the number of plants per unit area in the i^{th} mass class. For clarity, equation (3.4) is deliberately presented as continuous in time at this stage, as the focus in this subsection is on discretization of the mass profile. The fully numerical version of RED, which includes discretization of time, is described in section 3.2.4.

For large-scale application in ESMs a primary concern is to ensure that the total vegetation carbon obeys carbon balance (i.e. only changes due to the net impact of total growth minus total mortality). Here we use that requirement to derive the functional form for F_i. The total vegetation carbon in each mass class is $M_i = m_i\, N_i$. The update equation for M_i is therefore equation (3.4) multiplied by m_i:

$$\frac{\partial M_i}{\partial t} + m_i\,(F_i - F_{i-1}) = -\gamma\, M_i, \tag{3.5}$$

where m_i is the mean mass of a plant in the i^{th} mass class, and g_i is the growth rate per plant of the i^{th} mass class [kgC yr^{-1} plant^{-1}]. The total carbon in the vegetation, M, is the sum of the carbon in each of the mass classes:

$$M = \sum_i M_i. \tag{3.6}$$

Thus the update equation for the total carbon is:

$$\frac{\partial M}{\partial t} + \sum_i m_i\,(F_i - F_{i-1}) = -\gamma\, M, \tag{3.7}$$

which can be rewritten as:

$$\frac{\partial M}{\partial t} + \sum_i F_i\,(m_i - m_{i+1}) = -\gamma\, M. \tag{3.8}$$

Therefore, in order to explicitly conserve carbon, the flux F_i must take the form:

$$F_i = \frac{N_i\, g_i}{(m_{i+1} - m_i)}. \tag{3.9}$$

Now substituting equation (3.9) into equation (3.8) gives:

$$\frac{\partial M}{\partial t} = \sum_i N_i g_i - \gamma\, M. \tag{3.10}$$

The first term on the righthand-side of this equation is the total carbon uptake due to growth, G, and the second term represents the total carbon loss due to mortality, which is the required carbon conservation equation.

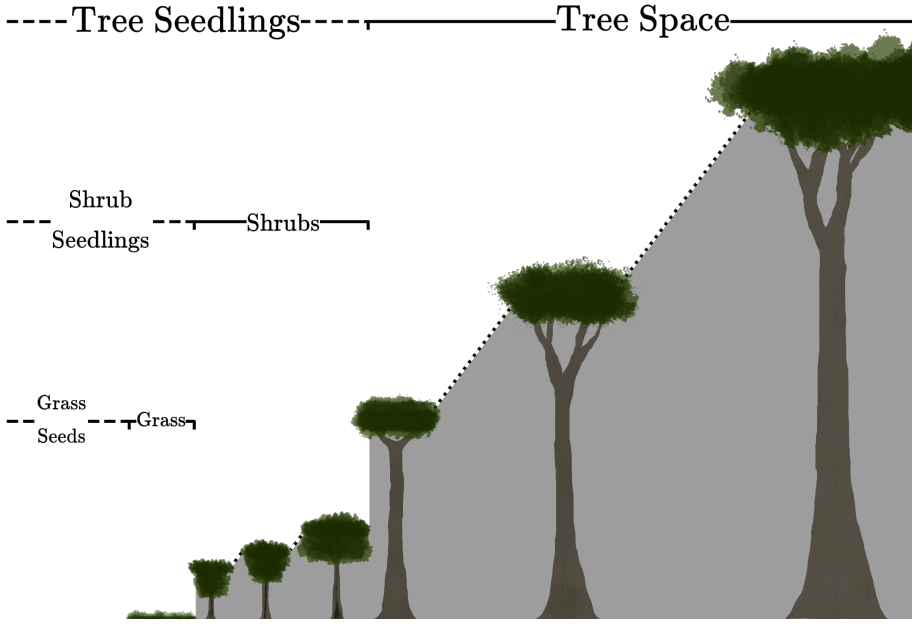

Figure 3.1: Schematic depicting the hierarchical PFT functional group regime within RED. Trees shade trees, shrubs and grasses. Shrubs shade shrubs and grasses, while grasses only shade grasses.

3.2.3 Seedling production and gap competition

To solve equation (3.4) we also require a lower boundary condition which represents the rate at which seedlings of mass m_0 are introduced into the cohort. Here we assume that a fixed fraction, α, of the total assimilate available to a PFT, P, is devoted to producing new seedlings, with the remainder $G = (1-\alpha)P$ being allocated to the growth of existing plants. Spreading is homogeneous across the entirety of the grid-box, but only seedlings established within 'unoccupied' space will survive to join the plant cohort. The net incoming flux of seedlings of mass m_0 is therefore:

$$F_0 = \frac{\alpha P}{m_0}\, s = \frac{\alpha}{(1-\alpha)}\, \frac{G}{m_0}\, s \tag{3.11}$$

where s is the fractional gap area available for seedlings. The definition of s is assumed to differ by PFT to reflect an underlying tree-shrub-grass dominance hierarchy, as shown schematically in Figure 1. Therefore, the rate of recruitment F_0 is the ratio of a fraction of the carbon assimilate allocated to reproduction, αP, and m_0, multiplied by the gap area s.

The space available to the seedlings of the k^{th} PFT is calculated from the area

fractions of the PFTs to which it is subdominant:

$$s_k = 1 - \sum_l c_{kl}\,\nu_l \tag{3.12}$$

where ν_l is the area fraction of the l^{th} PFT, and c_{kl} is the competition coefficient for the impact of PFT l on PFT k. If PFT l is within the same plant functional group (trees, shrubs or grasses) as PFT k, or dominant over it, $c_{kl} = 1$. If PFT k is dominant over PFT l, $c_{kl} = 0$ (Figure 3.1). This 'gap' boundary condition results in there being no equilibrium solution where the amount of coverage exceeds 1. Doing so would halt the recruitment flux such that mortality processes would bring the fractional coverage back below unity. This is a similar competition regime to the Lotka-inspired TRIFFID model (Cox, 2001), and allows for the co-existence between inter-functional groups (trees, shrubs and grasses) of PFTs. For instance, a PFT such as Broadleaf Deciduous Tree can co-exist with a Deciduous Shrub and C3 Grass, but not necessarily with another tree PFT. The hierarchy also enables the simulation of succession during regrowth. Faster growing species of grasses will not be able to expand into space occupied by trees and shrubs, unless there is space created by disturbance. A summary of the competition coefficients is given in table 3.2.

Table 3.2: Competition coefficients assumed for different plant functional groups. A more detailed example of this is given for specific PFTs in table 3.3.

		l		
c_{kl}		Trees	Shrubs	Grasses
k	Trees	1	0	0
	Shrubs	1	1	0
	Grasses	1	1	1

3.2.4 Coupling to Earth System Models

RED updates plant size distributions, biomass, and fractional areal coverage for an arbitrary number of PFTs at each spatial location, and can be driven by variables provided by a land carbon cycle model, ESMs, or observations (see Figure 3.2). For each PFT, the minimum required input is a time-series of net carbon assimilate, P, defined as the difference between Net Primary Productivity, Π_{NPP}, and local litter production due to turnover of leaves, stems and roots carbon pools,

Λ_{l}:

$$P = \Pi_{\mathrm{NPP}} - \Lambda_{\mathrm{l}}. \tag{3.13}$$

We apply the $m^{3/4}$ scaling to P. We therefore implicitly assume the same scaling for both GPP and plant respiration. This is consistent with observations suggesting that plant production also scales approximately as $m^{3/4}$ (Enquist et al., 1998; Niklas and Enquist, 2001). Where available, additional mortality due to disturbance events such as droughts, fires and anthropogenic deforestation, γ_{d}, can be added to the size-invariant baseline mortality rates, γ_{b}, for each PFT:

$$\gamma = \gamma_{\mathrm{b}} + \gamma_{\mathrm{d}}. \tag{3.14}$$

Disturbance rates γ_{d} can in principle be both PFT-dependent and mass-dependent (e.g. to capture forestry practices). Indeed DGVMs, such as LM3-PPA (Weng et al., 2015), use a variety of functions for mortality across mass, including a size-invariant mortality baseline.

The input values of net assimilate for each PFT, P, define the total structural growth rate, $G = (1 - \alpha)\, P$, and the seedling flux F_0, via equation (3.11), using PFT-specific values of the parameter α (see table 3.3). The definition of the total structural growth rate at a given time-step is:

$$G = \sum_i N_i\, g_i. \tag{3.15}$$

This can be combined with the growth-scaling given by equation (3.2), to derive the reference growth rate, g_0, from the net assimilate, P, which is a driving input:

$$g_0 = \frac{(1 - \alpha)\, P}{\sum_i N_i \left(\frac{m_i}{m_0}\right)^{\phi_g}}, \tag{3.16}$$

this in turn enables the growth rate of each mass class to be calculated using equation (3.2). Equation (3.16) has been used in a different form in the POP model (Haverd et al., 2014), to infer carbon increment across size. For each PFT, the number of plants in mass class, N_i, is updated using a discretised form of

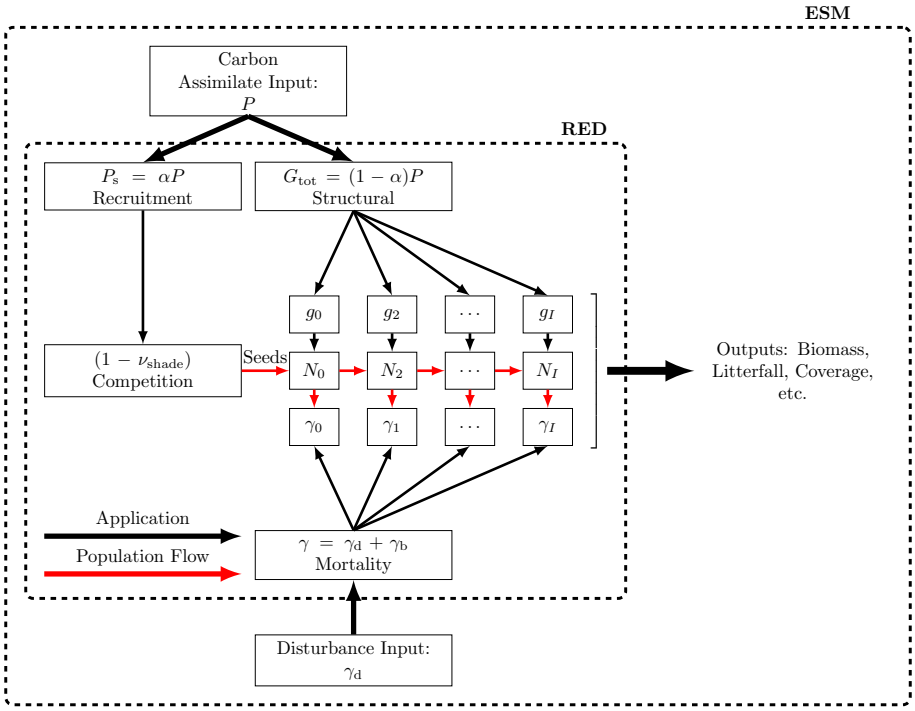

Figure 3.2: Schematic of RED coupled to an ESM or land carbon cycle model. RED is driven by a time-series of net carbon assimilate, P, which is then split between seedling production, $\alpha\, P$, and the growth of existing plants, $G = (1-\alpha)\, P$. The seedling flux is limited by the available free space, s. Additional mortality rates diagnosed from disturbance models, $\gamma_{\rm d}$, can be added on to an assumed baseline mortality, $\gamma_{\rm b}$, as a function of both PFT and mass class. Red arrows describe the direction of number density, while black arrows show separate model applications, such as disaggregation of the carbon assimilate during the model call.

equation (3.4):

$$N_i^{(j+1)} = N_i^{(j)} + \Delta t \left(F_{i-1}^{(j)} - F_i^{(j)} - \gamma^{(j)}\, N_i^{(j)} \right), \tag{3.17}$$

where Δt is the RED time-step (typically 1 month), and the superscript $^{(j)}$ denotes the j^{th} time-step. Our results are robust to changes in model timestep so long as the timestep remains small compared to the characteristic timescales associated with regrowth; $m_0/g_0 \sim 4\text{yr}$, and plant mortality; $1/\gamma \sim 20\text{yr}$. The lower boundary seedling flux is calculated from equation (3.11) using equation (3.12). We impose a zero-flux condition out of the upper mass class, under the assumption that there will be enough mass classes to ensure that this flux is negligible. However, to ensure carbon conservation on the land we add any plants that grow out of the upper mass class into a demographic litterfall term for each PFT, which is a RED output. This demographic litterfall term, Λ_d, keeps track of the carbon lost from

the vegetation due to competition, mortality and the carbon in any such plants that grow out of the largest resolved mass class (class I):

$$\Lambda_{\mathrm{d}} = \alpha\, P\,(1-s) + \sum_i \gamma_i\, M_i + g_I\, N_I. \tag{3.18}$$

The first term on the righthand-side of this equation represents carbon loss due to the shading of seedlings; the second term represents mortality of the resolved mass classes, which may include disturbance events; and the third term, which is normally very small, is the loss of vegetation carbon due to plants growing beyond the modelled mass classes. In order to initiate regrowth from bare soil, RED also assumes a minimum effective fractional area of each PFT. Where the net assimilate would be sufficiently negative to take the vegetation fraction below this minimum, the minimum value is maintained by subtraction from the demographic litter. The demographic litterfall term therefore represents the net addition litter production consistent with the prescribed net assimilate flux, the disturbance rate, and the change in vegetation carbon modelled by RED. When coupling to an ESM or land carbon model, the demographic litterfall term, Λ_d, should be added to the input local litterfall, Λ_l, as used in equation (3.13), to calculate the total litterfall flux into the soil/litter system.

3.2.5 Finding the discrete steady-state

The steady-state of the continuum model defined by equation (3.1) and equation (3.2) can be solved analytical for each PFT (Moore et al., 2018, 2020), and is equivalent with DET solutions presented in section 2.1.3. This analysis is also different from research by Moore et al. (2018) and Moore et al. (2020) as we have included the additional competitive mechanisms to close the system (see Closed Form Demographic Equilibrium Theory, CF-DET, presented in chapter 5 for more analysis). The shape of the mass distribution (Figure 2.4) and each of the equilibrium variables depend on the μ_0 ratio of plant mortality to growth, equation (2.24); $\mu_0 = \gamma m_0/g_0$. In order to initialise the numerical RED model in a drift-free initial state, we derive the steady-state of the discrete model, equation (3.17), which will differ slightly from the continuum model for a finite number of mass classes.

To solve for the discrete model equilibrium, we start from the flow equation from equation (3.4) with the term $\partial N/\partial t \to 0$:

$$\gamma N_i + F_i = F_{i-1}. \tag{3.19}$$

Considering the population flux - equation (3.9), we find N_i in relation to the lower mass class, N_{i-1}:

$$N_i = N_{i-1}\left[\frac{g_{i-1}/(m_i - m_{i-1})}{g_i/(m_{i+1} - m_i) + \gamma}\right] = N_{i-1}\lambda_i, \tag{3.20}$$

assuming no population grows out of the top class, $F_I = 0\ \mathrm{yr}^{-1}$, λ_I is given as:

$$\lambda_I = \frac{g_{i-1}}{(m_i - m_{i-1})\gamma}. \tag{3.21}$$

λ_i can be simplified to depend only on μ_0, by using $\mu_0 = (\gamma m_0/g_0)$, equation (2.24) and applying the mass scaling of growth rates $g_i = g_0(m_i/m_0)^{\phi_g}$. We can show that λ_i and λ_I are:

$$\lambda_i = \frac{(m_{i-1}/m_0)^{\phi_g}\ m_0/(m_i - m_{i-1})}{(m_i/m_0)^{\phi_g}\ m_0/(m_{i+1} - m_i) + \mu_0}, \quad \lambda_I = \frac{(m_{i-1}/m_i)^{\phi_g}\, m_0}{(m_i - m_{i-1})\mu_0}. \tag{3.22}$$

An expression for the total stand density at equilibrium, N_{eq}, can be derived. Using equation (3.20), we can represent any population of mass class i in terms of the lowest mass class N_0:

$$N_i = N_0 \prod_{j=1}^{i} \lambda_j. \tag{3.23}$$

Therefore, when finding the total number of stands relative to N_0 we get:

$$N_{\mathrm{eq}} = N_0 X_N, \quad X_N = 1 + \sum_{i=1}^{I} \prod_{j=1}^{i} \lambda_j. \tag{3.24}$$

In a similar vein to section 2.2, let us assume a dummy allometric relationship and variable; $z = z_0(m/m_0)^{\phi_z}$. Instead of an integral, like equation (2.34), the total quantity, Z_{eq}, is given as a sum-product:

$$Z_{\mathrm{eq}} = z_0 \sum_{i=0}^{I} \left(\frac{m_i}{m_0}\right)^{\phi_z} N_i, \tag{3.25}$$

or in terms of z_0 and N_0:

$$Z_{\rm eq} = z_0 N_0 X_Z, \quad X_Z = 1 + \sum_{i=1}^{I} \left(\frac{m}{m_0}\right)^{\phi_z} \prod_{j=1}^{i} \lambda_j. \tag{3.26}$$

The discretised version of RED thus yields formulae for the coverage, $\nu_{\rm eq}$:

$$\nu_{\rm eq} = \sum_{i=0}^{I} N_i \, a_i = N_0 \, a_0 \, X_\nu, \tag{3.27}$$

the total equilibrium structural growth, $G_{\rm eq}$:

$$G_{\rm eq} = \sum_{i=0}^{I} N_i \, g_i = N_0 \, g_0 \, X_G, \tag{3.28}$$

and the equilibrium carbon density:

$$M_{\rm eq} = \sum_{i=0}^{I} N_i \, m_i = N_0 \, m_0 \, X_M. \tag{3.29}$$

Here X_N, X_G, X_ν and X_M, are functions of μ_0 and the mass binning; equation (3.26). The equations above are therefore define the equilibrium state of the discrete system for given values of N_0 and μ_0. The next step, as in chapter 5, is to combine with the reproductive and competitive constraints, equation (3.11). However, this time we are including additional PFTs in the shading term through the competition coefficients. In equilibrium, the rate of the recruitment of seedlings, equation (3.11), must balance the rate of loss of plants due to total mortality, $\gamma \, N_{\rm eq}$:

$$\gamma \, N_{\rm eq} = \frac{\alpha}{(1-\alpha)} \frac{G_{\rm eq}}{m_0} \, s. \tag{3.30}$$

Substituting in equation (3.24) and equation (3.28) yields a balance equation for the k^{th} PFT:

$$\left(\frac{\alpha}{1-\alpha}\right) \left(1 - \sum_{l} c_{kl} \, \nu_l\right) = \mu_0 \, \frac{X_N}{X_G}. \tag{3.31}$$

We can get the equilibrium fraction of a PFT, k, by rearranging the above equation, assuming $c_{kk} = 1$:

$$\nu_{{\rm eq},k} = 1 - \left(\frac{1-\alpha}{\alpha}\right) \mu_0 \frac{X_N}{X_G} - \sum_{l \neq k} c_{kl} \nu_l. \tag{3.32}$$

As the righthand-side of this equation depends only on prescribed constants and μ_0, equation (3.32) can be inverted (by numerical iteration) to estimate μ_0 for observed values of the PFT fractions, $\nu_k,\ \nu_l$, and an assumed value of α (see table 3.3). Once the value of μ_0 has been derived in this manner, it can be used to calculate X_ν, and therefore N_0 by inversion of equation (3.27):

$$N_0 = \frac{\nu_{\rm eq}}{a_0\, X_\nu}. \tag{3.33}$$

Equations (3.32) and (3.33), along with equation (3.24), allow us to define an initial equilibrium state, N_i, which is consistent with observed area fractions of each PFT. Furthermore, when paired with an estimate of the net carbon assimilate (from a model or observations), the μ_0 estimate can be converted into a map of the implied mortality, γ, by PFT. We demonstrate this capability globally in the next section.

3.3 Model Results

For these runs, the numerical RED model is set up to use the 9 PFTs which are currently used in JULES (Harper et al., 2018). This enables us to directly use driving data - time series of the rate of net assimilation, P - from a previous UKESM model simulation that includes JULES (Sellar et al., 2019). RED is integrated forward using a one month time-step and successive mass classes that differ by a multiplicative constant ξ, so that $m_i = \xi\, m_{i-1}$. The value of ξ was chosen to optimally fit the analytical equilibrium solutions assuming 10 mass classes for trees, 8 mass classes for shrubs and 1 mass class for grasses, assuming $\mu_0 = 0.25$ (see appendix A). Other PFT-specific parameters are assumed as summarised in table 3.3.

Table 3.3: List of PFT names and assumed allometric scaling parameters (m_0, a_0), seedling fraction (α) and competition coefficient ($c_{\mathrm{pft,j}}$). The growth allometry of trees and shrubs across size is assumed to follow Niklas and Spatz (2004) ($\phi_g = 3/4$, $\phi_a = 1/2$). The competition coefficients given describe which PFT functional group shades the current PFT, if $c_{\mathrm{pft,j}} = 1$, the PFT is shaded, otherwise it is not (Table 3.2).

Long name	Abbrev	Classes	Scaling (ξ)	α	$m_0(\mathrm{kgC})$	$a_0(\mathrm{m}^2)$	$c_{\mathrm{pft},j}$ Tree	Shrub	Grass
Broadleaf Evergreen Tree Tropical	BET-Tr	10	2.32	0.10	1.00	0.50	1	0	0
Broadleaf Evergreen Tree Temperate	BET-Te	10	2.32	0.10	1.00	0.50	1	0	0
Broadleaf Deciduous Tree	BDT	10	2.35	0.10	1.00	0.50	1	0	0
Needleleaf Evergreen Tree	NET	10	2.35	0.10	1.00	0.50	1	0	0
Needleleaf Deciduous Tree	NDT	10	2.32	0.10	1.00	0.50	1	0	0
Cool Season Grasses	C3	1	1.50	0.60	0.10	0.25	1	1	1
Tropical Grasses	C4	1	1.50	0.60	0.15	0.25	1	1	1
Evergreen Shrub	ESh	8	2.80	0.35	0.50	0.25	1	1	0
Deciduous Shrub	DSh	8	2.80	0.35	0.50	0.25	1	1	0

3.3.1 Global: Diagnosed Plant Mortality Rates

Here we use the analytical forms for the equilibrium state (Section 3.2.5) and observations of global vegetation cover, to diagnose the corresponding map of PFT-specific mortality rates. These mortality rates are therefore consistent with the current observed vegetation state, and rates of net assimilation (P) provided from UKESM (Sellar et al., 2019). The UKESM simulation provides NPP and local litterfall per unit area of each PFT. We multiply by PFT fraction to get the grid-box mean values required to drive RED (using ESA landcover data, as explained below). The observed maps of PFTs are provided by the ESA LC_CCI dataset

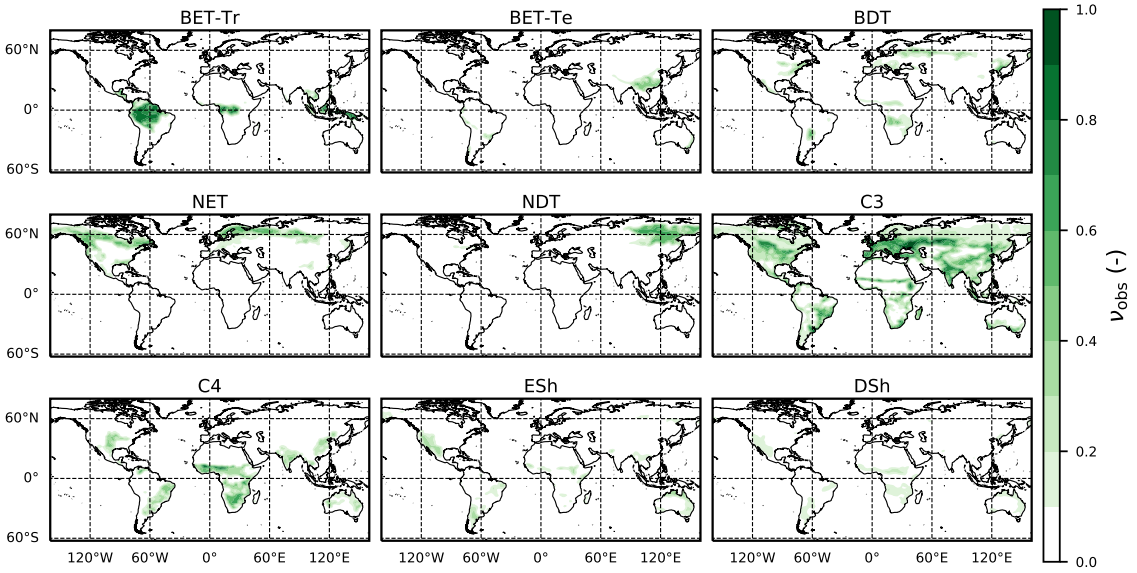

Figure 3.3: Observation-based dataset of the PFT area fractions for the nine JULES PFTs Harper et al. (2016) as listed in table 3.3. The observations for grass PFTs combines both natural and land-use fractions.

for 2008-2012 (Poulter et al., 2015), projected onto the 9 JULES PFTs by Harper et al. (2016) (Figure 3.3). Maps of the prescribed annual mean values of the rate of net assimilation (P) are shown in Figure 3.4.

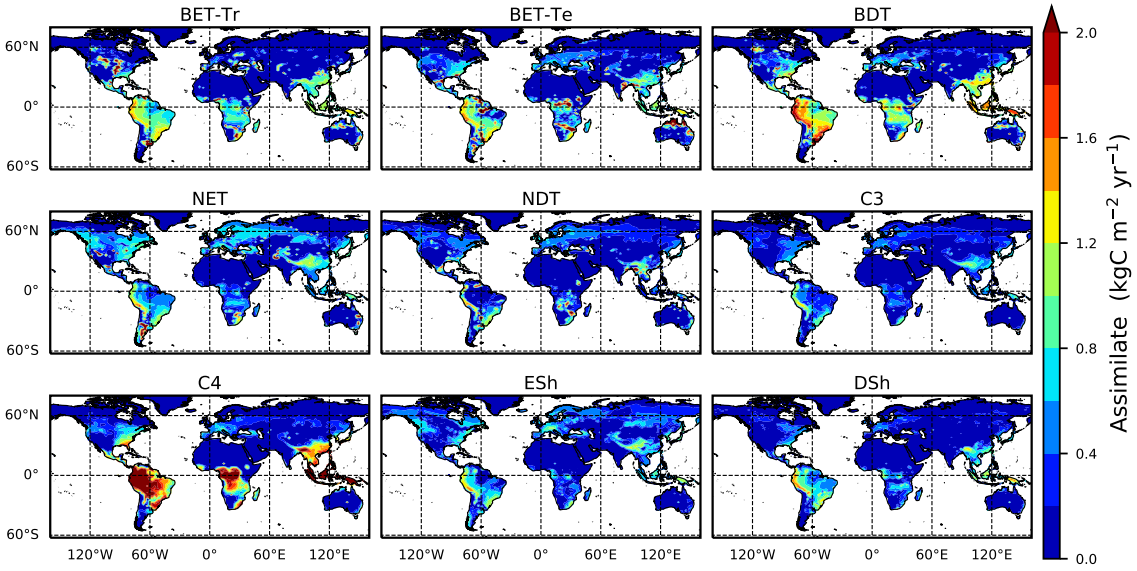

Figure 3.4: Mean net assimilate, P, per vegetation area from UKESM between 2000-2010, using equation(3.13). The mean is constructed by setting any negative growth rates to zero.

We use the procedure outlined in Section 3.2.5 to estimate spatially-varying values of μ_0 for each PFT, using equation (3.32), and then equation (3.33) to estimate

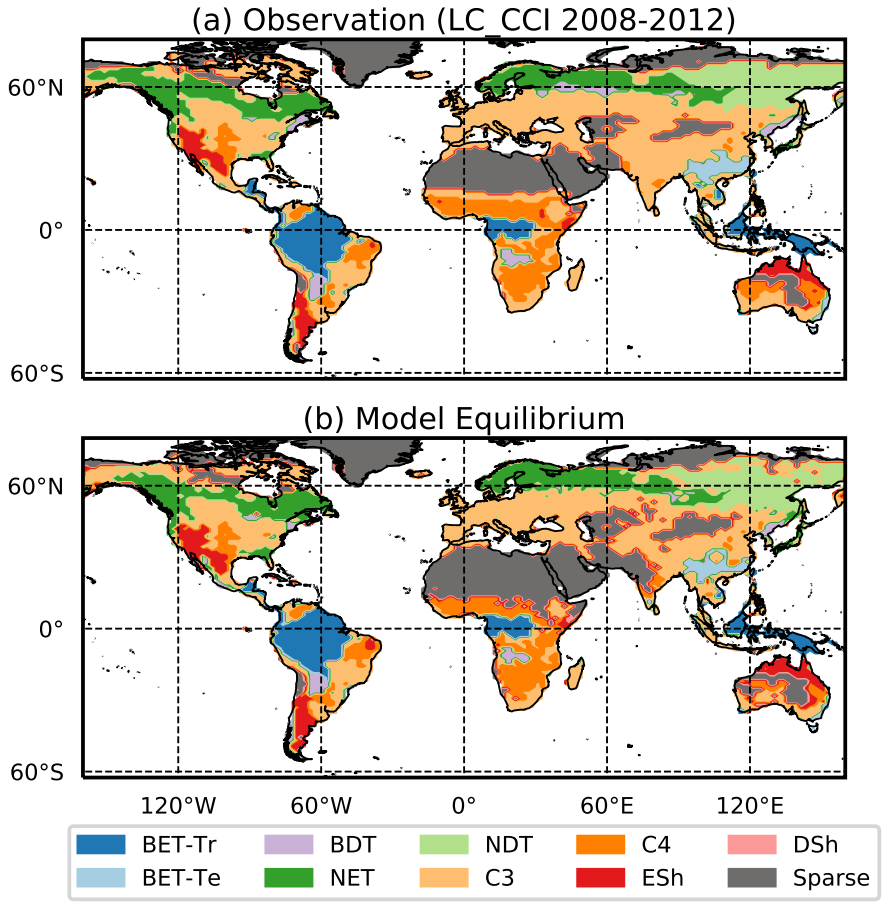

Figure 3.5: Maps of dominant PFT for (a) ESA LC_CCI dataset and (b) RED model equilibrium fractions. Sparse area is defined as where the total vegetation coverage is less than 10% (i.e. $\sum_k \nu_k < 0.1$).

N_0. This method successfully reproduces the ESA map of dominant PFT to good accuracy, as shown in figure 3.5 and table 3.4.

Table 3.4: Goodness of fits for the RED equilibrium coverages to the coverages from ESA LC_CCI dataset across PFTs. r represents the Pearson Correlation Coefficient, after weighting by the grid-box area to account for latitudinal variation of grid-box areas.

PFT	r	RMSE
BET-Tr	0.990	0.030
BET-Te	0.935	0.030
BDT	0.783	0.053
NET	0.905	0.051
NDT	0.928	0.033
C3	0.895	0.129
C4	0.818	0.088
ESh	0.854	0.051
DSh	0.525	0.049

The fit of the RED equilibrium vegetation coverage to the ESA observations is

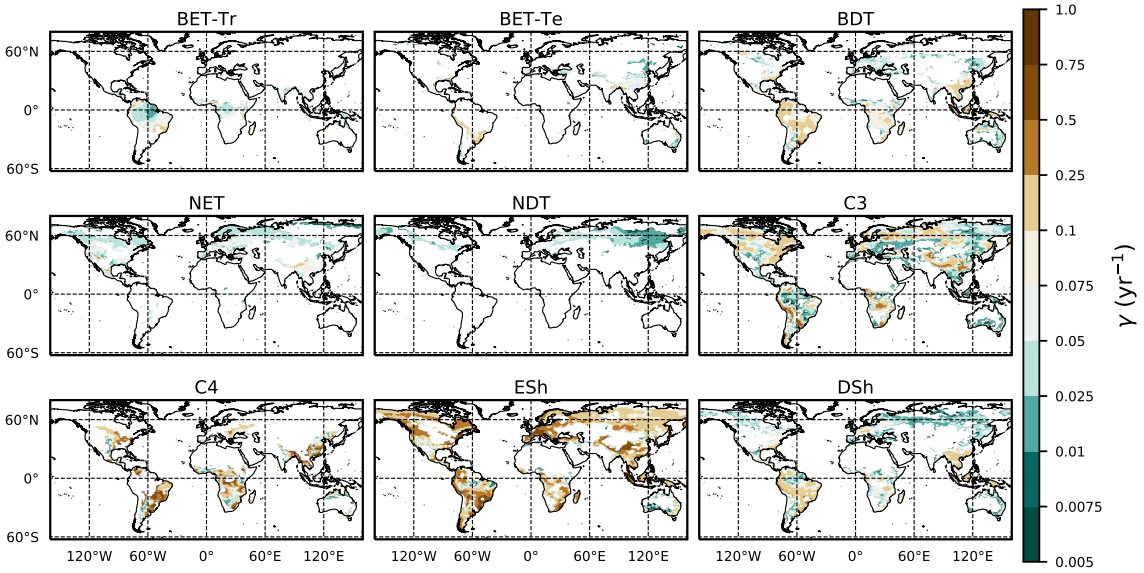

Figure 3.6: Diagnosed maps of mortality rates γ for each PFT, as required for consistency with the ESA observations and the UKESM growth rates with RED. White areas correspond with zero coverage and/or zero growth.

generally very good (Table 3.4). However, it is imperfect in some areas (e.g. Central Asia, Sahel) where the driving net assimilate from UKESM is zero or negative. Also, areas where the observational dataset indicates co-existing PFTs within the same vegetation class (e.g. broadleaf trees and needleleaf trees) are not well simulated by this first version of RED, which leads to competitive exclusion in the equilibrium state (see section 3.4). Since we now have diagnosed values of μ_0 and N_0, along with prescribed values of P, we can also diagnose the mean plant mortality rate γ, for each location and for each PFT, from equation (2.24) :

$$\gamma = \frac{\mu_0 \, g_0}{m_0}, \tag{3.34}$$

where g_0 is given by equation (3.16) combined with equation (3.20) and (3.22). Maps of γ values, derived in this way, are shown in Figure 3.6. The mortality rate derived is dependent on the assumed areal coverage and the total assimilate. A high coverage with a low growth rate will result in a compensating low diagnosed mortality rate (and vice-versa). Furthermore, the choice of α, equation (3.16), and m_0 also influence the diagnosed value of γ. An analysis of the sensitivity of the inferred value of γ to these factors is presented in Appendix B. Assuming $\pm 20\%$ uncertainty on assimilate, α, m_0 and $\pm 5\%$ on the coverage gives an uncertainty bound of $\pm 35\%$ on γ. Under the assumption that high coverages are indicative

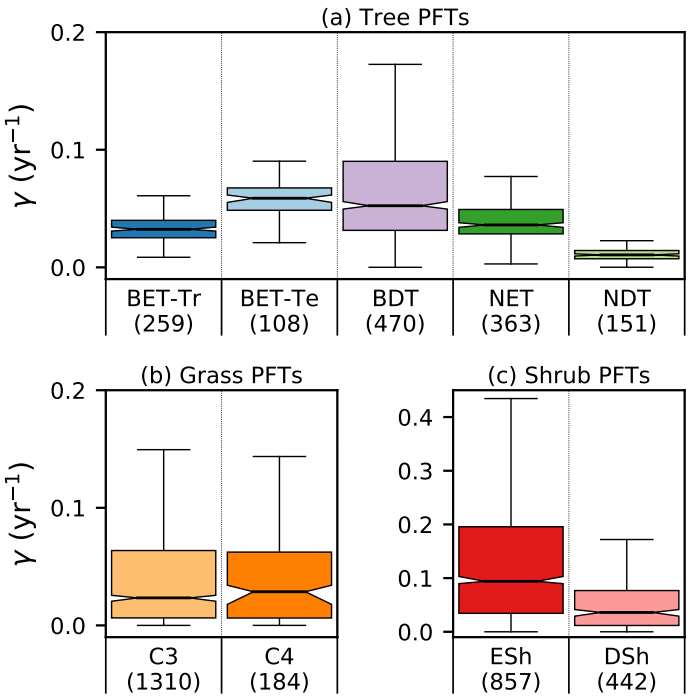

Figure 3.7: Diagnosed mortality rates for (a) trees, (b) grasses and (c) shrubs in the top quartile of coverage. Notches within the box represent the confidence bounds of the median. The confidence bounds are estimated using a bootstrap method. Bracketed numbers represent the number of grid-points.

of the baseline mortality for a given PFT, we take a sub-sample of the grid-boxes that are within the top quartile of non-zero coverages ($\nu_{\text{eq}} > 0.01$) (Table 3.5). The median μ_0 value diagnosed from the top quartile of BET-Tr of 0.232 (Table 3.5), is very close to the value calculated in our previous paper (Moore et al., 2020) of approximately 0.235 for all of South America using the RAINFOR sites.

Table 3.5: The area-weighted median values of observed coverage and driving net assimilate against μ_0 and γ for the upper quartile of grid-boxes for each PFT.

PFT	Area weighted median			
	ν_{obs}	P (kgC m^{-2} yr^{-1})	μ_0	γ (yr^{-1})
BET-Tr	0.793	0.731	0.232	0.032
BET-Te	0.402	0.349	0.340	0.059
BDT	0.238	0.143	0.377	0.052
NET	0.471	0.281	0.328	0.036
NDT	0.597	0.112	0.298	0.011
C3	0.566	0.124	0.163	0.023
C4	0.545	0.123	0.189	0.029
ESh	0.142	0.028	0.744	0.094
DSh	0.116	0.024	0.713	0.036

Site-level assessments of the rates of stand mortality within pan-tropical forests provide a range of background rates (Lugo and Scatena, 1996; Phillips, 1996;

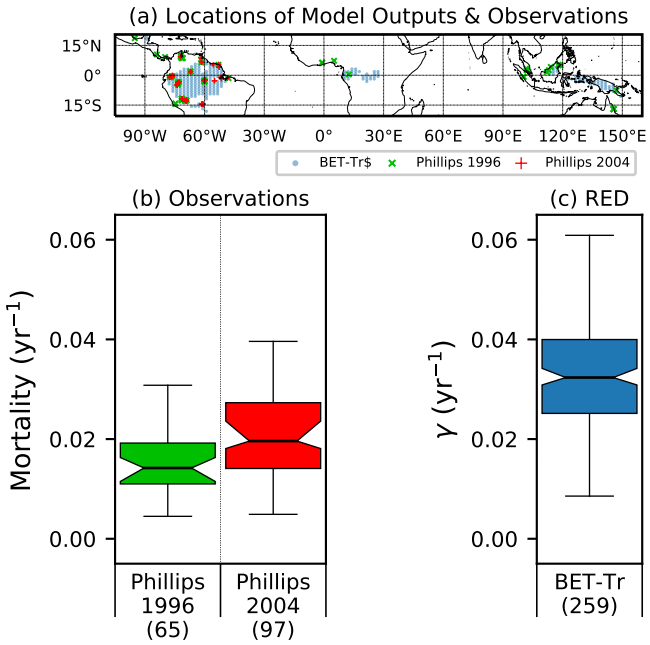

Figure 3.8: Comparison of observation-based estimates of tropical tree mortality (Phillips, 1996; Phillips et al., 2004) to γ values diagnosed from RED for the BET-Tr PFT (for the top 25% of fractions for this PFT). (a) location of observational sites (red and green crosses) versus the chosen RED grid-points (blue circles); (b) distribution of mortality across grid-boxes; (c) mortality distribution across the BET-Tr grid-points. Bracketed numbers in panel (b) represent the number of measurements, and in panel (c) the number of gridpoints.

Phillips et al., 2004). Phillips (1996) estimates mortality rates collected across 40 pan-tropical sites for tree sizes greater than $10 - 25$ cm dbh. Later work by Phillips et al. (2004) used the demographic data from the RAINFOR dataset of trees ≥ 10cm dbh. Using these site assessments, we can make a comparison to BET-Tr equilibrium mortality rates by looking at the values of γ in areas where we would expect to see old growth forests. We use the top 25% of coverages of the BET-Tr PFT to represent plausible areas of undisturbed forest. Figure 3.7 shows that the diagnosed baseline mortality rates are in reasonable agreement with these observational estimates for Amazonia. There is a need to better understand the influence of mortality arising from disturbance events such as droughts and fire in order to constrain model projections (Pugh et al., 2020). Here we investigate if the equilibrium mortality rates implicitly capture areas of disturbances, by comparing the mean tree mortality rate to fire and land-use surveys (the mean mortality is defined here by weighting grid-box γ values by grid-box fractional coverages). There are a number of surveys relating stand mortality in regions prone to wildfires (Swaine, 1992; Kinnaird and O'Brien, 1998; Peterson and Reich, 2001;

Van Nieuwstadt and Sheil, 2005; Prior et al., 2009; Staver et al., 2009; Brando et al., 2014). In a broad sense, post-fire mortality rates can range from $0.06\ \mathrm{yr}^{-1}$ to catastrophic rates around $0.8\ \mathrm{yr}^{-1}$ and can vary quite considerably depending on tree species, fire frequency and drought severity. The drought-fire interaction is responsible for significantly increasing mortality post-fire and can be a driving cause of regional die-back (Allen et al., 2010; Brando et al., 2014). Using the ESA FIRE_CCI dataset (Chuvieco et al., 2019) we can estimate the burnt vegetation fraction per year. Taking the average burnt vegetation fraction for the months between 2000 and 2010, and converting into annual burn rate we gain an estimate of fire severity.

Another key issue is anthropogenic land-use and land-use change (Nepstad et al., 2008; Haddad et al., 2015). Fragmentation of natural forests is understood to raise the mortality of the remaining forest and to decrease the overall resilience of the ecosystem (Esseen, 1994; Laurance et al., 1998; Jönsson et al., 2007). In order to maintain a near-constant agricultural fraction, regular disruption such as grazing is needed to prevent re-colonisation and secondary succession (Dorrough and Moxham, 2005; Van Uytvanck et al., 2008; Chaturvedi et al., 2012). We carry out a comparison with land-use using the 2000 ESA LC_CCI inferred crop coverages (Li et al., 2019).

In Figure 3.9, we see the derived observations for burn area (a) and crop fraction (b), along with the derived mean γ for the tree PFTs (c). From Figure 3.8 (d), we see that there are areas of large mortality ($\gamma > 0.075\ \mathrm{yr}^{-1}$) that do correspond to areas where we see large fire activity (burn rate $> 0.1\ \mathrm{yr}^{-1}$) and increased crop fraction (> 0.25). However, large burn rates are seen to overlap in parts of central Brazil around the Cernado region, Southern Africa and North Western Australia where fires are understood to play a significant part within the ecosystem (Coutinho, 1990; Medeiros and Miranda, 2008; Prior et al., 2009; Staver et al., 2009). There are also some areas of agriculture which correspond to deforestation, such as in the Atlantic forests of Brazil and in Indonesia (Higuchi et al., 2008; Curran et al., 2004). Areas of increased disturbances result in grasses and shrubs dominating (Figure 3.3).

Analysis of the RED equilibrium is an indirect approach to estimating tree mortality based on simple yet mechanistic principles of demography, and relying on few inputs (vegetation cover and assimilate). It is however conditional on the assumed

estimates of vegetation coverage and net rates of assimilation.

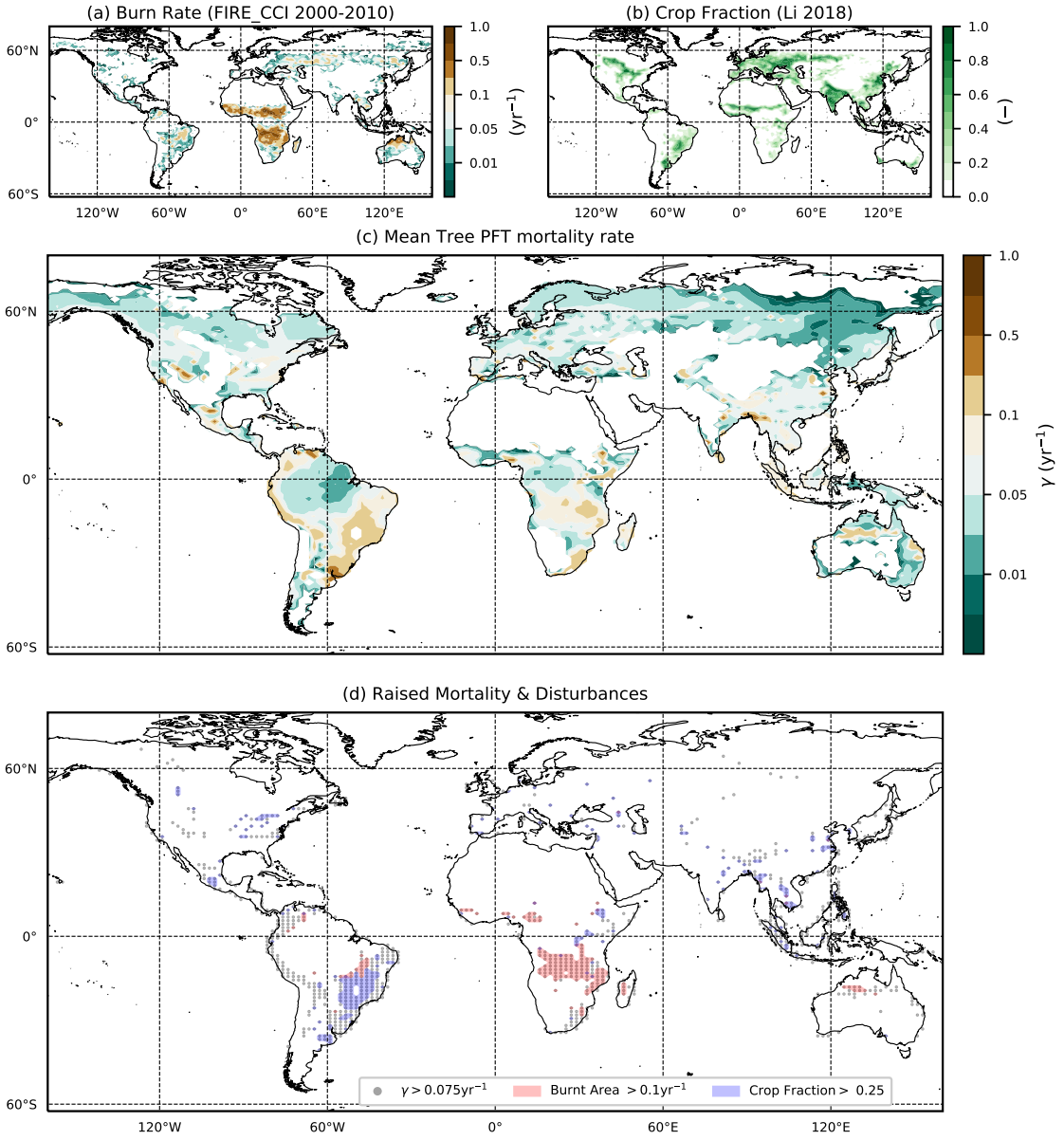

Figure 3.9: Comparison of diagnosed mortality rates, with observation-based maps of fire and land-use. (a) annual burnt area fraction from the ESA FIRE_CCI dataset; (b) crop fraction from the ESA LC_CCI 2000 dataset; (c) diagnosed mortality rate γ for the tree PFTs (BET-Tr, BET-Te, BDT, NET, NDT); (d) overlap of areas of higher tree mortality rates ($\gamma > 0.075\ \mathrm{yr}^{-1}$) with areas of fire (Burnt Area $> 0.1\ \mathrm{yr}^{-1}$) and agriculture (Crop Fraction $\geq 25\%$).

3.3.2 Dynamical Simulations

Local: Simulating Succession

In this subsection we demonstrate the vegetation successional dynamics simulated by RED in an idealised spin-up from bare-soil, for a grid-box at the edge of the Amazonian rainforest (Figure 3.10). We also simulate a separate run with the diagnosed equilibrium number density (from the previous section) as the initial condition. Under these circumstances, the diagnosed initial state is indeed the long-term equilibrium state, as evidenced by the horizontal dashed lines in panels a and b of Figure 3.10.

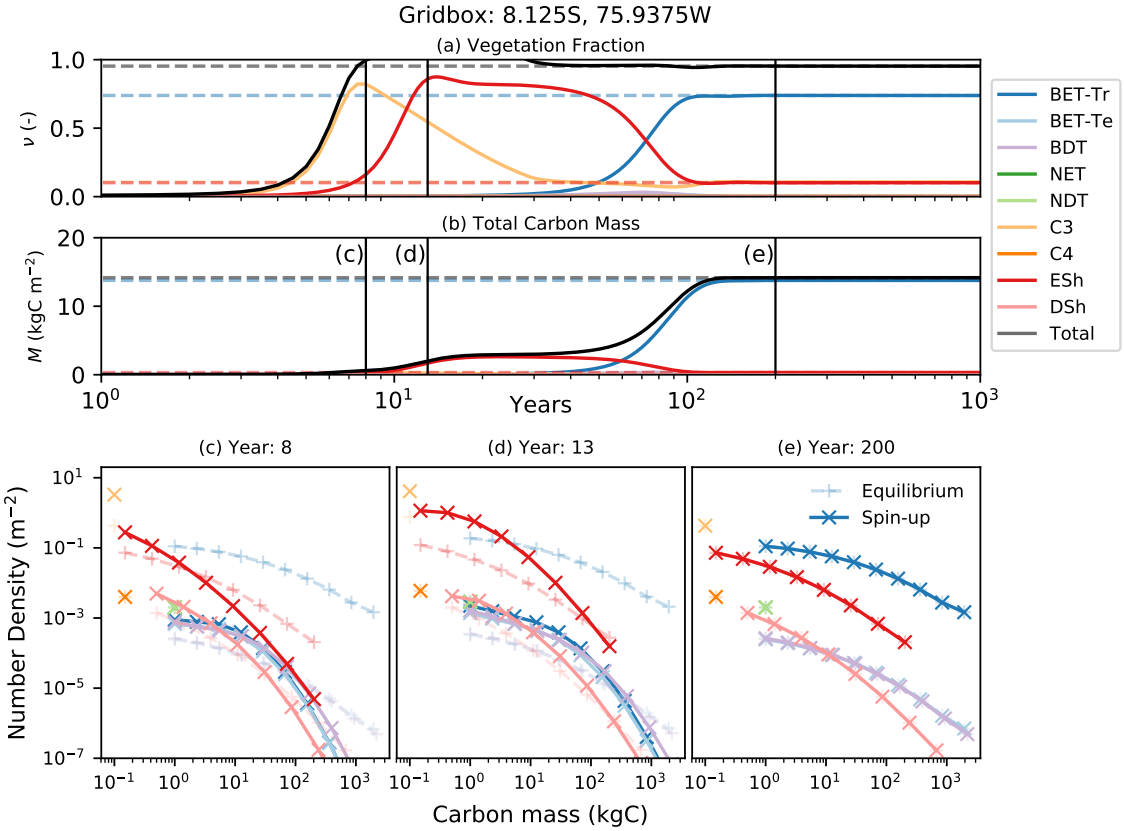

Figure 3.10: Dynamical runs of RED for a grid-box at the edge of the Amazonian rainforest, starting from bare soil (solid lines) and the diagnosed equilibrium state (dashed lines). (a) PFT fractions versus time; (b) biomass versus time; (c), (d) and (e) snapshots of the number density distribution of the PFTs across mass classes at different times. Lines marked as **+** are the equilibrium runs while **X** indicates the spin-up run. The ultimate steady-state is determined by the balance between recruitment and mortality; equation (3.11). Intra- and inter-PFT occurs here through the shading of seedlings, which implies that just a fraction of the gridbox (s, 'space' or 'gap' fraction) is available to grow seedlings, equation (3.12).

Faster growing grass PFTs dominate the grid-box within the first twelve years,

before being replaced by evergreen shrubs which shade the grass seedlings. Eventually, Broad-leaf Evergreen Tropical Trees replace much of the shrub and grass, on a timescale determined in large part by the parameter α and the reference mass class m_0. With the parameters used here, the vegetation fraction reaches close to its equilibrium value after about 100 years (panel (a)), but full spin-up of the biomass takes around 150 years (panel (b)).

The modelled evolution of number density versus mass distribution for each PFT is shown in panel (c) (after 6 years), panel (d) (after 13 years) and panel (e) (after 100 years), with the eventual demographic equilibrium profiles shown by the dashed lines. It is clear that grass PFTs are close to their demographic equilibrium after only 6 years, but tree PFTs need more than 100 years to reach equilibrium.

The dashed lines in Figure 3.10 represent a dynamical RED simulation from the diagnosed demographic equilibrium state. This state is derived using the methodology described in Section 3.2.5, with one significant change. The competition rules given by equation (3.12) and Table 3.2 result ultimately in equilibria which have a single dominate PFT in each class of co-competing types (trees, shrubs, grasses). To avoid drifts associated with the competitive exclusion of the subdominant PFTs in each vegetation class, we choose to initialise the dominant PFT to have the total area fraction of all the PFTs in that vegetation class.

Global: Spin-up from Bare Soil

Transient simulations of global vegetation will be the subject of a future paper, but in the final subsection of this paper we wish to demonstrate the utility of the semi-analytical equilibrium for initialisation of global model runs. Figure 3.11 shows the time-evolution of global mean PFT fractions and biomass from a global run driven by net assimilation rates from the UKESM model. Once again, two RED simulations are shown, one started from bare soil (solid lines) and the other from the semi-analytical equilibrium state (dashed lines). Using a constant assimilate rate (Figure 3.4) and the mortality distribution (Figure 3.7), we see convergence of these two runs, but only after more than 1000 years of simulated time. The ability to diagnose the equilibrium state therefore has the potential to reduce model spin-up time hugely, especially for Earth System Models (ESMs) applications.

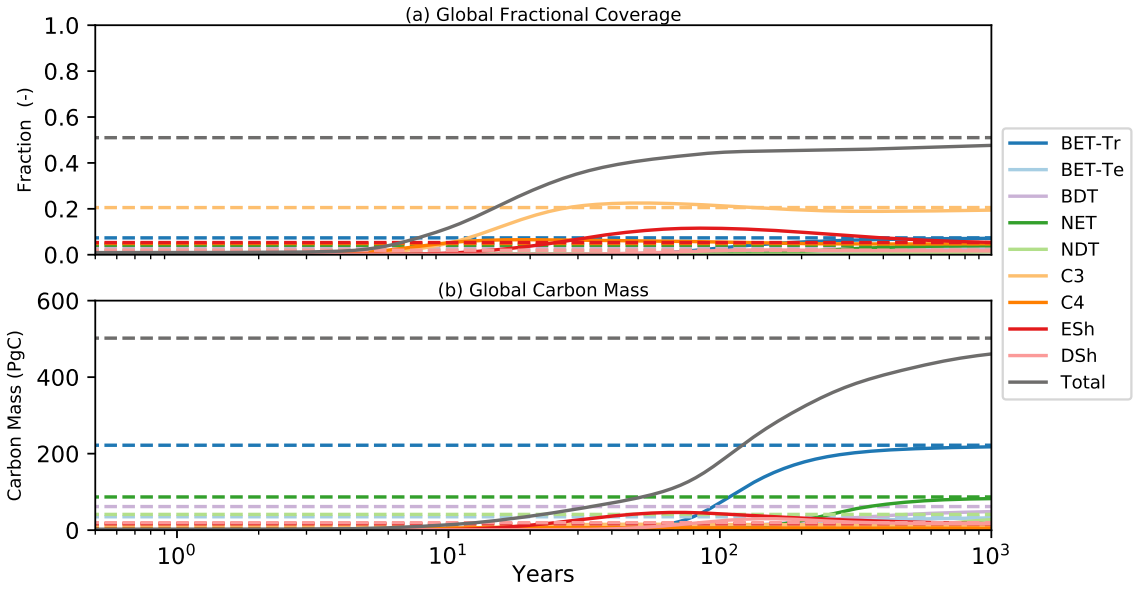

Figure 3.11: Global model spin-up from bare soil. As for figure 3.10, solid lines are spin-up from bare soil, dashed lines are the equilibrium instillation run. Panel (a) represents the fractional global coverage relative to the total land area; panel (b) represents the total biomass of the vegetation.

3.4 Discussion

Our previous work in evaluating demographic equilibrium theory for regional forest inventory datasets in North America (Moore et al., 2018) and using RAINFOR sites for South America (Moore et al., 2020), has provided the theoretical basis for the development of RED. In those studies we found that the tree size-distributions observed at a large-scale in forests can be satisfactorily understood in terms of demographic equilibrium in the size dimension alone. This is a reduction in complexity compared to other cohort models which are based on patch age, and yet an improvement in ecological fidelity compared to older phenomenological DGVMs such as TRIFFID (Cox, 2001). The modular design of RED allows for easy coupling to land-surface schemes, merely requiring the per unit grid-box total carbon assimilate rate and any additional mortality disturbance rates as inputs for each grid-box (Figure 3.2). In principle, RED allows scope for more complex tree size-dependent processes, although in this first study we chose to assume size-independent (but spatially varying) mortality rates for each PFT. Our previous work suggests that this is a good first-order assumption (Moore et al., 2018, 2020).

Internally within the model we make a number of simplifications. Firstly, the num-

ber density for each PFT is treated as a function of plant mass alone. This immediately eliminates the need to explicitly represent patches, and therefore removes age as an independent dimension. This is a distinct approach relative to cohort DGVMs which are based on patches defined by time since disturbance, such as the POP or ORCHIDEE-MICT models (Haverd et al., 2014; Yue et al., 2018). Secondly, we assume that plant growth rates vary as a power of plant mass. By default we assume a power of $\phi_g = 3/4$, which is consistent with Metabolic Scaling Theory (Enquist et al., 1998) and the empirically determined allometric relationships of Niklas and Spatz (2004).

Finally, we assume that competition is only significant for the lowest 'seedling' mass class. This enables us to represent gap dynamics among plants and resultant stages in succession. This represents a significant simplification compared to other approaches involving the Perfect Plasticity Assumption (PPA), as used within DGVMs such as LM3-PPA or CLM(ED) (Fisher et al., 2015; Weng et al., 2015), where canopies are assumed to perfectly fill gaps, equation (1.4), through photomorphism (Strigul et al., 2008). In LM3-PPA the radiative flux is limited by the available gap fraction in a given crown layer. PPA parallels our gap boundary condition at the lowest mass class, equation (3.11), but in RED the growth of a cohort is given by the disaggregation of total growth via metabolic scaling; equation (3.16).

These simplifications allow RED to be solved analytically for the steady-state vegetation cover given information on the mortality and growth rates per unit area for each PFT. Such analytical steady-state solutions mean that RED can be easily initialised in drift-free pre-industrial states, which is vital to avoid spurious sources and sinks in climate-carbon cycle projections. The analytical solutions also enable RED to be calibrated to the observed vegetation cover, via a single parameter (μ_0) which represents the ratio of mortality to growth for a tree of an arbitrary reference mass. The existence of analytical steady-state solutions for RED also opens up other promising research avenues. For example, these solutions imply relationships between the fractional coverage of each PFT, total plant biomass, and the ratio of mortality-to-growth. This in turn allows RED to be calibrated using observations of any two of these quantities. The analytical solutions also allow optimality hypotheses to be explored, for example the hypothesis that the fraction of net assimilate allocated to seed production maximises stand-density and/or

biomass (see chapter 5).

Aside from the existence of analytical steady-state solutions, RED is attractive for large-scale applications because it is both parameter sparse ('parsimonious') and requires very few driving variables. The main driving variable is the time-varying net plant growth rate for each PFT, which is defined as net primary production minus the local litterfall. These driving data can be provided by a land-surface scheme, as we do in this study, or from observations where appropriate (while the there does exists remotely sensed data on NPP, see section 5.6.3, there is a lack of local litter data). The only other driving variable for RED is the mortality rate, which we treat in this study as a geographically-varying PFT-specific constant that is independent of mass. However, in principle RED could utilise mortality rates that depend on plant mass and time to represent individual disturbance events (e.g. forest fires, disease outbreaks). Despite its simplicity, the RED model is able to fit the global distribution of vegetation types (Figure 3.5), and simulate successional dynamics, including changes in forest demography (Figure 3.10).

There are inevitably weaknesses with any particular modelling approach. For RED, a current limitation is for competition to lead to a single PFT at each location within each co-competing vegetation class (i.e. tree, shrub, grass). The PFT with the highest equilibrium fraction will end up excluding sub-dominant PFTs within the same vegetation class. It was necessary for us to account for this eventual competitive exclusion to derive zero-drift steady-states for the global runs presented in Section 3.3.2. Such competitive exclusion is a common problem in DGVMs (Fisher et al., 2018). Currently, RED would therefore not be the most appropriate DGVM to answer important questions regarding the role of biodiversity in ecosystem function (Pavlick et al., 2013; Levine et al., 2016). More sophisticated DGVMs are required to simulate plant diversity, such as individual-based models (Fischer et al., 2016), and DGVMs specifically-designed to capture sub-gridscale patch dynamics (Longo et al., 2019b,a). Adapting our 'gap' boundary condition, equation (3.12), appears to be a promising way to allow greater PFT diversity in RED, without unduly increasing model complexity. We see this as a key priority for future research.

RED is currently being coupled to the JULES Land Surface Model, replacing TRIFFID as the default DGVM within that framework. In parallel, significant improvements are being made to the representation of physiological processes in

JULES, most notably through the representation of non-structural carbohydrate ('SUGAR', Jones et al. (2020)), and through the inclusion of a coupled model of stomatal conductance and hydraulic failure under drought stress ('SOX', Eller et al. (2018, 2020)). Plans are also being made to derive the mortality rates for RED from the INFERNO forest-fire model (Burton et al., 2019). These developments will allow us to simulate the effects of size-dependent tree mortality rates within the near future.

3.5 Conclusion

In this chapter we have presented a new intermediate complexity second-generation dynamic global vegetation model (DGVM), which captures important changes in forest demography. The Robust Ecosystem Demography (RED) model makes a number of important simplifications to achieve this. These simplifications are based on theoretical concepts (e.g. metabolic scaling theory to estimate how plant growth rate varies with plant mass and minimum crown overlap) and also comparison to observed forest demography (Moore et al., 2018, 2020). As a result, RED is parameter sparse and can be driven with time series of net plant growth rate (and optionally disturbance rates) for each plant functional type (PFT). We have demonstrated that RED can be calibrated effectively to observed global vegetation maps, using a single fitting parameter (representing the ratio of mortality to growth for a plant of an arbitrary reference mass). In the future RED will be used in coupled climate–carbon cycle projections so to assess how changes in vegetation demography impact future CO2 and climate. We have made the prototype RED code publicly available, and we hope that Earth system and land-surface modellers will make good use of this framework to further their own research.

4 RED version 2: plant diversity, regrowth, and improved numerics

Rationale for Chapter

In this chapter we examine some of the issues present in RED version 1, and seek to address these in version 2. Firstly, the impact of the numerical discretisation of the mass classes. There is potentially a lot of numerical divergence present in version 1, with big differences between the continuous and discrete at equilibria (see appendix A for comparison). Secondly, there is significant dependence of regrowth time-scales on arbitrary parameters; the boundary mass, m_0, and the minimum vegetation fraction. Finally, there is a lack of intra PFT diversity (e.g. tree vs tree) diversity. For instances trees completely exclude trees otherwise the area occupied by vegetation is more than the grid-box, thereby breaking the hard exclusion approximation. This outcome has been an issues in other DGVMs that rely on Lotka-like competition, including TRIFFID and CTEM (Cox, 2001; Arora and Boer, 2006). For RED version 2, we want to address these issues while retaining the inherent simplicity of version 1. Later in this chapter, to demonstrate how RED can be used to examine the dynamics of secondary succession and the importance of size-demography in these outcomes, we simulate three forms of influences (land-use, fire and drought) in toy models and the resultant regrowth.

4.1 Improving mass class discretisation

There is numerical error in fixing the growth rate of population flux, $F_i = N_i g_i/(m_{i+1} - m_i)$, on the left boundary between m_i to m_{i+1}, as assumed in the original version of RED (Argles et al. (2020); Chapter 3 of this thesis). This arises as $g \propto m^{\phi_g}$, the growth rate increases non-linearly between the masses. By fixing g_i to the left

mass, we underestimate the number of trees entering into the next class. This error increases with wider mass widths. To account for this, version 2 adjusts the flux equation (3.10) with a growth rate, $g_{f,i}$, calculated between m_i and m_{i+1}. We explore the optimum position for the calculation of the fluxes, with the following initial schemes:

1. Left-boundary flux: $g_{f,i} = g_i$.
2. Right boundary flux: $g_{f,i} = g_{i+1}$.
3. Linear midpoint flux: $g_{f,i} = g_0(m_{f,i}/m_0)^{\phi_g}$, where $m_{f,i} = 1/2(m_i + m_{i+1})$.
4. Log midpoint flux: $g_{f,i} = g_0(m_{f,i}/m_0)^{\phi_g}$, where $m_{f,i} = \exp\{1/2\,(\ln\{m_i\} + \ln\{m_{i+1}\})\}$.

Given we have analytical solutions for the continuous (chapter 5) and discrete equilibrium (as outlined in section 3.2.5), we can test for the numerical error between each implementation (Figure 4.1). Ignoring the top classes, there is convergence among all schemes to the continuous number density as $I \to \infty$. All schemes of g_f typically underestimate the number density to the analytical solutions at low masses, while overestimating at higher masses. Placing g_f at the right boundary generates the most truncation error, while placing g_f at the left boundary minimise this error.

We can also compare how the choice of scheme affects the error relative to total coverage. Using the RED version 1 for a single PFT, and spinning up from a minimum vegetation fraction with a constant growth rate, we see that as we increase the number of mass classes, each flux scheme gets closer to the continuous equilibrium (Figure 4.2). In terms of dynamics the choice of $g_{f,i}$ causes a varied response of both the shape and time-scale for the ecosystem spin-up. By having $g_{f,i} = g_i$, RED version 1 significantly overestimates the spin-up time, especially given low mass classes (Figure 4.2.a). As $I \to \infty$, under this scheme there is slow convergence to the continuous equilibrium, with underestimation of the total coverage (Figure 4.2.d). There is the opposite result when using the right-hand scheme, which significantly underestimates the spin-up time and overestimates the final equilibrium coverage. The range between the left and right boundaries (light blue minus light yellow in figure 4.2.d) provide us with the extent of possible errors for the choice g_f. Both the linear midpoint (Figure 4.2.b) and

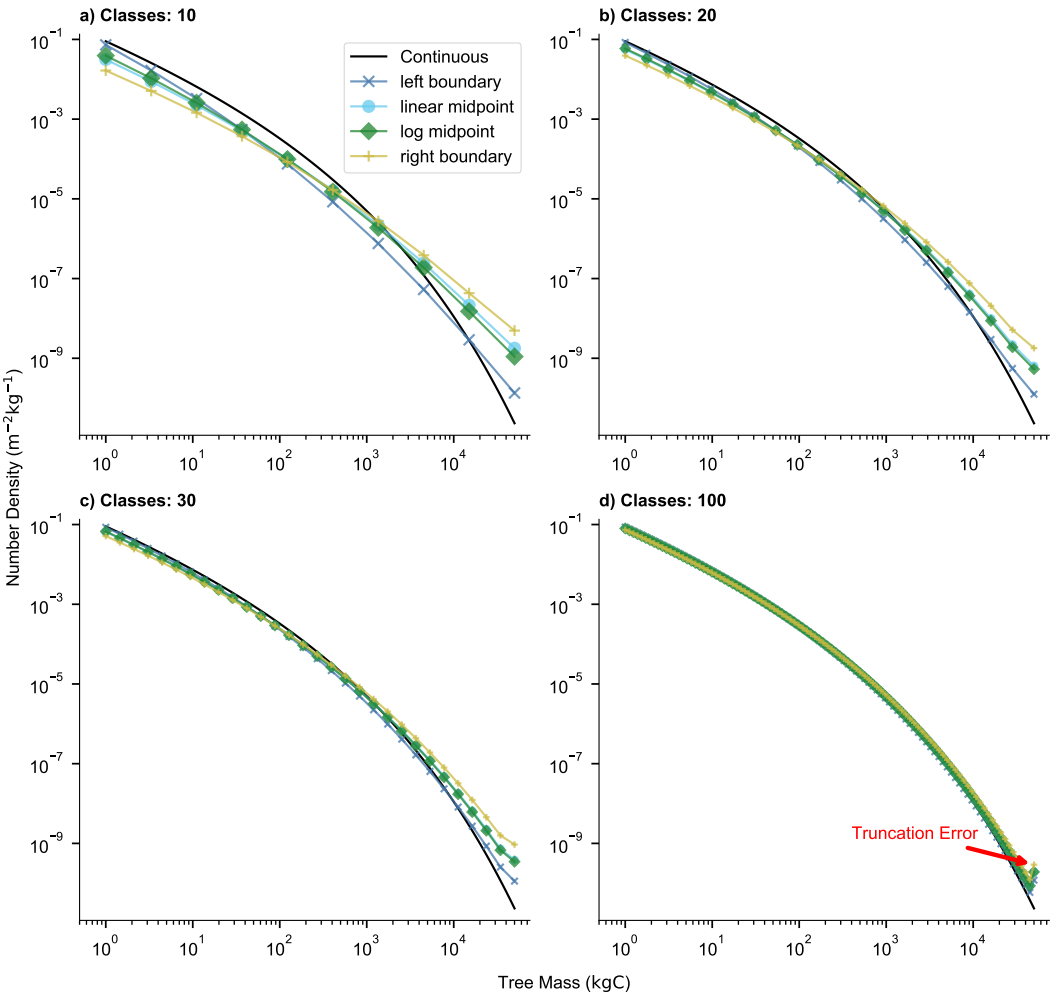

Figure 4.1: Comparing numerical flux schemes within RED to the continuous solution offered by CF-DET (Chapter 5) for 10 (panel a), 20, 30 and 100 mass classes over the same min ($m_0 = 1$ kgC) and max ($m_I = 50,000$kgC) mass range. RED vn1.0 (Argles et al., 2020) corresponds to a "left-boundary" flux calculation.

log midpoint (Figure 4.2.c) occupy a space part way between the left and right boundaries.

Because the contribution of the total carbon density is weighted to the larger trees (Figure 2.5) the total carbon density is particularly sensitive to the truncation error (Figure 4.1.d). Past a certain number of classes, the negative population flux error is outweighed by the error from truncating at m_I. To find the $g_{f,i}$ position that reasonably balances both the underestimation of the population flux and the truncation error, we can solve for a generalised linear weighting, $w \in [0, 1]$, between each masses:

$$g_{f,i} = g_0 \left(\frac{m_{f,i}}{m_0} \right)^{\phi_g}, \quad m_{f,i} = (1 - w)m_i + w m_{i,+1}. \tag{4.1}$$

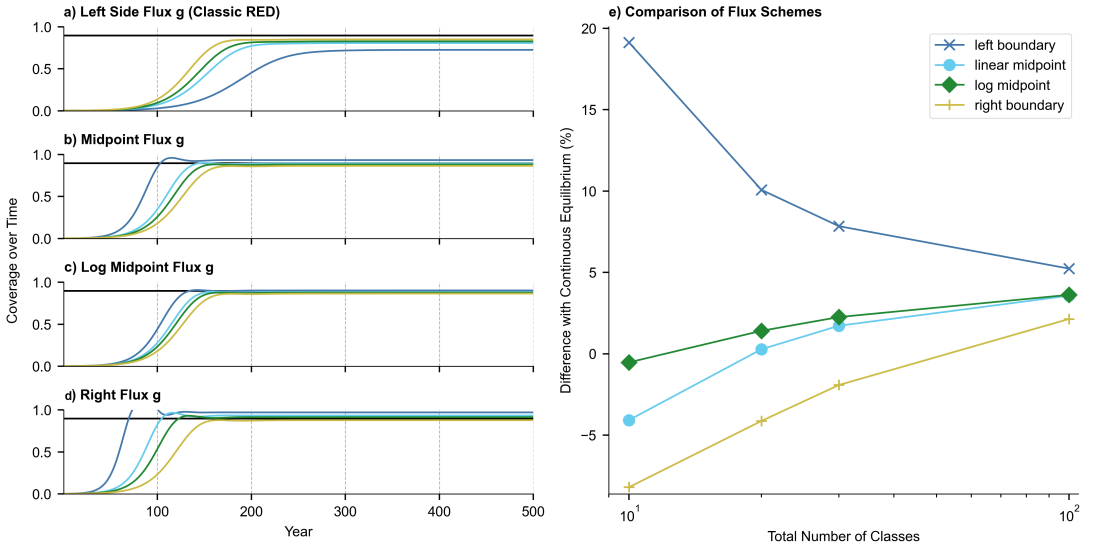

Figure 4.2: Dynamic simulations of RED with different discrete flux calculations compared with the continuous CF-DET solution for total coverage. For one PFT ($m_0 = 1\text{kgC}$ and $m_\text{I} = 50,000\ \text{kgC}, \alpha = 0.1, \mu_0 = 0.235$). Each panel of a-c shows dynamic simulations with increasing mass classes; dark blue: 10, light blue: 20, dark green: 30 and light green: 100. The black line indicates the analytical continuous solution for coverage. Panel (e) compares the difference between each scheme to the continuous equilibrium solution.

For the PFT parameters defined in figure 4.1, and using the continuous solution for the equilibrium (5.24), we get a carbon density of $M_\text{eq} = 25.7\ \text{kgC m}^{-2}$. By plotting the continuous and numerical carbon density against w and the number of mass classes, I, we are able to find the value of w that minimises continuous-discrete difference (Figure 4.3). Figure 4.3.b shows that increasing the number of classes to 30 will mitigate the numerical error. Increasing classes past 30 no longer contributes to a reduction in the difference. This is because the truncation of the number density at m_I in the discrete solution is semi-independent of the number of classes. However, this also means that the best w is also fixed past 30 classes at $w \approx 0.086$. Therefore, RED version 2 uses this value.

For simplicity, we still keep the sum of the growth $G = \sum N_i g_i$, with g_i being at m_i. To conserve carbon, we add the extra growth $N_i(g_{f,i} - g_i)$ to the demographic litter. In addition, The discrete equilibrium solution changes from equation (3.20), as the population flux, F is now dependent on $g_{f,i}$:

$$\lambda_i = \frac{\frac{g_{f,i-1}}{m_i - m_{i-1}}}{\frac{g_{f,i}}{m_{i+1} - m_i} + \gamma}. \tag{4.2}$$

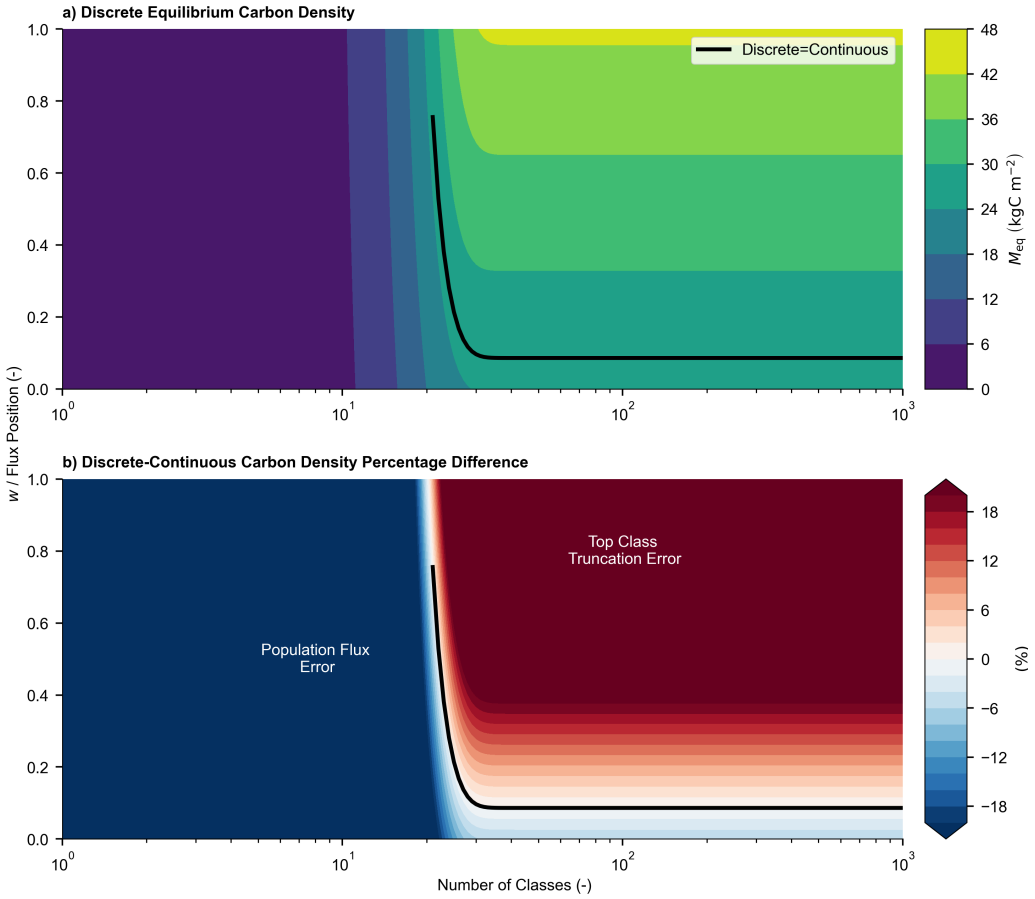

Figure 4.3: Panel (a) shows the discrete equilibrium carbon density, along with the line where the discrete is equal to the continuous solution (black line). Panel (b) shows the percentage difference between the continuous and discrete equilibrium carbon density, against the number of classes and the $g_{f,i}$ position. $w = 0$ corresponds to $g_{f,i} = g_i$, while a $w = 1$ gives $g_{f,i} = g_{i+1}$.

4.2 Regrowth sensitivity to parameters

To investigate the relationships between parameters and regrowth time for RED version 1, we set up a test where one PFT regrows from a minimum vegetation fraction, $\nu_{\min}$. Given the equilibrium solutions of RED it is possible to fix the equilibrium at M_{eq}.

We perform a parameter sensitivity analysis, where each ensemble member was selected from distributions that provide a plausible range of realistic parameter values (Figure 4.4). For α, γ and $a_{1\text{kgC}}$ we use a truncated normal distribution. $a_{1\text{kgC}}$ is a reference crown area which can be rearanged for a_0 using equation (3.3). For the boundary mass, m_0, we pick a uniform distribution between 0.2 kgC and 1.2 kgC. We then iterate for the equilibrium carbon density, using equations

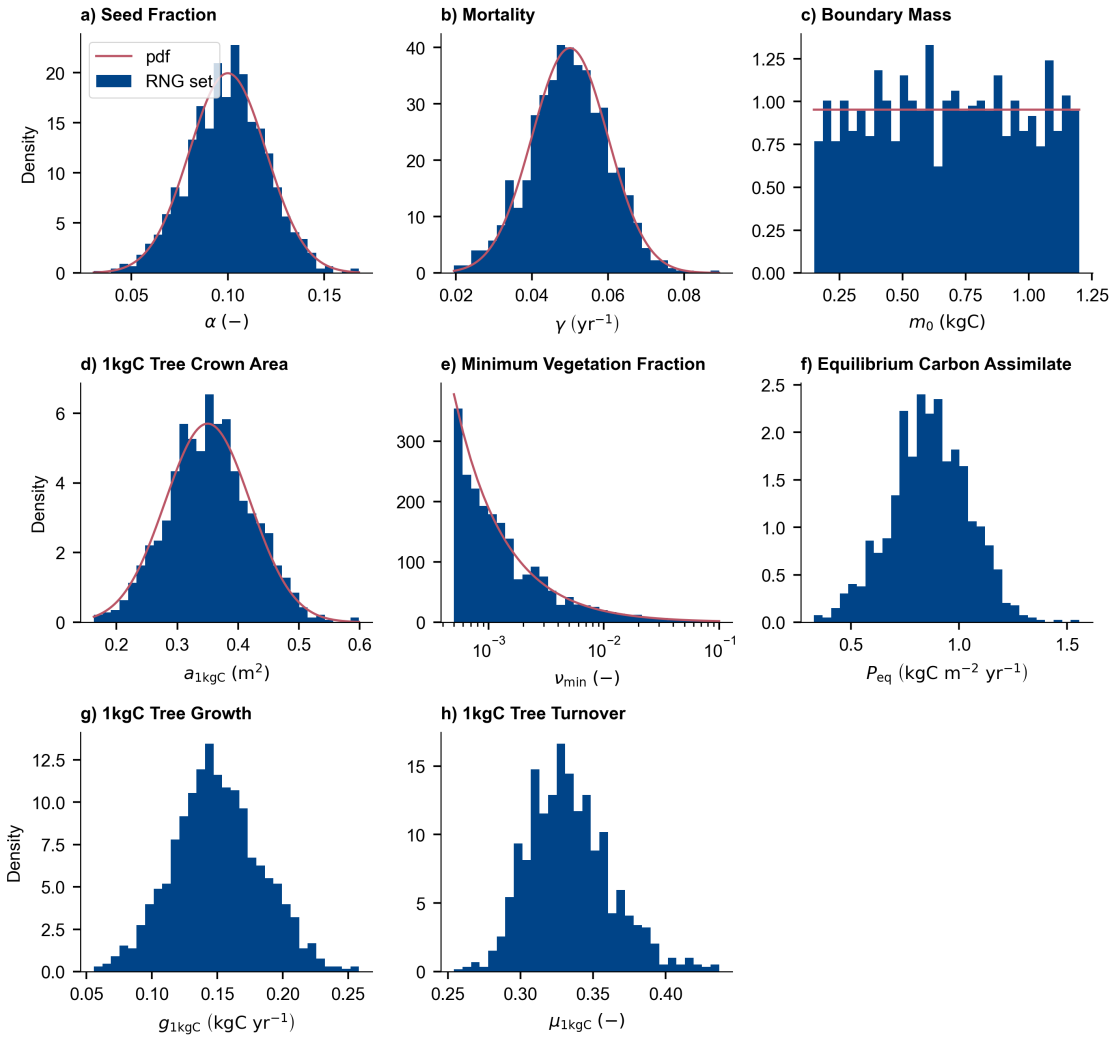

Figure 4.4: RED version 1 parameter distribution for investigating regrowth times. Parameters (a) α, (b) γ, (c) m_0, (d) $a_{1\mathrm{kgC}}$, and (e) $\nu_{\min}$ are picked from an assumed Probability Distribution Function (red line). PDFs are roughly chosen to be around the default values from RED version 1 (Arora et al., 2020). Most parameter PDFs are truncated normal distributions, with the exception of boundary mass which is uniform. (f) P_{eq}, (g) $g_{1\mathrm{kgC}}$ and $\mu_{1\mathrm{kgC}}$ are estimated from the resultant equilibrium solution for M_{eq}.

(3.29) & (3.33), for a value of $M_{\mathrm{eq}} = 15\ \mathrm{kgC\ m^{-2}}$ to find the value of μ_0 which satisfies the solution:

$$M_{\mathrm{eq}} = 15\ \mathrm{kgC\ m^{-2}} = \frac{m_0 X_M}{a_0 X_\nu}\left[1 - \left(\frac{1-\alpha}{\alpha}\right)\mu_0 \frac{X_N}{X_G}\right]. \tag{4.3}$$

Given the simulation is using a single PFT, equation (4.3) can be iterated to find a solution for μ_0. Through the definition of μ_0 we invert for the required value of g_0 and equilibrium carbon assimilate (Figures 4.4.h and 4.4.f).

Using the combination of both g_0 and γ, RED is driven from the minimum vegetation fraction (Figure 4.5). For some values there is breaking of the numerical

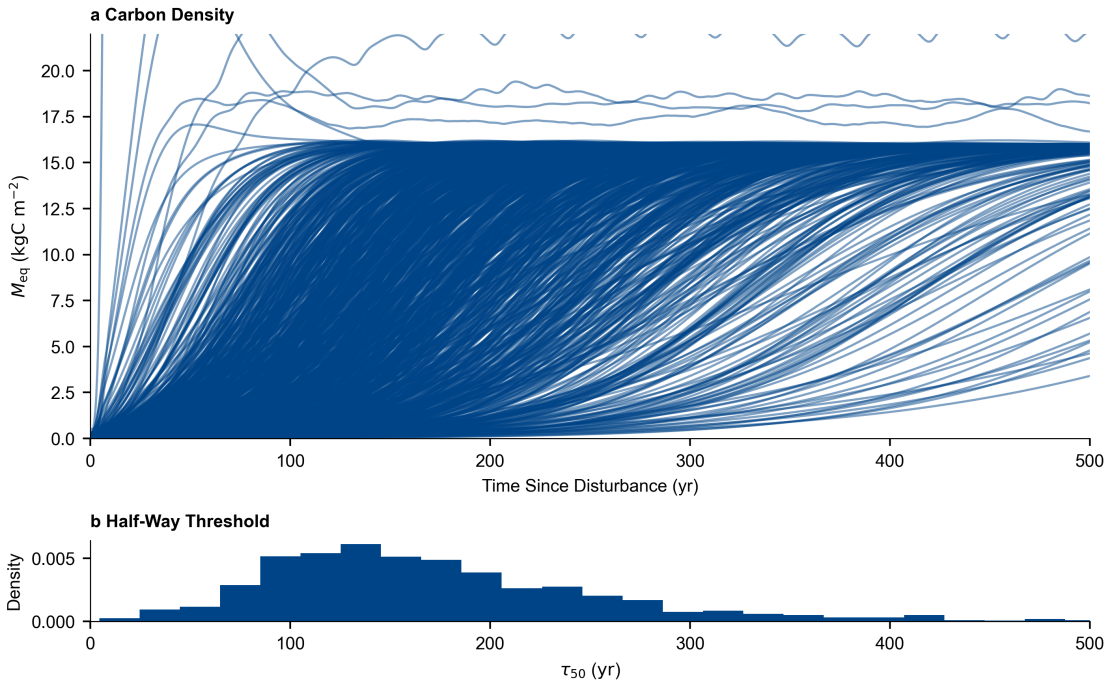

Figure 4.5: Ensemble simulations of a single PFT spun up to a equilibrium carbon density of $15\ \mathrm{kgC\ m^{-2}}$, with each simulation having random PFT parameters. Panel (a) the ecosystem carbon density over time for each ensemble member. Panel (b) shows the distribution of the intercept times, when the carbon density is over half-way to the equilibrium value.

stability Courant–Friedrichs–Lewy condition, resulting in overshooting. The plant growth, in a given time-step, is greater than the width of the binning of the masses; $g \geq \Delta m/\Delta t$, this outcome has previously been outlined in Moore (2016).

To get a measure of regrowth senstivity, we record the time, τ_{50}, to get to 50% of the equilibrium value ($15\mathrm{kgC\ m^{-2}}$). This is approximately at the inflexion point of the regrowth logistic curve. For the majority of runs the threshold of τ_{50} is met within $300\ \mathrm{yr}$ (Figure 4.5.b). When compared with observations, this is potentially an unrealistic regrowth time-scale for secondary-succession (Heinrich et al., 2021). However, we are assuming distributions of initial vegetation fractions that are small; down past $\nu_{\min} < 0.001$, in reality plants may not wholly be removed after a disturbance.

We can plot how τ_{50} varies with each PFT parameter for the same equilibrium carbon density (Figure 4.6). Certain parameters have a significant impact on the regrowth time-scales. For instance, by having larger mortality a PFT must compensate by having a larger growth rate to reach the same equilibrium point. Through equation (3.11), this means more assimilate is being used for recruit-

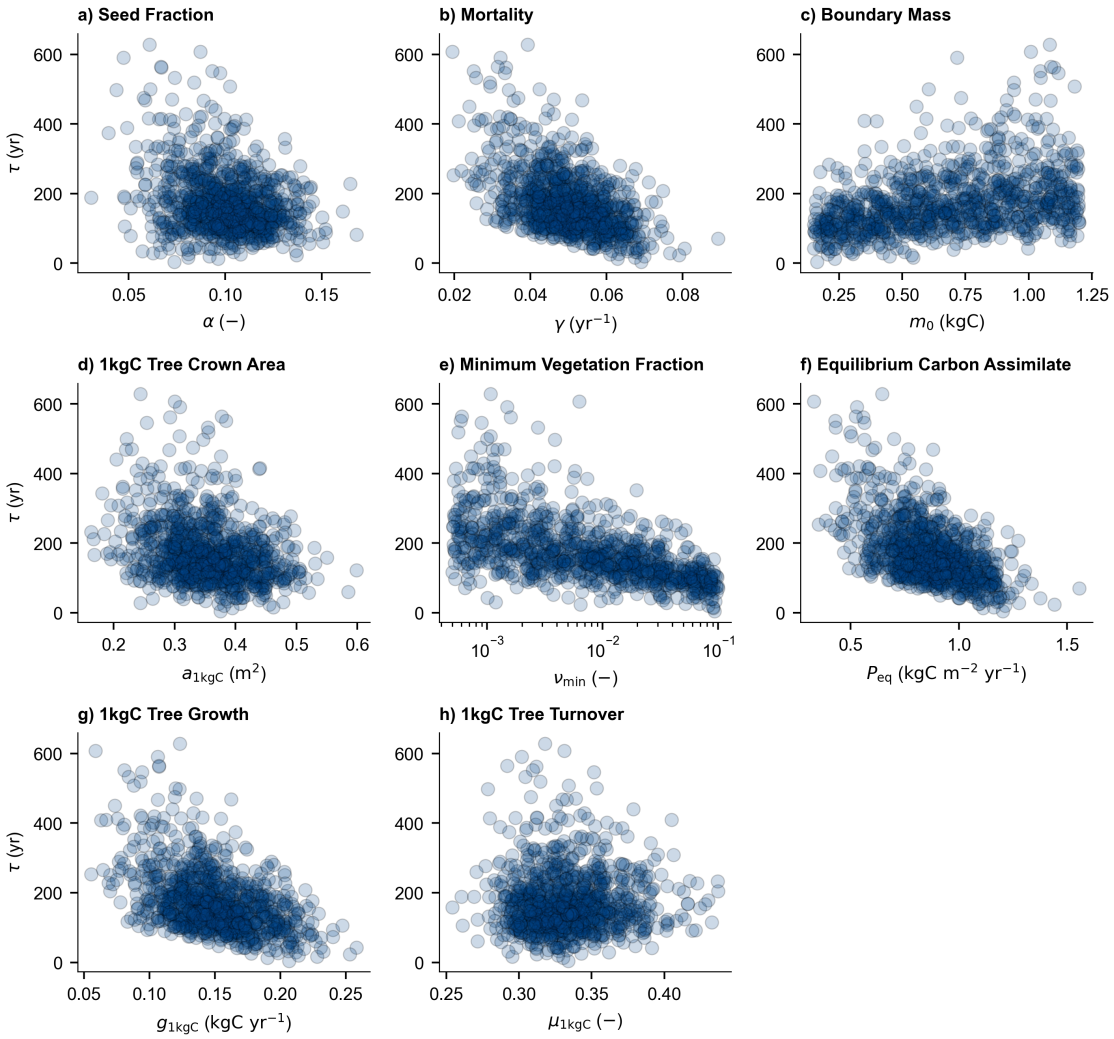

Figure 4.6: Sensitivity of each PFT parameter to the threshold time, τ_{50}, where the ecosystem carbon density is half-way to equilibrium.

ment, decreasing regrowth times significantly. There is a constrained range for regrowth times for low mortality rates, with τ_{50} being at least $150\ \mathrm{yr}$ for $\gamma < 0.04\ \mathrm{yr}^{-1}$ (Figure 4.6.b).

Another important factor in regrowth times is the initial vegetation fraction (Figure 4.6.e). Given the values picked for $\nu_{\min}$ is over log-space and close to zero, the mean regrowth time from $\nu_{\min} = 0.1$ versus $\nu_{\min} = 0.01$ varies significantly; $\tau_{50} \approx 120\ \mathrm{yr}$ versus $\tau_{50} \approx 200\mathrm{yr}$, respectfully. Like mortality, having a greater initial vegetation cover also constrains regrowth times. The final sensitive parameter is the boundary mass, m_0. Having a lower boundary mass will decrease regrowth time, because the number of recruits is proportional to $\alpha P/m_0$. τ_{50} has significantly less sensitivity with other variables like α, $a_{1\mathrm{kgC}}$, and $\mu_{1\mathrm{kgC}}$.

4.2.1 Explicit Seed Class

A key model issue with RED version 1 is how to define the boundary m_0. RED version 1 model uses the mass $1\mathrm{kgC}$ for trees, without significant justification. The value of which is sensitive for regrowth time-scales. A large m_0 will add multiple decades on reaching equilibrium (Figure 4.6). For this reason we choose to include a seed pool density, N_s, before applying competition. This also allows the the model to robustly define a tangible lower-bound to the plant size-structure, and expand the scope by including explicit seed related processes. In the most simplest form, we follow the assumption of seed/tree turnover equivalence; that the rate of germination, $g_s = g_0$ and $\gamma = \gamma_s$, is such that $\gamma_s m_s / g_s = \mu_0$. The continuous derivation for this assumption is presented through CF-DET, in chapter 5.3. The seeds are spread by:

$$F_s = \frac{\alpha P}{m_s}, \tag{4.4}$$

the ratio of assimilate devoted to reproduction, αP, and the seed mass, m_w. Where $m_s = m_0$ and F_s is the flux entering into the seed pool. Seeds germinate into plants under a new competitive constraint:

$$F_0 = \frac{N_s g_s}{m_0} s. \tag{4.5}$$

s is equivalent to the shading term defined in equation (3.12). The discrete dynamics of the seed pool, N_s is defined in a similar way as equation (3.17):

$$N_s^{(j+1)} = N_s^{(j)} + \Delta t \left(F_s^{(j)} - F_0^{(j)} - \gamma_s^{(j)} N_s^{(j)} \right), \tag{4.6}$$

where γ_s is the seed mortality. In RED version 2 the seed pool does not contribute towards the total coverage, and therefore competition. The total seed mass density is added t the total carbon density:

$$M = N_s m_s + \sum_{i=0} N_i m_i. \tag{4.7}$$

g_s does not contribute to total growth as there is no gain in mass; seeds are germinating into plants of the same mass. RED version 1 spins up from $\nu_{\min}$, the value of which can have a significant impact on regrowth time (Figure 4.6.e). The

value of $\nu_{\min}$ also affects the competition fluxes. To remove the reliance on $\nu_{\min}$, we choose to instead use a minimum seed density, $N_{s,\min}$, $N_{s,\min}$ and g_s establish a minimum flux into the population, which can potentially be related to the time-scales of forest migration. Migration of forests is normally a relatively slow process. Svenning and Skov (2007) suggests rates of between $25 - 2500\mathrm{m\ yr}^{-1}$ for post-glacial tree migration in Europe after the Pleistocene epoch, representing a very slow processes for ESMs scales (Figure 1.2).

4.2.2 Seed Pool Steady state

We must adjust our equilibrium to account for the new seed pool. The equilibrium seed density is given as $N_{s,\mathrm{eq}}$, and is equivalent to equation (5.12):

$$\gamma N_{\mathrm{eq}} = \frac{N_{s,\mathrm{eq}} g_0}{m_0} s, \tag{4.8}$$

which simplifies under our seed/plant turnover assumptions to:

$$N_{s,\mathrm{eq}} = \frac{\mu_0 N_{\mathrm{eq}}}{s}. \tag{4.9}$$

The flux entering into the seed pool is equivalent to the number of seeds leaving, equation (5.11), therefore we get:

$$\left(\frac{\alpha}{1-\alpha}\right) \frac{g_0}{m_s} N_{\mathrm{eq}} X_G = N_{s,\mathrm{eq}} \left(\gamma_s + g_s\right). \tag{4.10}$$

Substituting in equations (4.10) and (3.24), we end up with the equivalent equilibrium solution for the coverage:

$$\nu_{\mathrm{eq},k} = 1 - \left(\frac{1-\alpha}{\alpha}\right) \left(1 + \mu_0\right) \mu_0 \frac{X_N}{X_G} - \sum_{l \neq k} c_{kl} \nu_l, \tag{4.11}$$

to CF-DET equation (5.17). A key outcome is that we still retain the simplicity of the RED version 1 steady solutions, but with the added feature of explicitly representing seeds (see chapter 5).

4.3 Implementing Diversity

As outlined in section 1.2.2, there are issues with DGVMs that rely on the hard-exclusion principle and the representation of intra-PFT diversity (Arora and Boer, 2006; Scheiter et al., 2013). In RED version 1, the assumption of $c = 1$ for PFTs within the same group does not account for observations where tree PFTs exists within the same grid-box (Figure 3.5). Thus RED version 1 underestimates diversity of species observed at large scale.

For example, let us assume two tree PFTs, A and B, have respective equilibrium vegetation fractions; ν_A and ν_B, along with a shared competition coefficient $c = c_{A,B} = c_{B,A}$. In RED, we know that in order to sustain a population the vegetation fraction must be below equation (3.32), otherwise the number of deaths will be greater than number of new recruits. This means that for $\alpha_A = \alpha_B$, if $\mu_{0,A} < \mu_{0,B}$, then at equilibrium; $\nu_A \to 1-(1-\alpha)\mu_0/(\alpha\mathcal{F}_g)$ and $\nu_B \to 0$ (Figure 4.7, $c = 1$). In the dynamic model, the grid-box will always have a tree monoculture (Figure 4.11.a). For co-existence $\mu_{0,A}$ must equal $\mu_{0,B}$, which is not a realistic outcome as mortality and growth vary between species.

Lotka models can get around this by assuming that $c < 1$ (Arora and Boer, 2006). This enables co-existence, allowing for some overlap between vegetation fractions. However, in certain instances this breaks the hard-exclusion approximation, equation (1.1); the total PFT area, $\nu_A + \nu_B$ is greater than the grid-box area (Figure 4.7, $c = 0$ and $c = 0.5$).

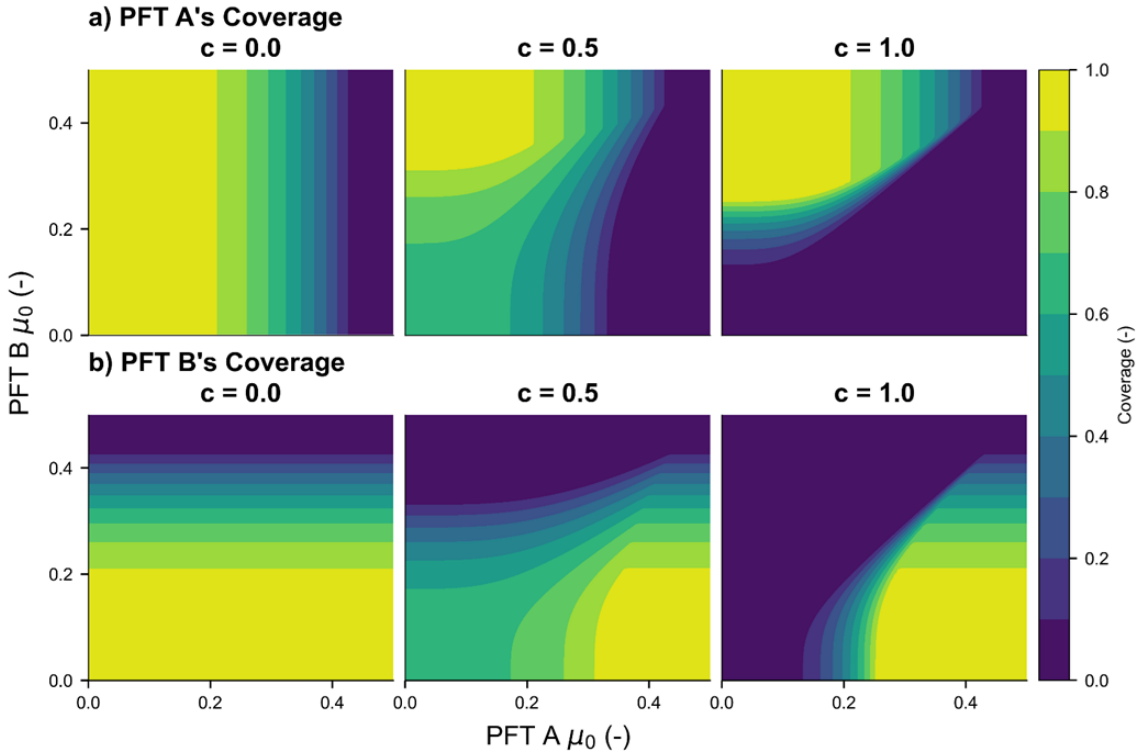

Figure 4.7: How the equilibrium coverage for the two example PFTs, A (panel a) and B (panel b) vary with μ_0 and the competition coefficient, c (with $c = c_{\mathrm{A,B}} = c_{\mathrm{B,A}}$.

To account for this breaking of the hard-exclusion rule, we must remove the assumption that total canopy area is consistent with the total area occupied. In reality trees overlap. Therefore, the space occupied is redefined as the total "projected top down" area of the vegetation canopy, $\sum_i \nu_{\mathrm{TD},i}$. $\sum_i \nu_{\mathrm{TD},i}$ should not exceed the grid-box area:

$$\nu_{\mathrm{bare}} + \sum \nu_{\mathrm{TD},i} = 1, \tag{4.12}$$

where ν_{bare} is the fraction of bare soil.

For simplicity, let us assume that all PFTs of the same group posses the same c value for competing with each other and more dominant PFT groups (Table 4.1). We can estimate the total top-down space as:

$$\nu_{\mathrm{TD},i} = c\nu_i. \tag{4.13}$$

Table 4.1: Competition coefficients assumed for different plant functional groups under RED version 2.

		l		
c_{kl}		Trees	Shrubs	Grasses
	Trees	1	0	0
k	Shrubs	c	1	0
	Grasses	c	c	1

$(1-c)\nu$ is the degree the fractions overlap. This allows RED version 2 to simulate diversity and and still have effective vegetation fractions that do not exceed unity. The assumption of c being a shared constant avoids the additional mathematical complexity of accounting for different inter-PFT overlap tolerances. In the earlier example, if $c_{A,B} \neq c_{A,C}$, then estimating $\nu_{\mathrm{TD},i}$ is significantly harder.

4.3.1 Estimating the diversity of an Ecosystem

Let us define a diversity indices, H_c. H_c is the Shannon Diversity Index but accounting for the "niche overlap" of the system. H_c can be estimated from any shared PFT ecosystem property, Z_i, and ecosystem total Z_{tot}, as:

$$H_c = -c\sum_i \left(\frac{Z_i}{Z_{\mathrm{tot}}}\right)\ln\left\{\frac{Z_i}{Z_{\mathrm{tot}}}\right\}, \quad Z_{\mathrm{tot}} = \sum_i Z_i. \tag{4.14}$$

H_c is the degree quantity Z is not occupying the same fractional area. A recent concept in ecology, is that ecosystems adhere to the principle of maximum entropy (Harte, 2011), or Maximum Entropy Theory of Ecology (METE). METE is that given a set of resource constraints (such as energy or space), a system will occupy a state that maximises the entropy or species diversity/abundance. This is because the maximum likelihood of seeing such a macroscopic state is one which corresponds to the maximum number of microscopic states. A study by Xiao et al. (2015), found that the METE explained the vast majority of species abundance across 60 globally distributed natural forests.

To mimic the outcome of METE, RED version 2 assumes that the shared c, is one which maximises equation (4.14), with respect to the coverage ($Z_i \to \nu_i$) (Figure 4.8).

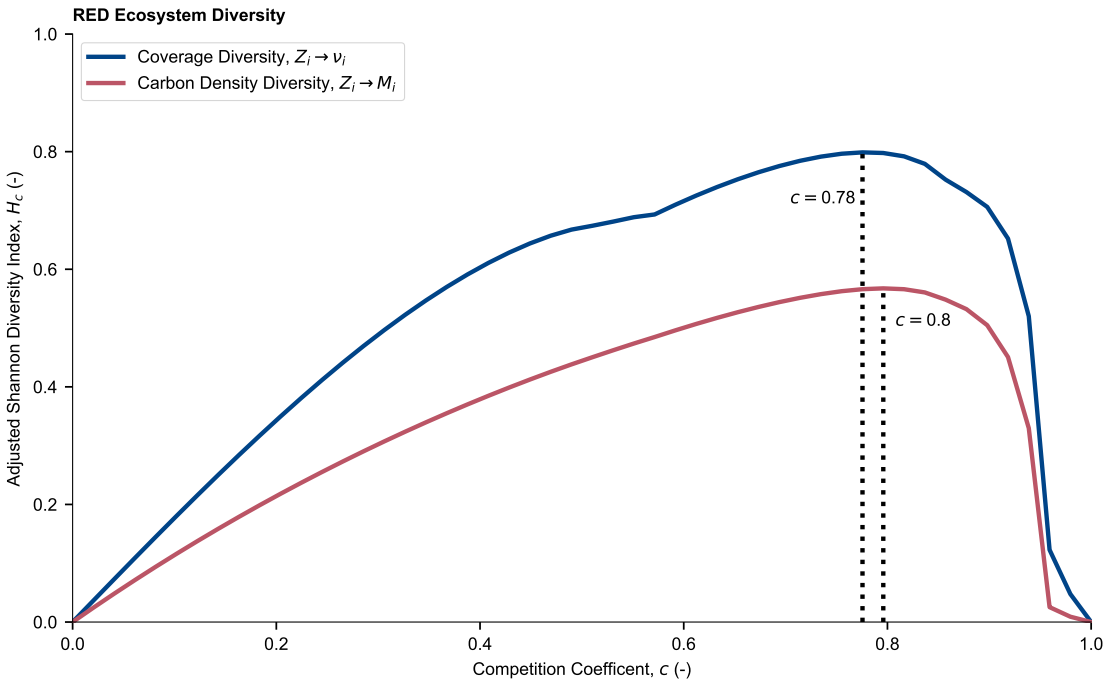

Figure 4.8: The modified Shannon diversity index, H_c, of ecosystem equilibrium coverage (red line) and carbon density (blue line) versus the shared competition coefficient for RED version 2. The six PFTs are chosen from table 4.2. Respective maximums are shown by the dotted black lines.

4.4 Comparing RED version 1 to 2

Here we compare the improvements of RED version 1 and 2. For this we select six PFTs whose parameters are chosen to represent a range of traits (Table 4.2). The PFTs are divided into representing the group hierarchy; grasses, shrubs and trees. Each group has two PFTs that shade each other and sub-dominant groups (Table 4.3). For RED version 1, the competition coefficient is $c = 1$. While for RED version 2, we select a coefficient of $c = 0.78$, this is to maximise the ecosystem diversity per unit area (Figure 4.8). Instead of selecting a optimum binning for a given m_0, for simplicity we choose a maximum mass; m_I.

Table 4.2: Selected PFTs with parameter values for comparing some of the advancements of RED version 2 with version 1. PFTs are classified by a spectrum of turnover values to capture grass, shrub and tree characteristics.

PFT	Classes	m_0 (kgC)	m_I (kgC)	$a_{1\mathrm{kgC}}$ (m^2)	h (m)	α ($-$)	$\mu_{1\mathrm{kgC}}$ ($-$)	γ_b (yr^{-1})	$g_{1\mathrm{kgC}}$ ($\mathrm{kgC\ yr}^{-1}$)
Grass-A	10	0.01	100	1	1	0.1	0.5	0.15	0.3
Grass-B	10	0.01	100	1	1	0.1	0.45	0.09	0.2
Shrub-A	20	0.015	5×10^3	1	1.5	0.05	0.35	0.05	0.143
Shrub-B	20	0.015	5×10^3	1	1.5	0.05	0.3	0.04	0.133
Tree-A	30	0.02	5×10^5	1	2	0.01	0.25	0.025	0.1
Tree-B	30	0.02	5×10^5	1	2	0.01	0.2	0.02	0.075

Table 4.3: Competition coefficients used in comparison of RED version 1 and 2. PFTs at the same successional stage (e.g. Early, Mid, and Late) compete with each other. For RED version 1 $c = 1$, else for version 2 $c = 0.78$.

c_{kl}		l					
		Grass-A	Grass-B	Shrub-A	Shrub-B	Tree-A	Tree-B
k	Grass-A	1	c	c	c	c	c
	Grass-B	c	1	c	c	c	c
	Shrub-A	0	0	1	c	c	c
	Shrub-B	0	0	c	1	c	c
	Shrub-A	0	0	0	0	1	c
	Shrub-B	0	0	0	0	c	1

RED version 1 and 2 were respectively initialised using a minimum vegetation fraction and minimum seed density. To make comparison fairer, these two boundary conditions are assigned the same value. For RED version 1 the number density in the first class is; $N_0^{(0)} = \nu_{\min}/a_0$. For RED version 2; $N_s^{(0)} = \nu_{\min}/a_0$. To be consistent with Argles et al. (2020), we choose a minimum vegetation fraction of $\nu_{\min} = 1 \times 10^{-3}$.

4.4.1 Single PFT

To investigate the impact of the new numerical scheme and seed pool, we simulated all PFTs individually. We run RED version 1 and version 2 from spin-up for each PFT in table 4.2 (Figure 4.9). RED version 2 results in faster regrowth times for trees, and to a lesser extent shrubs and grasses. For PFTs with a large number of mass classes, RED version 2 is more consistent with the continuous equilibrium solutions. This is expected as low class PFTs typically underestimate the carbon density (figure 4.3).

We also compare how each new modification influences the regrowth dynamic (Figure 4.10). To do this we run RED version 2, but with the previous flux scheme: with $g_{f,i} = g_{f,0}$. We also run RED version 1 with the new flux scheme: $g_{f,i} = wg_{f,0}, \quad w = 0.09$. While both changes reduce regrowth time, the addition of the seed pool contributes the most. The new flux scheme increases the equilibrium carbon density. The overall impact is a faster and steeper regrowth curve.

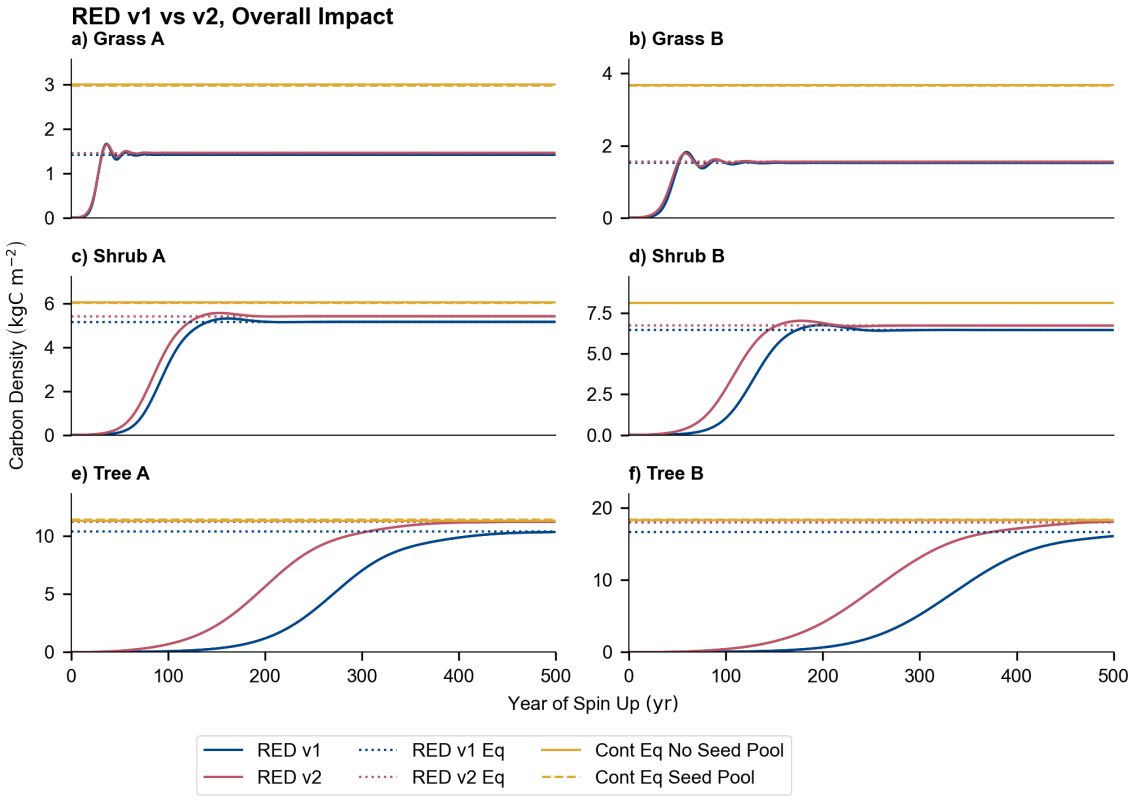

Figure 4.9: RED version 1 and 2 spin-up comparison of individual PFTs carbon density. PFTs listed in table 4.2. Blue and red lines are the spin up simulations of RED version 1 and version 2 respectively. Blue and red dotted lines show respective version 1 and 2 equilibrium. While yellow lines show the continuous solutions for the carbon density from CF-DET (Chapter 5).

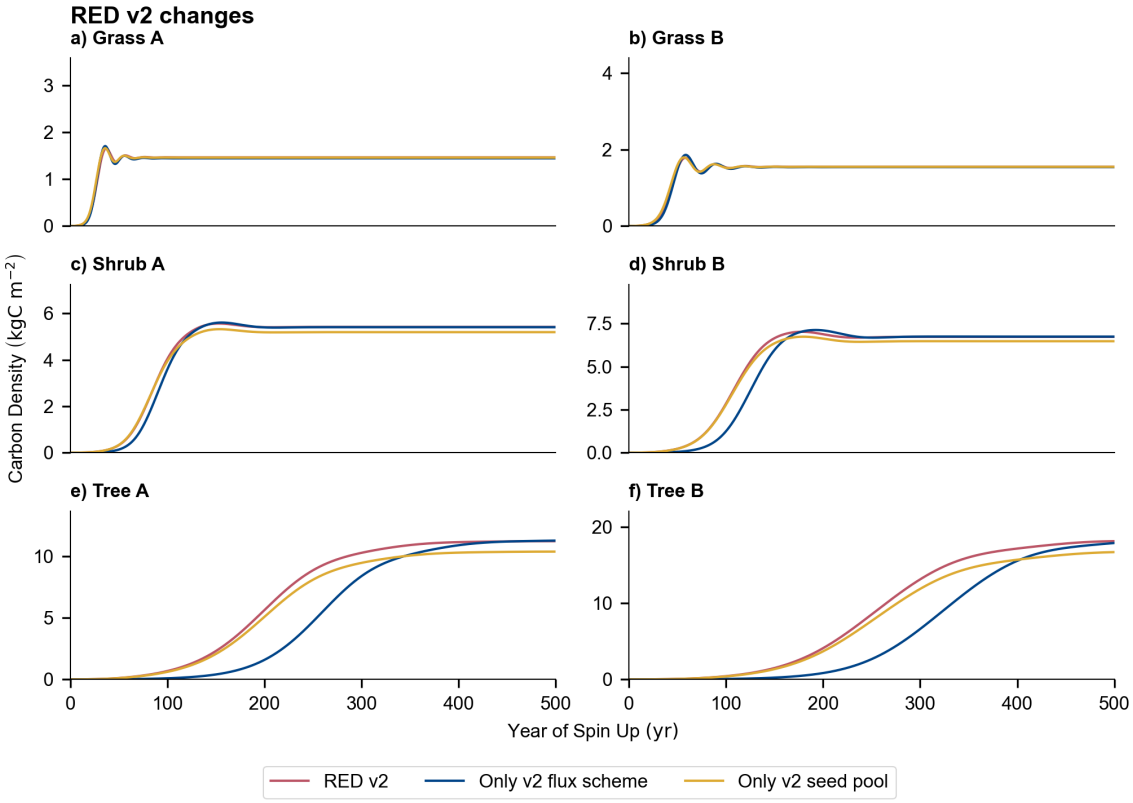

Figure 4.10: Contribution of each RED version 2 change to the spin-up simulations of carbon density for each individual PFT defined in table 4.2. Blue line is a simulation using the new g_f flux scheme, with no seed pool. Yellow line is a simulation using a seed pool, but without the flux scheme. Red line is the combined impact of both changes in RED v2.

4.4.2 Many PFTs

To compare the changes to diversity, we now include all the PFTs together for the spin-up simulation. From the parameter values present in table 4.2, we are able to solve for the equilibrium solution by estimating the coverage from the respective $\mu_0 = \mu_{1\text{kgC}} m_0^{1-\phi_g}$ and equation (4.11). In addition, we perform a test where RED version 2 starts with the equilibrium seed density, $N_s^{(0)} = N_{s,\text{eq}}$; equation (4.10). This is to simulate a hypothetical scenario of regrowth where a disturbance has removed all the plants, but not the seeds. This is to illustrate how the addition of the seed pool improves the representation of secondary-succession.

Figure 4.11 shows the simulation results across a $800\ \text{yr}$ period. RED version 1 has complete competitive exclusion of all PFTs expect Tree B in the equilibrium, and takes significantly longer period to reach this point. In contrast, having $c = 0.78$ decreases the time-scale of regrowth and allows for diversity of PFTs at the equilibrium (Figure 4.11.b). With the new seed class, we can now more ap-

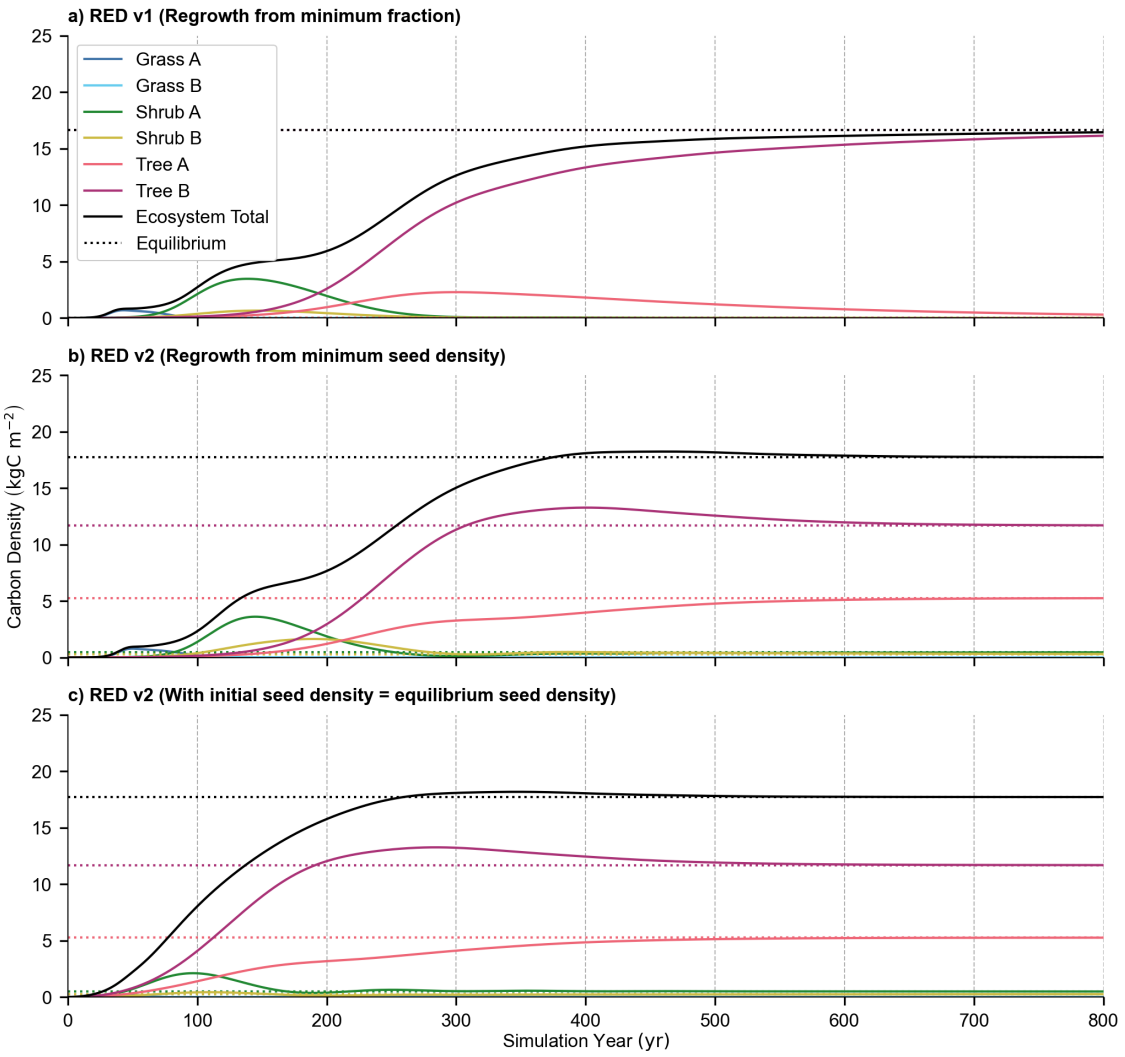

Figure 4.11: Successional comparision between RED version 1 and version 2 for PFTs listed in table 4.2. Carbon density is plotted against simulation year. Panel (a) shows the spin-up of RED version 1 from a minimum fraction. Panel (b), RED version 2 is driven from a minimum seed density. Panel (c), RED version 2 regrowth, where the initial seed flux is equal to the equilibrium seed flux.

propriately represent secondary succession and have much faster regrowth times (Figure 4.11.b). By setting the initial seed density to the equilibrium, we can approximately half the time taken to pass the τ_{50} threshold for the total ecosystem carbon density ($M_{\text{tot}} \approx 8.5\ \text{kgC m}^{-2}$ at $\sim 100\ \text{yr}$) over spinning up from a minimum boundary ($M_{\text{tot}} \approx 8.5\ \text{kgC m}^{-2}$ at $\sim 200\ \text{yr}$). This can be further reduced if the disturbance event is not absolute in the removal of all the trees, as we will explore in the next section.

4.5 Implementations of Land-use, Land-use change, and Disturbances

DGVMs have relied on a variety of relationships to capture drought or fire (Chapter 1). These processes vary from area-based rates of disturbance, oriented around the concept of patches (Moorcroft et al., 2001; Medvigy et al., 2009), to parameterisation of large-scale disturbances such as fire for individual based DGVMs (Smith, 2001; Thonicke et al., 2001). Perhaps the simplest implementation of area-based disturbance is within average-area models, such as fire in JULES-INFERNO (Burton et al., 2019). In reality, the impact of drought and fire on vegetation is heavily dependent on demography (Gora and Esquivel-Muelbert, 2021). Another exogenous interaction is land-use change. In exclusionary models land-use change can be implemented as an additional tile-type or PFT that is given priority for space (Haverd et al., 2018; Littleton et al., 2020).

With RED we want to build a model framework that is capable of capturing both area-based and size-dependent mortality processes. In the next sections we examine three examples of how to represent both processes.

4.5.1 Area-based disturbance and Land-Use Change

For even-area based disturbance we can simply apply a shared γ across all PFTs and sizes:

$$\frac{\partial \nu_{\rm d}}{\partial t} = \gamma_d \sum_i \nu_{{\rm TD},i}. \tag{4.15}$$

Where γ_d is the disturbance rate. We can rearrange equation for the necessary γ_d and then add on to the baseline mortality rate, $\gamma_{\rm b}$. In the case of the discrete model:

$$\gamma_d = \frac{1}{\sum_i \nu_{{\rm TD},i}} \frac{\Delta \nu_{\rm d}}{\Delta t}, \tag{4.16}$$

Where $\Delta \nu_{\rm d}$ is removed within the given time-step, Δt. For land-use and land-use change, RED could excluded a fraction of the grid-box from vegetation by implementing a crop/pasture PFT at the top of the hierarchy. This effectively stops natural PFT seeds from spreading into a proportion of the grid-box. Let us assume a Land-Use fraction; $\nu_{\rm LU}$, with compeitition coefficient for natural PFTs being $c_{i,{\rm LU}} = 1$. The dynamics of $\nu_{\rm LU}$ can be proscribed, like in the CMIP runs

(Lurton et al., 2020), or modelled separately through an independent crop model before RED is driven. For instance, we could numerically implement a proscribed mortality associated with γ_{LUC}:

$$\gamma_{\mathrm{LUC}} = \frac{1}{\sum_i \nu_{\mathrm{TD},i}} \frac{\Delta \nu_{\mathrm{LU}}}{\Delta t}. \tag{4.17}$$

γ_{LUC} is the required mortality to be consistent with the clearance for the land use, $\Delta \nu_{\mathrm{LU}}$.

4.5.2 Water-stress mortality

The increased frequency and severity of drought is likely to have important implications for both regional ecosystem resilience and the carbon cycle (Allen et al., 2010; Williams et al., 2013; Gora and Esquivel-Muelbert, 2021). The interaction of droughts at an ecosystem level is complex, both growth rates (Metcalfe et al., 2010; Jones et al., 2020) and mortality of trees are affected. The cause of water-stress mortality is widely discussed, ranging from tree carbon starvation (McDowell et al., 2011) through to hydrolic embolism of the plant xylem (Rowland et al., 2015). Despite this, it is widely understood from observations (Nepstad et al., 2007; da Costa et al., 2010) and theory (Gora and Esquivel-Muelbert, 2021), that water-stress mortality increases with plant size. The mortality function with respect to size could be significantly more varied, with it also increasing with respect to smaller trees in certain situations (Fauset et al., 2012; Zuleta et al., 2017; Gora and Esquivel-Muelbert, 2021).

Height is a key factor when considering tree risk to water-stress (Stovall et al., 2019). In this context, we explore a hypothetical example of a mortality function with respect to tree height, h. h is assumed to be related to the plant mass through the allometric equation (2.22). Let us assume a power-law relationship of water-stress mortality, γ_{ws} with respect to height by the equation:

$$\gamma_{\mathrm{ws}} = \gamma_{\mathrm{ws},0} \left(\frac{h}{h_0} \right)^{\phi_{\mathrm{ws}}}. \tag{4.18}$$

For the modelled PFTs the value of h_0 is defined in table 4.2. Let us also define a shared reference mortality at a height of $1\ \mathrm{m}$, $\gamma_{\mathrm{ws,1m}} = 0.05\ \mathrm{yr}^{-1}$, taken to roughly follow the increase suggested by Stovall et al. (2019) for small trees.

4.5.3 Fire mortality

To provide a counter example to the positive relationship between water-stress mortality and size, we model fire mortality; γ_{f}. Forests fires typically burn within the under-story, and the duration of fires in environments such as rainforest is normally relatively small (Gora and Esquivel-Muelbert, 2021). Trees within the canopy are not normally effected during rainforests fires (Brando et al., 2012), but can experience increased environmental risk due to other disturbances after the fire, such as from wind-throw (Van Wilgen et al., 2000).

Let us assume a power-law relationship of fire mortality with respect to height:

$$\gamma_{\mathrm{f}} = \gamma_{\mathrm{f},0} \left(\frac{h}{h_0} \right)^{\phi_{\mathrm{f}}}. \tag{4.19}$$

Unlike water-stress, we assume negative value for ϕ_{f}, such that the maximum mortality is at the smallest size-classes. Again we define a reference mortality rate at a height of $1\ \mathrm{m}$ but with a increased mortality rate, over drought of $\gamma_{\mathrm{f},1\mathrm{m}} = 1\ \mathrm{yr}^{-1}$ (Staver et al., 2020).

4.6 Examples of Forest Regrowth

For this section we look at the regrowth of forest ecosystems from such exogenous impacts. This is an important feature for DGVMs to get correct, so that they can capture the environmental and human processes that are modelled within climate projections (Figure 1.1).

To compare with observational data, we use the TropForC-db (Anderson-Teixeira et al., 2016). TropForC-db compiles a list of estimated biomass and carbon density for various pan-tropical sites. We select for sites that are currently experiencing secondary-succession ($\mathrm{site\ age} < 500\ \mathrm{yr}$). As TropForC-db is sourced from various studies, the measurements are not necessarily the ecosystem carbon density. We can increase the number of sites by relying on conversion relationships. For total biomass, TB, we convert to approximate carbon density, M, by multiplying by a factor of one half. For sites with just measurements of above or below ground carbon, AGC or BGC, we rely on the suggested relation-

ship by Saatchi et al. (2011) to find TB:

$$\mathrm{TB} = \mathrm{AGB} + \mathrm{BGB}, \quad \mathrm{BGB} = 0.489\mathrm{AGB}^{0.89}. \tag{4.20}$$

4.6.1 Forest regrowth from agricultural abandonment

To simulate the regrowth of a forest following abandonment of agriculture we initialise to the equilibrium solutions, but with a proportion of the grid-box devoted to land-use. This adjustment requires a modification to the steady-state coverage, equation (4.11), where we essentially add additional "shading" to stop seeds being recruited in the given space being used by land-use, ν_{LU}:

$$\nu_{\mathrm{eq},k} = 1 - \left(\frac{1-\alpha}{\alpha}\right)(1+\mu_0)\,\mu_0 \frac{X_N}{X_G} - \nu_{\mathrm{LU}} - \sum_{l \neq k} c_{kl}\nu_l. \tag{4.21}$$

After this initialisation we set ν_{LU} to zero, thereby "abandoning" the area used for land-use and run RED to the natural equilibrium (Figure 4.12). The result of increasing the initial fraction of ν_{LU}, is that the initial fraction of natural PFTs coverage slowly goes towards zero (Figure 4.12.a). We measure this impact using τ_{90}, which is the time taken to reach 90% of the natural total equilibrium carbon density. We can see from figure 4.12.b that increasing the fraction of land use, increases the RED regrowth time in a Logit-like curve, bar ν_{LU} close to 0 or 1. Having a grid-box which is initially 20% covered by land-use gives a τ_{90} below a century. In contrast, having 80% of the initial grid-box used by land-use increases regrowth times to roughly $250\ \mathrm{yr}$. At $\nu_{\mathrm{LU}} \to 0$, τ_{90} quickly collapse to zero, as the initial carbon density is already past 90%. For $\nu_{\mathrm{LU}} \to 1$, τ_{90} truncates to $\sim 390\ \mathrm{yr}$, as PFTs are removed from the ecosystem. The PFT distribution may also has a significant impact on the behaviour of the regrowth carbon density. If the dominant PFTs are removed from the ecosystem, the regrowth carbon density is more variable. This increases for higher ν_{LU}, with more obvious successional sequences (Figure 4.12.c). When there is no natural vegetation existing, regrowth effectively follows primary succession (Figure 4.11.a), and the duration of successional stages are maximised.

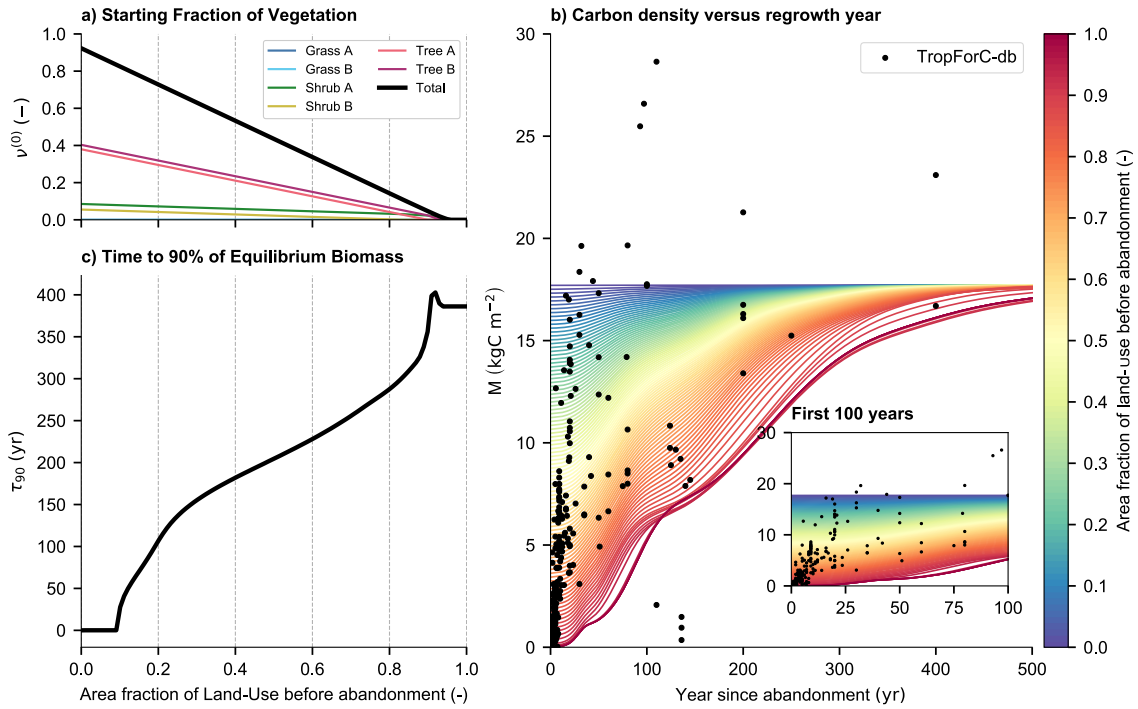

Figure 4.12: Regrowth time-scales following land-use abandonment with PFT values listed in table 4.2. Here RED version 2 is initialised at equilibrium where a proportion of the grid-box is devoted to land-use (a). After this space is made available to natural PFTs, we then record the time taken to reach 90% of the equilibrium carbon density (b). Panel (c) shows the total ecosystem carbon density across the time since abandonment, along with observations of secondary succession of pan-topical sites from TropForC-db. (Anderson-Teixeira et al., 2016).

For the TropForC-db observations the general trend for the first 100 years appears to be quicker when compared with the RED regrowth trajectories. There could be a number of factors which explain these differences. For instance, given the resoultion of TropForC-db focuses on plots at small scale (between $0.1 - 10$ ha), it could be that seed dispersal from within the locality plays a significant role with re-spreading vegetation (Powers et al., 2009). The overall impact of seed dispersal at greater scales is diminished (Snell et al., 2014). Secondly, some of the regimes are plantations which might enhance the growth rate and seed dispersal.

4.6.2 Forest regrowth from fire and drought

Here we look at the impact of size-structured mortality and disturbance duration on the regrowth times in RED version 2. For this we assume the water-stress and fire mortality relationships suggested in the previous sections. We assume

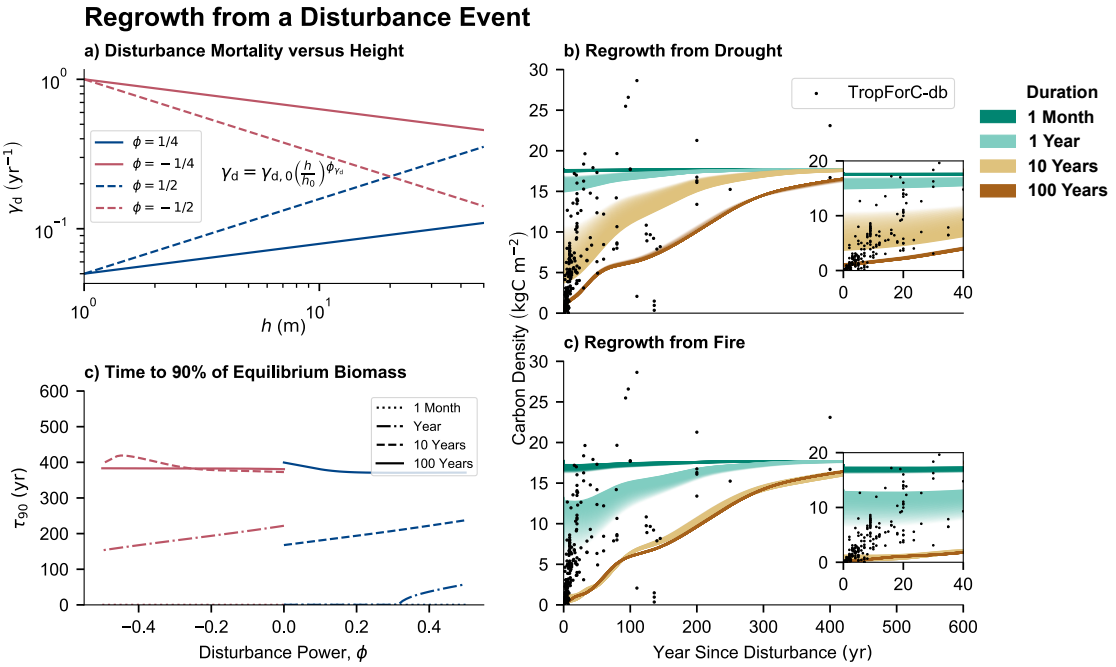

Figure 4.13: Vegetation recovery from a disturbance mortality event with PFTs from table 4.2. Here we assume a power-law relationship with respect to PFT height, h, that is chosen to mimic fire and water-stress mortality (a). Panels b and d show how the total ecosystem carbon density changes across years since disturbance, with observations of secondary succession pan-topical sites from TropForC-db (Anderson-Teixeira et al., 2016). Brown/greens shows the respective duration (dark green: month, light green: year, light brown: decade, dark brown: century) of the disturbance before recovery, with colour opacity indicating the magnitude of the (mortality to height) disturbance power, ϕ (the more opaque the greater $|\phi|$). Panel c shows how the time-scale depends on this power, along with the duration of the disturbance.

a power-law for mortality in relation to plant height, with equations (4.18-4.19), while varying the power between 0 and $1/2$ for water-stress and $-1/2$ to 0 for fire (Figure 4.13.a). This is to capture different levels of size-mortality dependence and to illustrate the importance of such demographic dependent processes can have on ecosystem regrowth time-scales. For γ_{ws}, having a higher power means there is more mortality in the higher size classes. For γ_{f}, having a lower power means that smaller plants are more vulnerable to fire.

After initialising to undisturbed equilibrium, we then run the forest in a period of disturbance, where either γ_{ws} or γ_{f} are added to the baseline mortality, γ_{b} of different ϕ. The duration of the disturbance period lasts for one month, year, decade and a century. After this period, we no-longer apply the disturbance morality and simulate the subsequent recovery to the pre-disturbance equilibrium (Figures

4.13.b & d).

The skewness of disturbance mortality across height has a clear influence on the regrowth time (Figure 4.13.c). Disturbances where taller trees are more at risk, such as drought, see a clear correlation with regrowth time. The mortality caused by droughts is more prolonged, hence the lesser rate of γ_{ws} versus γ_{f}. We see that for a major reduction in the carbon density, droughts must last more than 1 year, even with highly skewed mortality. This agrees with observations droughts could take multiple years to cause sustained carbon loss (Doughty et al., 2015).

Having disturbances more likely to kill smaller trees will decrease regrowth times to 90% of equilibrium biomass. A year long fire, where taller trees are significantly less at risk than smaller trees, potentially results in a small reduction in the total ecosystem carbon-density (Figure 4.13.d). This is because of the allometric inequality in both assimilate and carbon density, as the majority of carbon and growth is stored in largest size-classes (Figure 2.5.b-c). Again, much like the land-use abandonment instance, the gradient of regrowth followed by the TropForC-db appears to be steeper within the first few decades. Another potential factor in recovery time will be frequency of the disturbance. Figure 4.13 only shows the recovery from a single disturbance of varying severity and duration rather than repeated instances disturbances. Repeat disturbances can severely limit the ability of a forest to recover to the prior state (Heinrich et al., 2021).

4.7 Discussion

The princple focus of RED version 2 is to address of the shortcomings of the original implementation of the RED model; mainly regrowth time-scales and PFT diversity. Firstly, RED version 1 assumed a left-handed growth flux in-between mass classes. This underplays the non-linear relationship of growth between m_i and m_{i+1}. The result of this played into the numerical accuracy with respect to the continuous solutions, shifting the size distribution to smaller masses (Figure 4.1), and underestimating the rate of regrowth as larger trees were not being recruited as quickly (Figure 4.1). RED version 2 assumes a new flux in-between masses, g_f. g_f is placed at the point between classes which minimises the difference between continuous and discrete solutions (Figure 4.3). This change also provided better numerical convergence for the dynamic spin-up (Figure 4.2).

RED version 1 had theoretical and practical challenges justifying certain aspects of the recruitment. The classic scheme used an arbitrary boundary mass of $m_0 = 1\ \mathrm{kgC}$ for trees. New recruits would instantaneously be a tree of mass m_0, passing over important and potential interactions involving seeds. Seed sizes could vary substantially depending on species; between a few micro grams up to a few kilograms for the sea coconut, but are generally less than $1\mathrm{kgC}$ (Igea et al., 2017). We found that m_0 was a overtly sensitive parameter in terms of the recruitment flux, and had impacts on the dynamic time-scales (Figure 4.6.c). Additionally, having RED version 1 start from a minimum vegetation fraction could overestimate the time taken to spin up from bare soil, and could provide an additional arbitrary minimum competition by feeding back into equation (3.11) (Figure 4.6.e).

RED version 2 improves the realism of the recruitment boundary layer by including an explicit seed pool. This enables more realistic dynamic processes to be explicitly modelled on seeds, such as mortality or germination rates. m_s, the seed mass, can be estimated using empirical measurements. Secondly, we no longer spin up from a minimum coverage but effectively model a minimum seed density, which can be indicative of seed migration from outside the ecosystem.

The final improvement is the inclusion of diversity among PFT groups (e.g. tree vs tree PFT). Lotka or space-exclusionary DGVMs have traditionally had issues with maintaining co-existence (Arora and Boer, 2006; Scheiter et al., 2013). This is because they have relied on competition coefficients, c, being 1 or 0, which prohibits diversity in the steady-state. Having $c < 1$ provides diversity, but there is a risk of breaking the hard-exclusion rule, this is because the total canopy area can surpass the grid-box area (Figure 4.7). To get around this we must adjust the coverage to account for canopy overlap. We do this by assuming a shared c value for all PFTs within the same level of the original RED competitive hierarchy (Table 4.1). This means that the total top-down coverage is given by a simple mathematical relationship $\nu_{\mathrm{TD}} = c\nu$, which avoids breaking the hard-exclusion rule, equation (4.12). Following the concept of METE (Harte, 2011), we assume a shared competition coefficient of $c = 0.78$ which maximises the non-shared coverage or species abundance (Figure 4.8).

The addition of the new numerical scheme, seed pool, and the diversity helps RED version 2 make significant improvements in terms of regrowth over RED ver-

sion 1 (Figure 4.11). When spinning up from the minimum boundary conditions, RED version 2 gets faster convergence towards the equilibrium solution and faster PFT succession. The addition of the seed pool allows for more nuanced modelling of secondary succession. For example, we can retain the equilibrium seed density, while a disturbance removes the established plants and get significantly quicker regrowth than primary succession (Figure 4.11.b).

For the final part of this chapter, we explore regrowth from land-use abandonment and disturbances within RED version 2. We compare with observations of carbon density and stand age from TropForC-db (Anderson-Teixeira et al., 2016). The fraction of land-use prior to abandonment can have a significant consequence for regrowth time-scales (Figure 4.12). In RED, the τ_{90} time-scale appears to follow a logit function with the amount of prior land-use. Above certain critical levels of land-use ($\nu_{\mathrm{LU}} > 0.8$), the regrowth time is more asymptotic, truncating at the time-scale of primary succession, roughly 390 years (Figure 4.12.b). Compared to the TropForC sites, the regrowth time-scales can appear low but this could be due to the small scale of the sites, thereby there is more significant seed dispersal from outside the ecosystem, and the fact that some sites are plantations with an initial distribution of vegetation. Therefore, for large-ecosystem and ESM purposes it could be more reasonable to look at remotely sensed observations in the future.

To simulate mortality-size interactions of fire and drought, we use a power law relationship. To mimic observed correlations (Gora and Esquivel-Muelbert, 2021), we assume water-stress has a positive power with respect to plant height, and in contrast fire mortality has a negative power. We then investigate by simulating the disturbances on an initial equilibrium state for the durations; a month, year, decade and century, and vary the mortality-height power to see the resultant regrowth (Figure 4.13). We find a complex relationship with this disturbance mortality-power, but in general the less at risk large trees are, the faster the regrowth. This is because, as a result of allometric scaling, the majority of the ecosystem growth and carbon density is within the largest size classes (Figure 2.5).

4.8 Conclusion

RED version 2 represents a marked improvement of realism and theoretical scope over RED version 1, while retaining the important model parsimony (Argles et al., 2020). By including a mid-class flux, g_f, we improve the numerical accuracy relative to the continuous equilibrium solution. The addition of the explicit seed pool both establishes a physical lower boundary for recruitment, and gives more realistic regrowth, providing a framework to better investigate secondary succession. By allowing vegetation to overlap in space ($c < 1$), we now have valid diverse RED steady states.

In this chapter we also illustrate how the improved model and the analytical equilibrium can be easily used in unison to investigate the resultant regrowth from both land-use abandonment and disturbances, such as fire and drought. These results also illustrate the importance of demography on secondary succession.

5 Extensions and Further Applications of Demographic Equilibrium Theory

Rationale for Chapter

Using the RED recruitment and competition as a basis, here we present the continuous analogue for RED - Closed Form Demographic Equilibrium Theory (CF-DET). In this chapter we explore how CF-DET could be used to infer ecosystem resilience, optimality and demography and turnover estimated from macroscopic quantities.

5.1 Background

We can increase the scope of DET by including a recruitment feedback, we call this Closed Form - Demographic Equilibrium Theory (CF-DET), where the number of individuals recruited is proportional to the number of plants within the population. This method of recruitment has been used within dynamic models before (Ribbens et al., 1994), but not devised in the form of analytical equilibrium. Let us first assume that recruitment is a biological tax that has been applied to the total carbon assimilate, P, with some fraction, α, going into recruitment assimilate, P_s, with the remainder going into structural growth, G:

$$P = P_s + G, \quad P_s = \alpha P, \quad G = (1 - \alpha)\, P. \tag{5.1}$$

P_s represents any reproductive litter, such as fruit and seeds. Secondly, that the rate of recruited individuals at the boundary class, m_0, is given as the ratio of P_s to m_0:

$$\text{total recruits} = \frac{P_s}{m_0}. \tag{5.2}$$

5.2 No seed pool

As in RED version 1 (Argles et al. (2020), chapter 3), we initially assume that the total recruits directly enter into the population pool as small trees, without explicit representation of germination or seeds. We use the hard-exclusion approximation as the competitive constraint on space. Seeds cannot grow into already occupied space, ν, and can only be established into free space, s. Therefore, the rate of successful recruits, $n_0 g_0$, is given as:

$$n_0 g_0 = \left(\frac{P_s}{m_0}\right) s, \tag{5.3}$$

where:

$$s = (1 - \nu). \tag{5.4}$$

As already established under the previous chapter, at equilibrium the rate of recruitment must equal the rate of total individuals removed by mortality, equation (2.30); $\gamma N = n_0 g_0$. Given our assumptions about the total assimilate rate, equation (5.1), and the total structral growth in DET, equation (2.44), we can write P_s as:

$$P_s = \left(\frac{\alpha}{1-\alpha}\right) G = \left(\frac{\alpha}{1-\alpha}\right) g_0 N \mathcal{F}_g. \tag{5.5}$$

Therefore, equation (5.3) can be written as:

$$\gamma N = \left(\frac{\alpha}{1-\alpha}\right)\left(\frac{G}{m_0}\right) s, \tag{5.6}$$

which simplifies:

$$\frac{\gamma m_0}{g_0} = \left(\frac{\alpha}{1-\alpha}\right) \mathcal{F}_g s. \tag{5.7}$$

Substituting for ν for s gives us a separate definition for the equilibrium coverage in terms of a few parameters; ϕ_g, α and μ_0:

$$\nu = 1 - \left(\frac{1-\alpha}{\alpha}\right) \frac{\mu_0}{\mathcal{F}_g}, \tag{5.8}$$

or just two when we assume Metabolic Scaling Theory ($\phi_g = 3/4$):

$$\nu = 1 - \left(\frac{1-\alpha}{\alpha}\right) \frac{\mu_0}{1 + \frac{3}{4\mu_0} + \frac{3}{8\mu_0^2} + \frac{3}{32\mu_0^3}}. \tag{5.9}$$

5.3 Including a Seed Pool

We include the addition of the seed class from RED version 2. For this we assume a given seed mass, m_s, which is equivalent to m_0. There are a few benefits for doing this. As outlined in changes made in RED version 2 (Chapter 4), having an explicit seed population pool expands the scope of the model and removes the arbitrary cut-off of m_0, that does not have a robust real-world counterpart.

At equilibrium the number of seeds, N_s, entering the pool is equal to the number of seeds leaving the pool. Seeds leave either by mortality, γ_s, or a germination rate, r_s, into the size-structure:

$$\frac{P_s}{m_s} = N_s \left(\gamma_s + r_s\right). \tag{5.10}$$

Assuming seeds germinate into trees of identical mass, $m_s = m_0$, as previously shown in equation (5.5), we can get P_s in terms of N. By using the relationship for the rate of recruits, equation (5.2), we get:

$$\left(\frac{\alpha}{1-\alpha}\right) \frac{g_0}{m_s} N \mathcal{F}_g = N_s \left(\gamma_s + r_s\right). \tag{5.11}$$

Another equilibrium constraint is that the rate of successful germination into trees must be equal to the total number of tree deaths. Assuming successful seeds are only allowed in free-space, s, we have:

$$\gamma N = N_s r_s s, \tag{5.12}$$

which rearrange for N_s, gives the equilibrium seed density:

$$N_s = \frac{\gamma N}{r_s s} = \frac{\gamma N}{r_s(1-\nu)}. \tag{5.13}$$

We now have all the relationships needed to find the equilibrium coverage. Substituting equation (5.13) into equation (5.11) and rearranging for ν, gives us:

$$\nu = 1 - \left(\frac{1-\alpha}{\alpha}\right)\left(1 + \frac{\gamma_s}{r_s}\right)\frac{\mu_0}{\mathcal{F}_g}, \quad \frac{\gamma m_s}{g_0} = \mu_0. \tag{5.14}$$

While we have added two new parameters, γ_s and r_s, we can make some addi-

tional assumptions that simplify the equilibrium solutions.

5.3.1 Growth/germination equivalence

Firstly, that the rate of germination is equivalent to the ratio of the lower boundary growth and mass:

$$r_s = \frac{g_0}{m_0}, \tag{5.15}$$

this gives us the adjustment involving the seed to plant mortality ratio:

$$\nu = 1 - \left(\frac{1-\alpha}{\alpha}\right)\left(1 + \frac{\gamma_s \mu_0}{\gamma}\right)\frac{\mu_0}{\mathcal{F}_g}. \tag{5.16}$$

5.3.2 Seed/plant turnover equivalence

The assumption that the ratio γ_s/r_s is equal to μ_0, the equilibrium coverage is given as:

$$\nu = 1 - \left(\frac{1-\alpha}{\alpha}\right)(1+\mu_0)\frac{\mu_0}{\mathcal{F}_g}. \tag{5.17}$$

5.3.3 Immortal seeds or $\gamma_s << r_s$

Assuming that $\gamma_s \to 0\ \mathrm{yr}^{-1}$ or that the germination rate is significantly greater than the seed mortality rate, we find that the seed pool equation (5.14) becomes consistent with the no-seed pool case, equation (5.8):

$$\nu = 1 - \left(\frac{1-\alpha}{\alpha}\right)\frac{\mu_0}{\mathcal{F}_g}. \tag{5.18}$$

5.4 Critical Regions

The functional form given by equation (5.18) implies that the equilibrium coverage can go below zero. This gives a critical region within μ_0 and α space where a forest is able to sustain itself:

$$\nu = 0 = 1 - \left(\frac{1-\alpha}{\alpha}\right)\frac{\mu_0}{\mathcal{F}_g}. \tag{5.19}$$

Equation (5.19) implies that there is a balance of tree mortality, growth and recruitment in which a forest is able to exists. By plotting out the equilibrium coverage

versus $\mu_{1\mathrm{kgC}}$ and α, we find parameter region that sustains a forest (Figure 5.1). If the turnover value, μ_0, is too high and the corresponding α is small, then the size profile is not sustainable. Low assimilate and low reproductive litter implies there is never enough plants entering the population to counteract the loss of population through mortality. By plotting out the equilibrium coverage versus $\mu_{1\mathrm{kgC}}$ and α, we get an idea of allowed parameter space that sustains a forest.

Figure 5.1 hints at why we see different plant strategies in terms of the balance of these traits. A plant which contributes more to seeds, and thus less to structural growth, has a wider tolerance to increasing μ_0 or turnover. This is contrasted with plants that are long-lived and contribute a relatively small amount to recruitment, and are thus more likely to have larger trees (Figure 2.4). Figure 5.1 also shows that the rate of seed germination and mortality, $m_s = 0.02\mathrm{kgC}$, is relatively insensitive to low $\mu_{1\mathrm{kgC}}$ values in comparison to higher $\mu_{1\mathrm{kgC}}$. Different rates of seed turnover (solid, dashed-dotted, dashed and dotted black lines) converge for low $\mu_{11\mathrm{kgC}}$ and diverge for at higher $\mu_{1\mathrm{kgC}}$ for the same coverage.

In a raised disturbance environment, such as increased frequency of fire and/or drought caused by climate change, the per unit change in γ for the “Live Fast, Spread Fast” strategy could potentially win out over PFTs that adhere to the “Live Slow, Spread Slow” one. Potentially changing the species composition through dieback (de L. Dantas et al., 2013; Beckman et al., 2018). We see that in high disturbance regimes, successful species rely on high cost recruitment strategies in fire regimes (Enright et al., 2014) and droughts (Suarez and Kitzberger, 2008), such as shrubs or grasses.

Another anthropogenic interaction is how growth and mortality (Bugmann and Bigler, 2011; Friend et al., 2014) may change with increased CO_2 fertilisation and the impact on the composition of a forest (Feeley et al., 2011). It is understood that demographic interactions play an important role in the response (Needham et al., 2020).

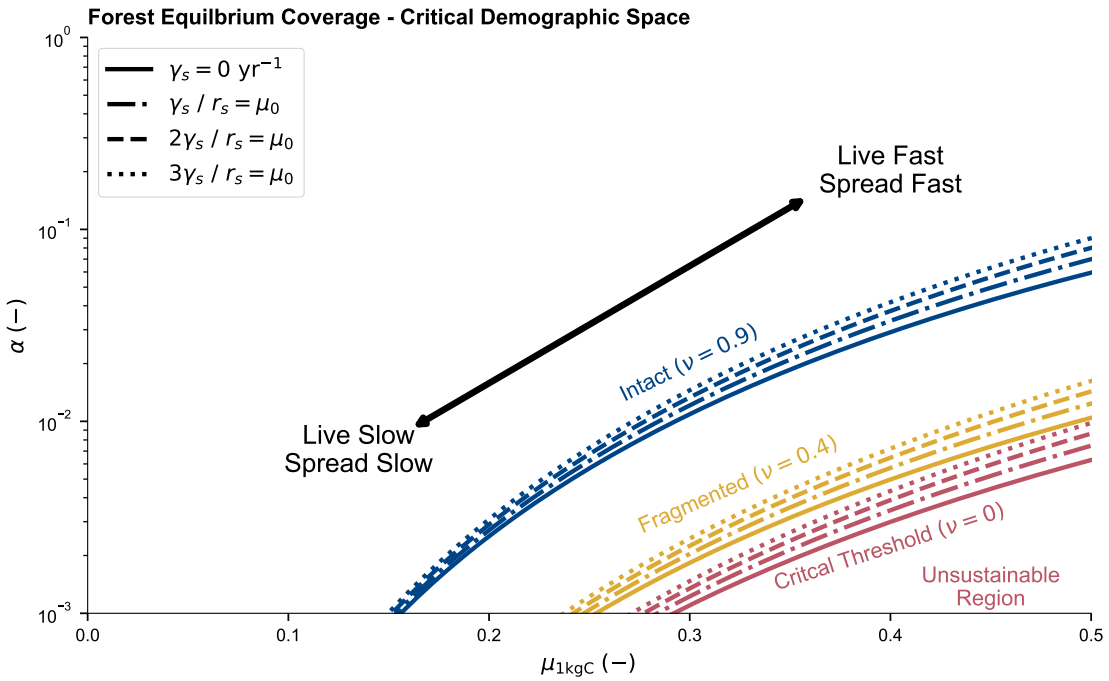

Figure 5.1: How equilibrium forest coverage, ν, varies with the turnover parameter, $\mu_{1\mathrm{kgC}}$, and assimilate reseed fraction, α. Using the previous figure 2.1 as a guide, we see critical regions of where a forest may begin to fragment (yellow) or even disappear (red) at equilibrium for a combination of mortality and growths. Dotted line to solid line indicates various rates of seed germination and mortality, relative to μ_0.

5.5 Forest Quantities in CF-DET

Using the boundary constraint on coverage it is possible to derive the total allometric quantities of Z in terms of α rather than total number density N and μ_0. The total coverage is given by integrating over the crown area across size by equation (2.50), and also by competitive relationships from the earlier sections. This means that in terms of ν, N is given by:

$$N = \frac{\nu}{a_0 \mathcal{F}_a} \tag{5.20}$$

Looking at the no seed pool instance, equation (5.8), we can find the equilibrium number density in terms of α and μ_0:

$$N = \frac{1}{a_0 \mathcal{F}_a} \left[1 - \left(\frac{1-\alpha}{\alpha} \right) \frac{\mu_0}{\mathcal{F}_g} \right]. \tag{5.21}$$

This naturally leads into a general relationships in terms of a allometric variable. For this we use the dummy z notation from section 2.2, with Z being the total quantity density and ϕ_z being the allometric scaling exponent in relation to mass. When we substitute equation (5.20) into equation (2.39) we can find the ecosystem quantity that no longer depends on N:

$$Z = \left(\frac{z_0 \mathcal{F}_z}{a_0 \mathcal{F}_a} \right) \nu. \tag{5.22}$$

The total quantity can vary substantially across μ_0 and α space dependent on the balance between the scaling coefficients; ϕ_g, ϕ_a and ϕ_z. Let us consider how ϕ_z and Z may vary if we assume constant parameter values for the terms; $\phi_g = 3/4$, $\phi_a = 1/2$, $\alpha = 0.05$. For this we consider the dimensionless ratio of $Z a_0 / z_0$ plotted against ϕ_z, to more easily demonstrate the dependency of Z with the given parameters (Figure 5.2.a). If the quantity scales faster than the crown area, $\phi_z > \phi_a$, that quantity is area-weighted towards larger plants. For instance, ecosystem biomass or growth, are maximised when $\mu_0 \to 0$ and the size-structure approaches self-thinning rules. At low μ_0 high coverages, this can increase super-linearly (Figure 5.2.b).

An allometric exponent which has $\phi_z = \phi_a$ will have a linear proportionality with respect to coverage. As we expect from equation (5.22) Z goes to $Z = z_0 / a_0 \nu$. A allometric variable which has $\phi_z < \phi_a$ we will get a non-monotonic function with respect to μ_0, α and ν (Figure 5.2.c). There will be an optimum μ_0 to maxmises the quantity within an ecosystem. For instance, natural forests typically maximise the stand density when the coverage less than 100% (Lieberman et al., 1995; Sprintsin et al., 2009). This could imply that tree species may have evolved to maximise for number density within their ecosystems.

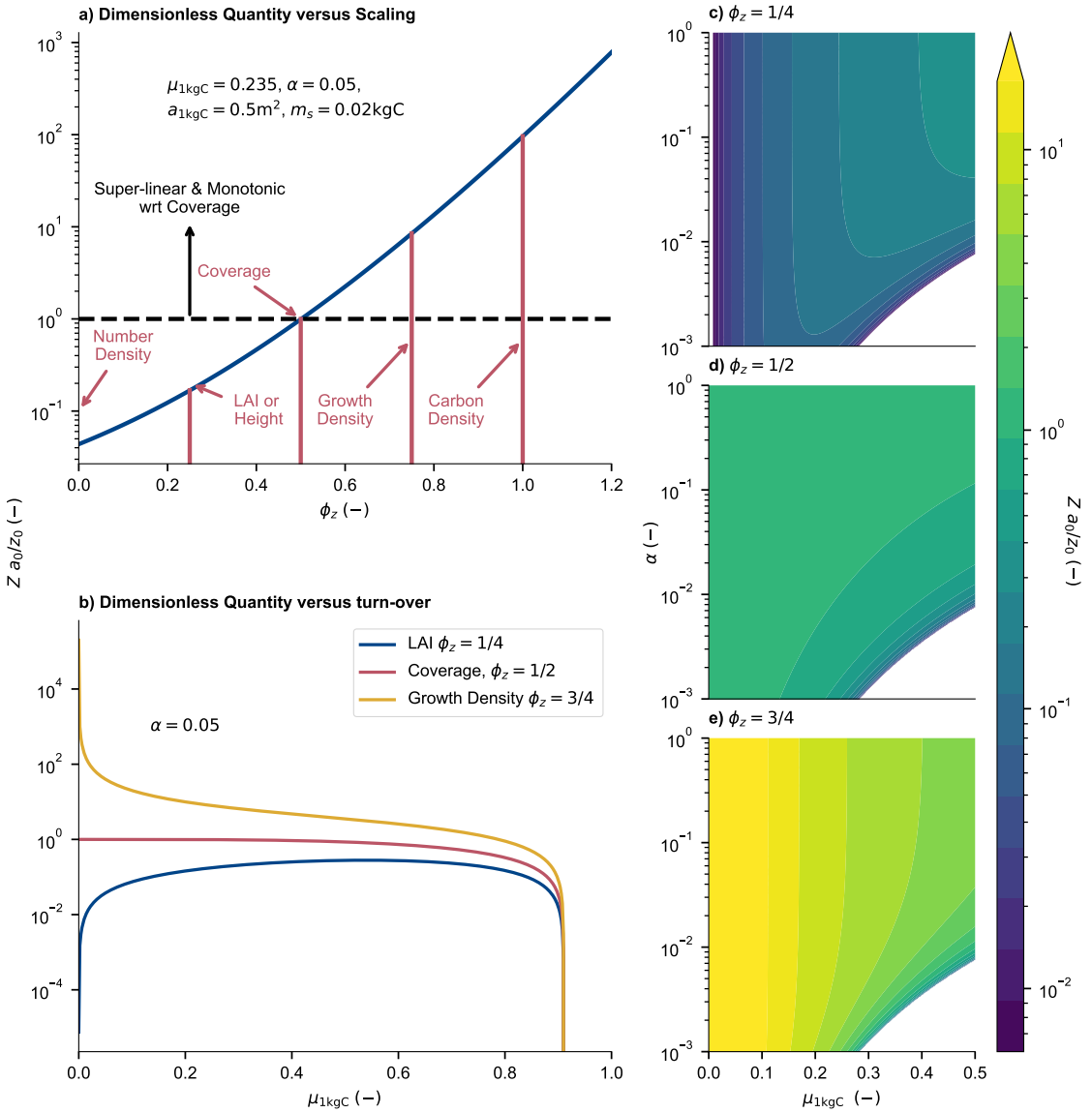

Figure 5.2: How a allometric quantity varies across reproduction, growth and mortality under CF-DET (c-e). For an arbitrary dimensionless quantity, equation (5.22), we see how the quantity varies with respect to the allometric power, ϕ_z (a). ϕ_z also affects the general shape of the quantity relative to the turnover (b).

5.6 Estimations using CF-DET

Given the low number of parameters in CF-DET, chiefly μ_0 and α, it is possible to infer from observations of forest quantities such total biomass, coverage, or average height, the necessary demographic size-distribution. Given α and assumed allometric constants, a_0 and m_0, we can solve for the μ_0 that is consistent with the observations. In this section we will outline a few examples of where this could be of benefit; for evaluations at site, regional, and global scales.

5.6.1 Pan-tropical Carbon Density

Using TropForC-db observations of pan-tropical forests Anderson-Teixeira et al. (2016), we can find μ_0 consistent with the carbon density measurements. We first filter for old-growth sites with measurements of carbon densities. We can expand the number of sites by employing the method used in chapter 4, by converting from measurements of total, above and bellow ground biomass to total carbon density.

Assuming a seed pool of equivalent turnover with μ_0, equation (5.17), we take equation (5.22) with $z \to m$, such that the total carbon density is given as:

$$M = \left(\frac{m_0 \mathcal{F}_m}{a_0 \mathcal{F}_a}\right) \left[1 - \left(\frac{1-\alpha}{\alpha}\right)(1+\mu_0)\frac{\mu_0}{\mathcal{F}_g}\right]. \tag{5.23}$$

Let us assume that $\phi_g = 3/4$, $\phi_a = 1/2$, $m_0 = 0.02\ \mathrm{kgC}$, $a_{1\mathrm{kgC}} = 0.5\ \mathrm{m}^2$, and $\alpha = 0.03$. We then iterate the difference between equation (5.23) and the observations to find the necessary $\mu_{1\mathrm{kgC}}$ for equivalence.

Additionally, we can compare the TropForC-db fits of $\mu_{1\mathrm{kgC}}$ to the fitted estimates of the RAINFOR sites (Moore et al., 2020). Figure 5.3 shows the results across $\mu_{1\mathrm{kgC}}$ and α space. From this, we see that CF-DET can also imply other forest properties; stand density, coverage and seed density. Which allows us to get to the underlying size-structure across mass (Figure 5.3). Using such combinations of datasets it may be possible to constrain areas within this parameter space. Such a constraint would help with research to see if forest optimise a particular characteristic (Figure 5.2).

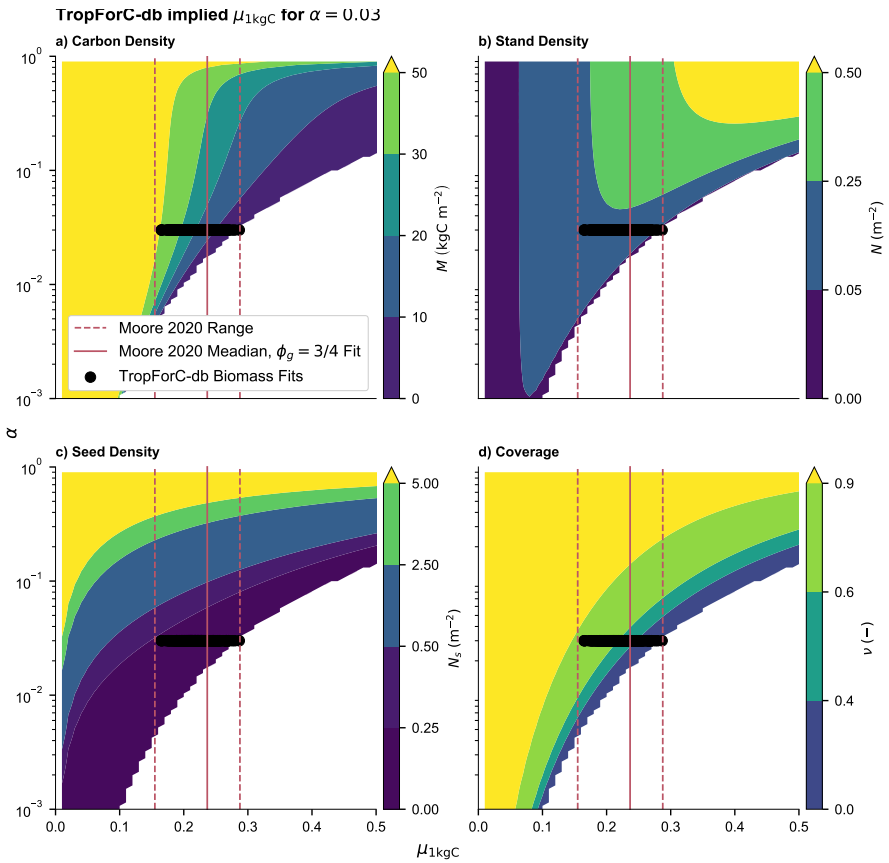

Figure 5.3: Distribution of α vs $\mu_{1\mathrm{kgC}}$ space for (a) carbon density, (b) stand density, (c) seed density and (d) coverage, along with fitted parameter values for $\mu_{1\mathrm{kgC}}$. The black markers are inferred from observations of pan-tropical carbon densities from TropForC-db (Anderson-Teixeira et al., 2016). The red lines is the median and range of the $\mu_{1\mathrm{kgC}}$ estimates from Moore et al. (2020).

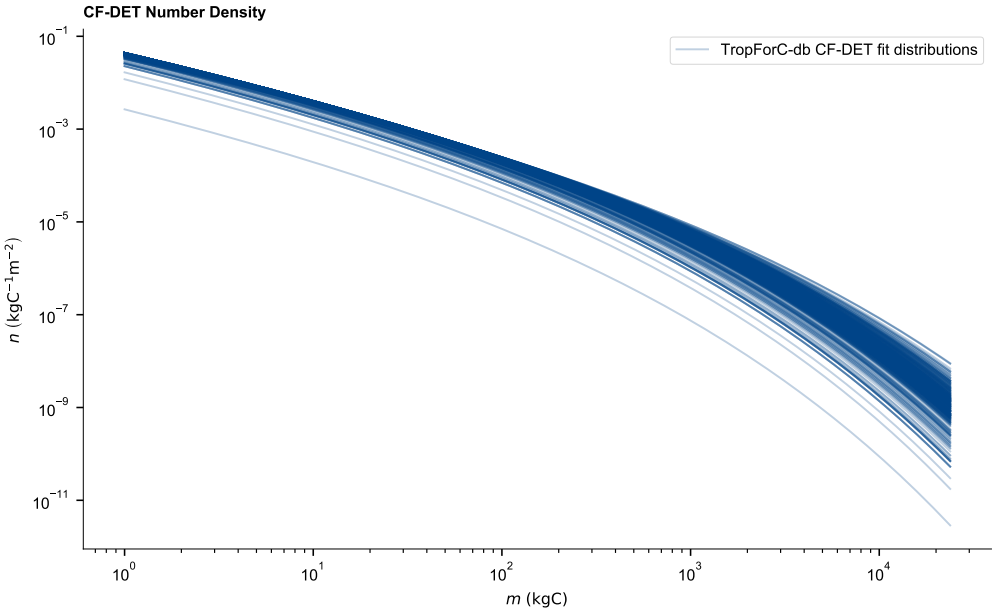

Figure 5.4: CF-DET fitted number density (blue) for the TropForC-db carbon density measurements.

5.6.2 The Forest Carbon Budget of Great Britain

To demonstrate the feasibility of CF-DET at a regional level, in this section we make a comparison of regional totals of carbon between CF-DET and inventory data for Great Britain. We fit μ_0 to equation (5.8) to get the tree cover to match the $0.05° \times 0.05°$ degree observational data from the NASAs MODIS-VCF for 2011 (Figure 5.5.a) (Hansen and Song, 2018). We use the parameters $\alpha = 0.1$, $a_0 = 0.5\ \mathrm{m}^2$, and $m_0 = 1\ \mathrm{kgC}$, we then use equation (5.23) for the carbon density but with the modification of no seed pool[1] (Figure 5.5.b):

$$M = \left(\frac{m_0 \mathcal{F}_m}{a_0 \mathcal{F}_a}\right)\left[1 - \left(\frac{1-\alpha}{\alpha}\right)\frac{\mu_0}{\mathcal{F}_g}\right]. \tag{5.24}$$

The total region carbon is given by summing the product of the grid-box area and the carbon density at each grid-box.

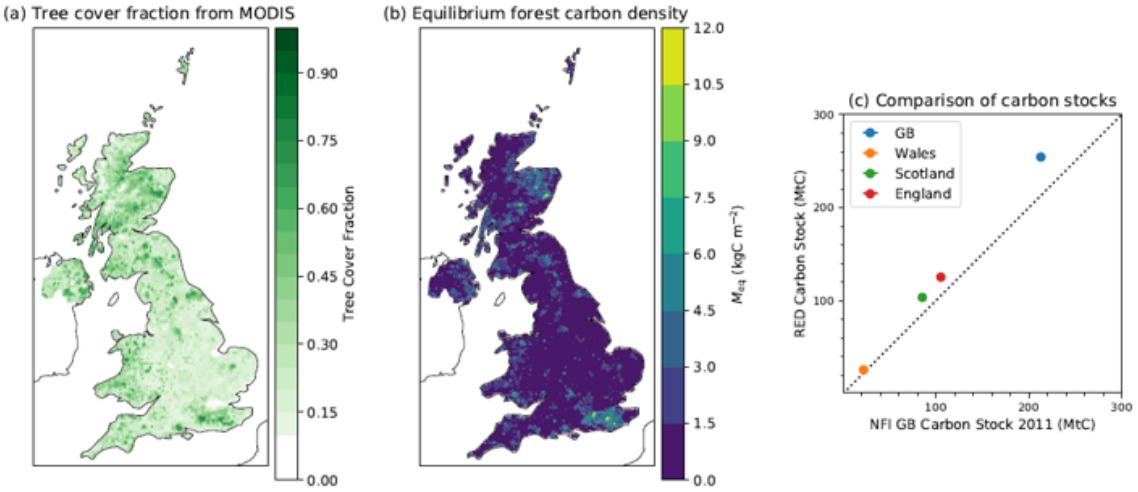

Figure 5.5: Comparing remotely sensed MODIS tree cover fraction (Hansen and Song, 2018) (a), along with inverted CF-DET Carbon Density (b). Panel (c) shows the comparision between aggregate carbon stock inventory against CF-DET (RED) for the nations in Great Britain.

When compared with total carbon from the UK National Forest Inventory (NFI) for the year of 2011 (Jenkins et al., 2011), the CF-DET carbon density is close to these bottom-up census for each country within GB. Although does generally overestimate (Figure 5.5.c). This could partly be due to forests not being in equilibrium.

[1] This test was done before the implementation of the RED version 2 seed pool. Hence we use older parameter values (Chapter 3).

5.6.3 Global Forest Carbon Turnover

A final example inverting the CF-DET equations, is estimating carbon residency times, τ. τ is a quantity that measures the duration of carbon within a system, that is a useful measure for evaluating remotely sensed observations to ESM and DGVMs (Carvalhais et al., 2014; Koven et al., 2015; Erb et al., 2016; Wu et al., 2018; Forkel et al., 2019; Pugh et al., 2020). For instance, Carvalhais et al. (2014) found that the CMIP5 models predict faster than expected turnover for arid regions for both the vegetation and soil pools. τ is typically measured by dividing the carbon density by the carbon flux into the system; such as NPP, Π_{NPP}:

$$\tau = \frac{M}{\Pi_{\mathrm{NPP}}}. \tag{5.25}$$

Equation (5.25) is only valid when the ecosystem is in equilibrium. The assumption of equilibrium is not consistent with observations in certain instances; Erb et al. (2016) found that this is especially true in areas of heavy land-use.

To demonstrate how CF-DET can be used to find the carbon turnover, we combine the $0.05^\circ \times 0.05^\circ$ MODIS tree cover fraction data (Hansen and Song, 2018), with unscaled $1\mathrm{km} \times 1\mathrm{km}$ resolution MODIS NPP data (Running et al., 2015), that is averaged between 2000-10. We then assume the same parameters used in the previous section; $\alpha = 0.1$, $a_0 = 0.5\ \mathrm{m}^2$ and $m_0 = 1\ \mathrm{kgC}$. Solving for the coverage using equation (5.8), we infer the CF-DET carbon density. After this we then divide by the observed Π_{NPP} to find the τ required for equilibrium to be true.

Figure 5.6 shows the CF-DET carbon residency time globally. Some savannah and areas of heavy land-use, such as the south east of Brazil and Southern and Eastern Africa, suggest a very quick duration of carbon passing through forests. There are large carbon residency times in tropical forests such as the Amazon but also in arid-desert regions such as across Sahel or in Western India. Compared with earlier studies this approach captures a similar spatial distribution, but overestimates the magnitude in tropical forests (Carvalhais et al., 2014; Pugh et al., 2020). As in section 5.6.2, this could partly be due to overestimation of the biomass due to some forests not being in equilibrium.

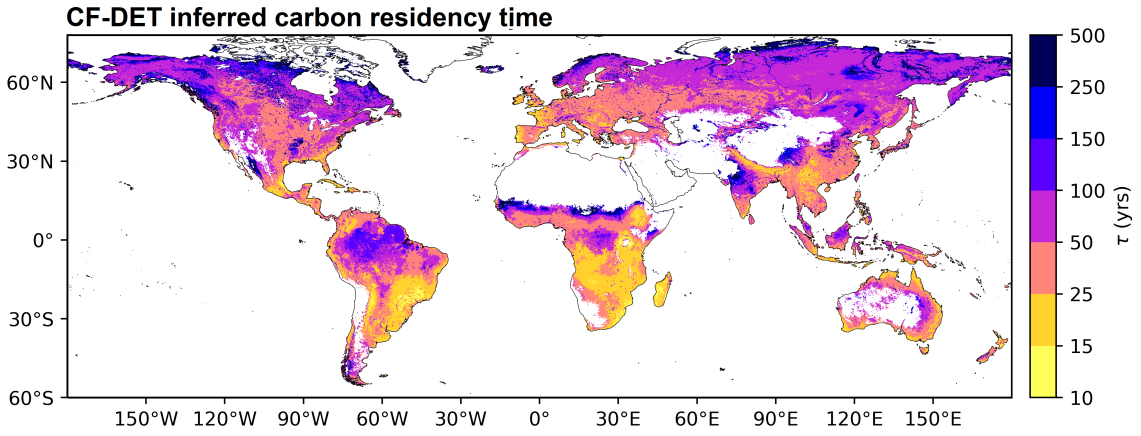

Figure 5.6: Global carbon residency times for vegetation produced by fitting CF-DET coverage against MODIS tree cover fraction for the years of 2000-2010 (Hansen and Song, 2018). The Carbon density was then divided by up-scaled observed NPP (Running et al., 2015) using equation (5.25).

5.7 Conclusion

CF-DET attempts to relate the large scale attributes of a forest to size-structured demography. It has been formulated by closing DET by including a reproductive feedback, equation (5.3), and assuming that a fraction of assimilate, α, goes into reproduction. CF-DET also provides a simple framework to understand how dynamical forests perform at equilibrium, and helps us answer what rates of turnover and fecundity are sustainable in the long-run (Figure 5.1).

CF-DET, being an expansion of DET, is consistent with the latter validation of fitted Weibull distribution (Moore et al., 2018, 2020). It also provides a broad number of analytical solutions for total ecosystem quantities, such as carbon density (section 5.5). CF-DET has the potential to constrain forest turnover and recruitment with measurements of demography or ecosystem totals from sites (section 5.6.1) or from remote sensing.

We provide examples of how the analytical solutions of CF-DET can be combined with remotely sensed measurements. Using MODIS tree coverage (Hansen and Song, 2018) data we invert the coverage equation 5.8 to find μ_0. This can provide us regional carbon density measurements that can be compared with national surveys. Additionally, when also used with MODIS NPP measurements (Running et al., 2015), CF-DET can estimate implied carbon residency times globally (Figure 5.6).

The low number of parameters and analytical equations of CF-DET, when

contrasted with the dynamical models, allows for both direct comparison with the resolution of remotely sensed data and inventory data.

6 Conclusions

Rationale for Chapter

This chapter summarises the conclusion of this thesis and identifies promising directions for future research.

In Chapter 1, we reviewed the motivation and issues of modelling vegetation at large scale, and from this derive the overall objectives for the thesis. The climate and vegetation have many significant interactions (Cox et al., 2000; Friedlingstein et al., 2001). Plants influence surface albedo, and the carbon & hydrological cycle (Sellers and Dorman, 1987; Bond et al., 2008; Friedlingstein et al., 2020). Environmental, (e.g. fire & drought) and human factors (e.g. land-use change) can impact the resilience of forest ecosystems. This inter-dependency leads to uncertainty in ESM for climate protections that arise from Dynamic Global Vegetation Models (DGVMs) (Arora et al. (2020) & figure 1.1).

It is understood that plant size and age play a major role in some of these processes, such as carbon sequestration (West et al., 1997), and disturbances such as fire or drought (Gora and Esquivel-Muelbert, 2021). Yet a large number of popular DGVMs have to compromise for modelling at large scales or simply do not represent plant size or age at all. Cohort DGVMs represent an intermediate complexity approach between the simplicity of area-averaged and individual based models. As a result, cohort DGVMs are becoming more frequent in use (Figure 1.2). These use demography through size and/or age classes to capture both small and large scale processes (Fisher et al., 2018).

This thesis reports on the development of the Robust Ecosystem Demography (RED) model, that uniquely focuses only on plant size as the single demographic dimension (Moore, 2016; Argles et al., 2020). To that end we use two initial

principles for large scale vegetation dynamics, firstly, that the geographic distribution of vegetation at equilibrium is governed by climatic and human factors, and secondly, competition across space can be captured using the hard exclusion approximation. From these initial assumptions we set out to model demography of forests at large scales using two objectives. Firstly, what statistical and demographic theories are used to mathematically explain the distribution of trees within forests and how does this inform us on the characteristics, such as the distribution of carbon biomass within forests. Secondly, to further develop the Robust Ecosystem Demography (RED) Dynamic Global Vegetation Model. The goal for RED is to develop a demographic model which occupies the middle ground of complexity, which is tractable enough to allow for easy future development of other dynamic processes.

6.1 Analysis of the demography of forests

In chapter 2, we showed that Demographic Equilibrium Theory (DET) is adequate for explaining observed regional forest demography. This suggests that the forest size structure at equilibrium arises through Metabolic Scaling Theory (MST) (West et al., 1997) and size-invariant mortality. Under these assumptions, the Fokker-Plank equation, which describes the change of number density across size, integrates to give a truncated a Weibull distribution. Not only is DET able to explain the emergence of the self-thinning power-law, but in addition it is also able to explain the sharper decline in number density for larger trees. This result has been validated across a variety of regions and situations; for USDA forest inventory data in North American (Moore et al., 2018) and RAINFOR sites in South America (Moore et al., 2020).

To answer how much carbon is stored and how this arises through demography, we integrated the DET curve with respect to power-law allometric functions for mass, height, basal diameter and crown area. This combination of DET and allometry yields further relationships for total and average ecosystem properties, such as the total carbon density or average plant height (section 2.2.2). A unique feature of this is that we can also see how such quantities are distributed within a forest. From this solution and the RAINFOR fits, we see that forest coverage, growth and carbon density are skewed towards larger trees, the skewness

of which depends on the allometric power and tree turnover rates (Figure 2.5). Therefore, by the power of physical scaling of growth and mortality, forests are inherently unequal ecosystems in many qualities.

In chapter 5, we took forest equilibrium further by deriving an expanded theory: Closed-Form Demographic Equilibrium Theory (CF-DET). CF-DET is based on combining the continuous DET solutions with the recruitment and competitive constraints of the RED model. This theory allows us to see how forest coverage depends on recruitment and turnover, through two critical parameters α vs μ_0 and detail regions of this parameter space which are unsustainable (Figure 5.1). When combined with allometric scaling, CF-DET may suggest natural optimisations for certain variables, such as height, leaf area index or number density (Figure 5.2). We also demonstrated how such a theory can use remote sensing to infer large-scale demography and carbon densities.

6.2 Development of the RED model

As a foundation we take the assumptions of DET; MST and size invariant mortality, as a basis to model how the forest size-structure may change through time. Chapter 3 is an adapted version of the RED model paper (Argles et al., 2020). For the RED DGVM we partition plants onto carbon mass classes and use MST and PFT allometric functions of growth and canopy area to scale between ecosystem totals, and disaggregate onto classes. For recruitment RED assumes a proportion, α, of the total ecosystem carbon assimilate, P, is used for spreading plants of mass m_0. PFT seedlings are limited to the space they can expand into by a TRIFFID like (Cox, 2001) competition hierarchy (Figure 3.1 & table 3.3). As known in the literature (Arora and Boer, 2006), this form of competition results in the limiting of forest diversity at equilibrium. RED is designed to be modular, allowing for easy integration into ESM (Figure 3.2). As RED is consistent with CF-DET, we can use semi-analytical approaches to find the necessary mortality rates to be consistent with observed global PFT distributions (Figure 3.5).

In RED version 2, we seeked to address some remaining issues within version 1. Issues concerned the implementation of the numerics, the recruitment, and PFT diversity. To improve the numerics we modified the population flux-scheme, making the model more consistent with the continuous equilibrium solutions of

CF-DET (Figure 4.3). We also reduce the reliance on arbitrary parameters (such as m_0 and $\nu_{\min}$) at the recruitment boundary, by introducing an explicit seed pool. This expands, for little cost in complexity, the scope of the model. Both the new flux scheme and seed pool improve the realism of ecosystem dynamics by decreasing regrowth times (Figure 4.9 & 4.10). Additionally we change the competition coefficient to be less than one; $c < 1$, selecting a value which maximises the diversity (Figure 4.8). This allows for more PFTs to coexist in the steady state, while increasing inter-PFT succession (Figure 4.11).

Using RED version 2, we performed a simulation of forest regrowth following abandonment from land-use (Figure 4.12). We also simulated size dependent drought and fire disturbances (Figure 4.13. This was done to highlight the importance of demographic processes on regrowth time-scales and to provide an example of how RED would perform using additional disturbance mortality. The results suggest that disturbances which target larger trees, i.e. long-term droughts through water-stress, would significantly impair the forest rate of recovery to the steady state biomass. As demonstrated earlier by the combination of DET and allometry, this is because most of the growth and carbon density of a forest is within the biggest size classes.

6.3 Areas of future study

With CF-DET and RED version 2, we now have a strong framework to explore multiple avenues of interests. The analytical solutions of forest equilibrium provided by CF-DET offer a simple method to investigate critical rates of forest transition. The theory suggests there is an inherent optimality for forest that exists due to combinations of recruitment and turnover.

The most urgent practical matter is now to fully integrate RED into an ESM. RED will also be implemented into future versions of the UKESM model (Kelley et al., 2021). There is also a significant amount of parallel work going to capture wildfires (Burton et al., 2019), drought (Eller et al., 2018, 2020; Jones et al., 2020) and land-use transitions (Littleton et al., 2020) within JULES. The demography offered by RED will improve the representation of the vegetation response to these disturbances. RED can also be used to model how countries may meet there net zero targets through afforestation and reforestation. For instance, in

the UK this could involve parametrisation of RED for native and plantation tree species (Bateman et al., 2021). Applications of CF-DET and JULES-RED have the potential to improve the understanding and prediction of how forests will respond to the combined pressures of land-use change, CO_2 increases and climate change in the future. For example, CF-DET allows us to clearly visualise the important traits which gives a forest its resilience (Figure 5.1), while JULES-RED coupled will give us environmental projections of ecosystem resilience globally.

A Optimising mass binning for RED

Inevitably discretised models will not exactly reproduce exact continuum analytical solutions, as a result of numerical inaccuracies that arise from using a finite number of mass classes. However, where exact analytical solutions exist they can be used to benchmark numerical models and optimise discretisation schemes, which is what we set out to do in this appendix. We compare the continuum analytical solution for the equilibrium coverage, equation 5.9, to results from RED with differing numbers of mass classes m_i and a geometric mass class scaling, $m_{i+1} = \xi m_i$. Figure A.1.a shows how the relationship between ν_{eq} varies with μ_0 for the exact continuum solution (black line) and variants of the numerical version of RED with different numbers of mass classes (coloured lines). As hoped, results from the discretised model converge on the exact solution as the number of mass classes increases.

The numerical versions of RED shown in figure A.1(a) each use a value of ξ that is near optimum for the number of mass classes, as shown in panels (b) and (c) of figure A.1. Optimum ξ values reduce from about 2.3 for 10 mass classes to 1.1 for 100 mass classes. This variation results from a trade-off. For a given number of mass classes, small values of ξ give greater numerical accuracy, but explicitly model less of the mass range, and the opposite is true of large ξ values. As a result, optimum values of ξ an be defined for each number of mass classes as outlined below.

For geometric scaling any mass can be expressed in terms of m_0, by writing $m_i = m_0(\xi)^i$. Therefore, by using $m_{i+1} - m_i = m_0(\xi)^i(\xi - 1)$, we find that our equilibrium form of λ_i is reduced to:

$$\lambda_i = \frac{\xi^{(\phi_g - 1)(i-1)}}{\xi^{i(\phi_g - 1)} + \mu_0(\xi - 1)}, \quad \lambda_I = \frac{\xi^{(\phi_g - 1)(i-1)}}{\mu_0(\xi - 1)} \tag{A.1}$$

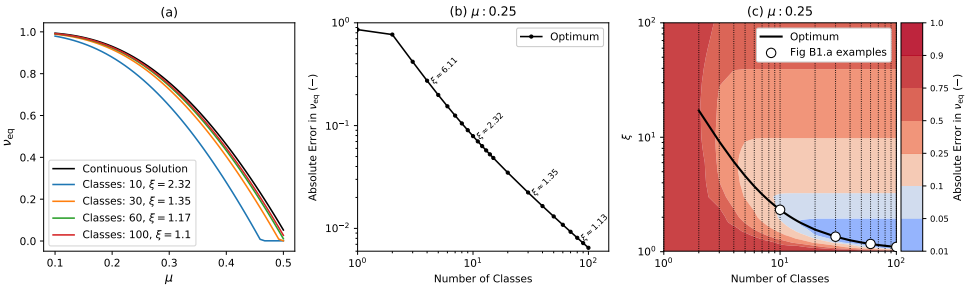

Figure A.1: Comparison of the discretised model to the continuum analytical solution, showing convergence for higher numbers of mass classes. This example uses parameters for Broadleaf Evergreen Tropical trees (BET-Tr PFT) with $\alpha = 0.1$: (a) equilibrium coverage ν_{eq} versus μ_0 for the exact continuum solution (black line) and discretisations of the mass dimension with varying numbers of mass classes and mass class width scaling (ξ); (b) absolute error in the modelled value of ν_{eq} against the number of mass classes using the optimum value of ξ for each case; (c) optimum ξ versus number of mass classes, with contours showing the absolute error in ν_{eq}. Panels (b) and (c) assume $\mu_0 = 0.25$. The white dots in (c) have the same number of classes and scaling as the discrete lines in (a).

From figure A.1.c we see that there is an optimum value for ξ, the geometric scaling for a given number of classes, which minimises the difference between the continuous and discrete forms. This can be found by taking the difference of the continuous and discrete coverages and differentiating with respect to ξ to find the minima. It should be noted that as the continuous form is not dependent on ξ, we get:

$$\frac{\partial}{\partial \xi}\left[\nu_{\mathrm{eq,continuous}} - \nu_{\mathrm{eq}}\right] = -\frac{\partial}{\partial \xi}\left[\nu_{\mathrm{eq}}\right] \tag{A.2}$$

where ν_{eq} corresponds with the discrete equilibrium, equation (3.31), with $\nu_{\mathrm{eq}} = (1 - s)$). Setting equation (A.2) equal to zero we reduce the relationship to only a dependence on X_N and X_G:

$$0 = \frac{\partial}{\partial \xi}\left[\frac{X_N}{X_G}\right] = X_G X'_N - X'_G X_N \tag{A.3}$$

Finding the partial derivative of X_N, using the geometric form of equation (3.20), we get:

$$X'_N = \sum_{j=1}^{I}\left[\left(\prod_{i=1}^{j}\lambda_i\right)\left(\sum_{i=1}^{j}\frac{\lambda'_i}{\lambda_i}\right)\right] \tag{A.4}$$

and for X_G:

$$X'_G = \sum_{j=1}^{I} \left[\xi^{j\phi_g} \left(\prod_{i=1}^{j} \lambda_i \right) \left(j\phi_g \xi^{-1} + \sum_{i=1}^{j} \frac{\lambda'_i}{\lambda_i} \right) \right] \tag{A.5}$$

Finding λ'_i we get:

$$\lambda'_i = \lambda_i \left[(1-i)(\phi_g - 1)\xi^{-1} - \lambda_i \left(i(\phi_g - 1)\xi^{\phi_g - 2} + \mu_0 \xi^{(i-1)(1-\phi_g)} \right) \right] \tag{A.6}$$

and for the top class, λ'_I:

$$\lambda'_I = \left(\frac{(1-\xi^{-1})(I-1)(\phi_g - 1) - 1}{\xi - 1} \right) \lambda_I \tag{A.7}$$

To numerically solve for the minimum, we must differentiate equation (A.3), with respect to ξ. Through the product rule we get:

$$\frac{\partial^2}{\partial \xi^2} \left[\frac{X_N}{X_G} \right] = X_G X''_N - X''_G X_N \tag{A.8}$$

Differentiating equation (A.4) and simplifying gives:

$$X''_N = \sum_{j=1}^{I} \left[\left(\prod_{i=1}^{j} \lambda_i \right) \left(\sum_{i=1}^{j} \frac{\lambda''_i}{\lambda_i} \right) \right] \tag{A.9}$$

and doing the same for equation (A.5) gives:

$$X''_G = \sum_{j=1}^{I} \left[\xi^{j\phi_g} \left(\prod_{i=1}^{j} \lambda_i \right) \left(j\phi_g \xi^{-2}(j\phi_g - 1) + \sum_{i=1}^{j} \frac{2j\phi_g \xi^{-1} \lambda'_i - \lambda''_i}{\lambda_i} \right) \right] \tag{A.10}$$

λ''_i is given by:

$$\begin{aligned} \lambda''_i = \lambda_i \Bigg[& -\frac{\lambda'_i}{\lambda_i} \left((i-1)(\phi_g - 1)\xi^{-1} \right) - (i-1)(\phi_g - 1)\xi^{-2} - \\ & \lambda_i (\phi_g - 1)\xi^{-1} \left(i(\phi_g - 1)\xi^{\phi_g - 2} - \mu_0 (i-1)\xi^{(i-1)(1-\phi_g)} \right) \Bigg] \end{aligned} \tag{A.11}$$

For the double differential of λ_i we get:

$$\lambda''_i = \frac{\lambda''^2_i}{\lambda_i} + \frac{\lambda_i}{\xi - 1} \times \left(\frac{(I-1)(\phi - 1)}{\xi^2} - \frac{\lambda'_i}{\lambda_i} \right) \tag{A.12}$$

We now possess the identities needed to numerically find the optimum bin scaling for a given number of classes. In figure A.1.c the optimum scaling, ξ, is shown as

the solid black line.

B Sensitivity of Diagnosed Mortality Rates to Model Parameters

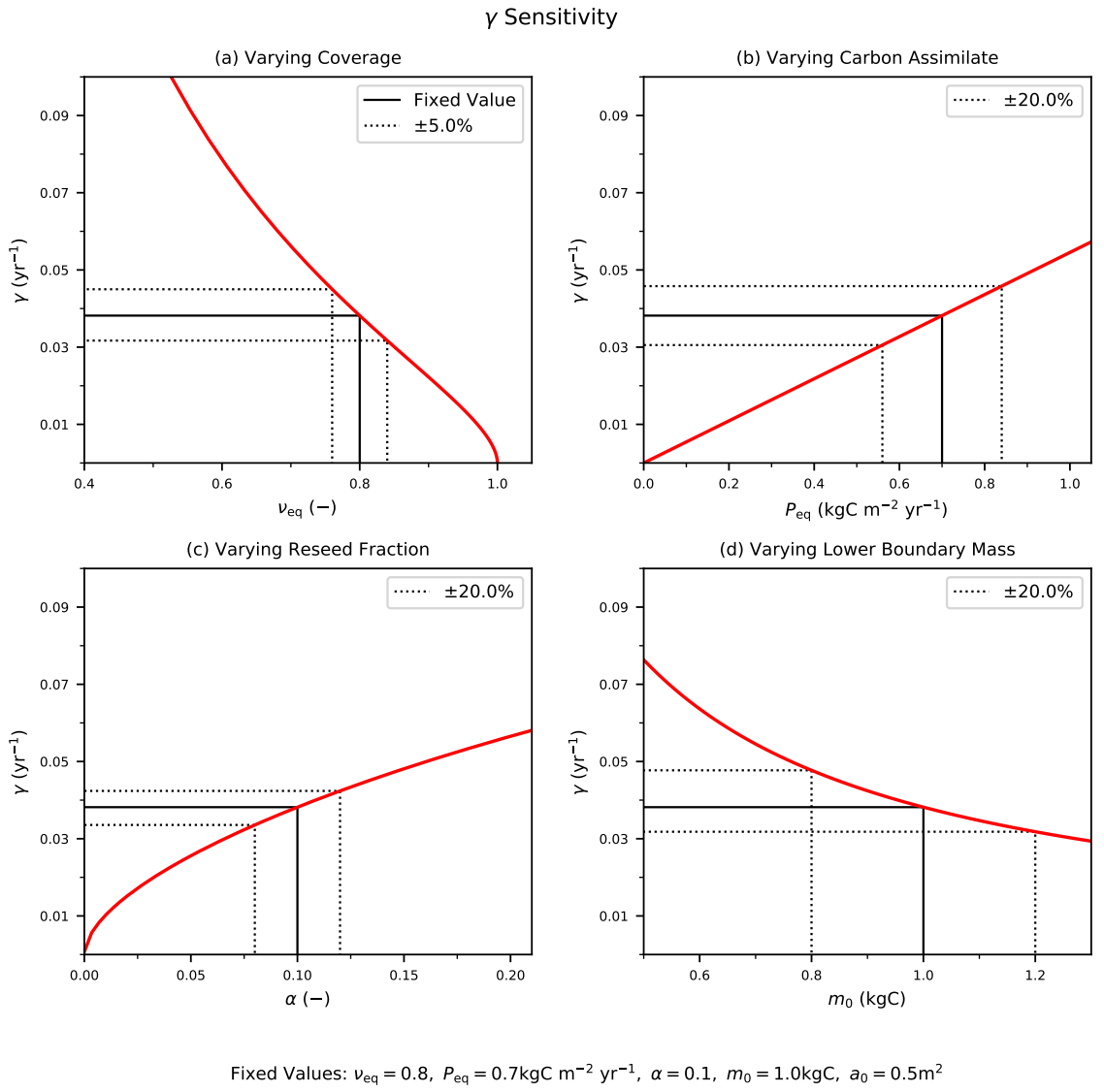

Figure B.1: The sensitivity of the mortality rate to assumed input variables: coverage, ν_{eq} (a), and carbon assimilate rate, P_{eq} (b), and model parameters: reseed fraction, α (c) and boundary mass, m_0 (d). The solid black line indicates the fixed values with corresponding $\pm 20\%$ (b,c,d) or $\pm 5\%$ (a) variation (dotted black lines).

The diagnosed mortality rates in figure 3.6 are sensitive to variation in model inputs and parameters. The mortality rate, γ, can be found for the continuous solutions by rearranging the boundary condition equation (3.11), and substituting

in equation (2.30); $N = n_0 g_0/\gamma$, using equation (2.51) rearrange for N; $N = \nu/(a_0 F_a)$:

$$\gamma = \frac{\alpha P_{\rm eq} a_0}{m_0} \left(\frac{1-\nu_{\rm eq}}{\nu_{\rm eq}} \right) \left[1 + \frac{1}{2\mu_0} + \frac{1}{8\mu_0^2} \right] \tag{B.1}$$

The key external inputs to this equation are the observed PFT fraction ν_{eq} and the net assimilate P_{eq}. In addition, our estimates of γ are dependent on the internal model parameters, α and m_0.

The red lines in figure B.1 demonstrate how the estimate of γ depends on these four inputs. The black dashed lines in figure B.1 indicate how uncertainties in each input relate to uncertainties in γ, for 'true' values typical of a tree PFT. We estimate uncertainties in the observed PFT fraction (e.g. from remote-sensing) to be $\pm 5\%$, and uncertainties in P (e.g. from JULES) to be $\pm 20\%$, leading to errors of $\pm 17\%$ and $\pm 20\%$ respectively. Likewise, $\pm 20\%$ uncertainties in the internal parameters α and m_0 lead to $\pm 12\%$ and $\pm 20\%$ uncertainties in γ. Combining these sources of uncertainty leads to an overall uncertainty in our inferred estimate of γ of about $\pm 35\%$.

Bibliography

Alechin, W. (1946). L'histoire de la phytosociologie russe et ses particularités (Russie). *Outscheny Zapisky Moskowsk. Gosoud. Ouniversit. Wip*, 103:85–95.

Allen, C. D., Macalady, A. K., Chenchouni, H., Bachelet, D., McDowell, N., Vennetier, M., Kitzberger, T., Rigling, A., Breshears, D. D., Hogg, E. T., et al. (2010). A global overview of drought and heat-induced tree mortality reveals emerging climate change risks for forests. *Forest Ecology and Management*, 259(4):660–684.

Alves, L. F. and Santos, F. A. (2002). Tree allometry and crown shape of four tree species in Atlantic rain forest, south-east Brazil. *Journal of Tropical Ecology*, 18(2):245–260.

Anderson-Teixeira, K. J., Wang, M. M., McGarvey, J. C., and LeBauer, D. S. (2016). Carbon dynamics of mature and regrowth tropical forests derived from a pantropical database (TropForC-db). *Global Change Biology*, 22(5):1690–1709.

Antonarakis, A., Munger, J., and Moorcroft, P. (2014). Imaging spectroscopy-and lidar-derived estimates of canopy composition and structure to improve predictions of forest carbon fluxes and ecosystem dynamics. *Geophysical Research Letters*, 41(7):2535–2542.

Argles, A. P. K., Moore, J. R., Huntingford, C., Wiltshire, A. J., Harper, A. B., Jones, C. D., and Cox, P. M. (2020). Robust Ecosystem Demography (RED version 1.0): a parsimonious approach to modelling vegetation dynamics in Earth system models. *Geoscientific Model Development*, 13(9):4067–4089.

Arora, V. K. and Boer, G. J. (2006). Simulating competition and coexistence between plant functional types in a dynamic vegetation model. *Earth Interactions*, 10(10):1–30.

Arora, V. K., Katavouta, A., Williams, R. G., Jones, C. D., Brovkin, V., Friedlingstein, P., Schwinger, J., Bopp, L., Boucher, O., Cadule, P., et al. (2020). Carbon–concentration and carbon–climate feedbacks in CMIP6 models and their comparison to CMIP5 models. *Biogeosciences*, 17(16):4173–4222.

Asner, G. P., Kellner, J. R., Kennedy-Bowdoin, T., Knapp, D. E., Anderson, C., and Martin, R. E. (2013). Forest canopy gap distributions in the southern Peruvian Amazon. *PLOS One*, 8(4):e60875.

Bailey, R. L. and Dell, T. (1973). Quantifying diameter distributions with the Weibull function. *Forest Science*, 19(2):97–104.

Baker, T. R., Swaine, M. D., and Burslem, D. F. (2003). Variation in tropical forest growth rates: combined effects of functional group composition and resource availability. *Perspectives in Plant Ecology, Evolution and Systematics*, 6(1-2):21–36.

Bateman, I., Morison, J., Brazier, R., Binner, A., Betts, R., Hails, R., Hastings, A., Day, B., Anderson, K., Williamson, D., Tyler, C., Unger, N., Belcher, C., Matthews, R., Heard, M., Cox, P., Hill, T., Harper, A., and Sabrina, E. (2021). Greenhouse Gas Removal Plus (GGR+): Sustainable Treescapes Demonstrator and Decision Tools. UK Research and Innovation. Project Reference: BB/V011588/1.

Bayer, A. D., Lindeskog, M., Pugh, T. A., Anthoni, P. M., Fuchs, R., and Arneth, A. (2017). Uncertainties in the land-use flux resulting from land-use change reconstructions and gross land transitions. *Earth System Dynamics*, 8(1):91–111.

Beckman, N. G., Bullock, J. M., and Salguero-Gómez, R. (2018). High dispersal ability is related to fast life-history strategies. *Journal of Ecology*, 106(4):1349–1362.

Beer, C., Lucht, W., Gerten, D., Thonicke, K., and Schmullius, C. (2007). Effects of soil freezing and thawing on vegetation carbon density in Siberia: A modeling

analysis with the Lund-Potsdam-Jena Dynamic Global Vegetation Model (LPJ-DGVM). *Global Biogeochemical Cycles*, 21(1).

Bellard, C., Bertelsmeier, C., Leadley, P., Thuiller, W., and Courchamp, F. (2012). Impacts of climate change on the future of biodiversity. *Ecology Letters*, 15(4):365–377.

Belsky, A. J. and Canham, C. D. (1994). Forest gaps and isolated savanna trees. *Bioscience*, 44(2):77–84.

Betts, R., Cox, P., Collins, M., Harris, P., Huntingford, C., and Jones, C. (2004). The role of ecosystem-atmosphere interactions in simulated Amazonian precipitation decrease and forest dieback under global climate warming. *Theoretical and Applied Climatology*, 78(1):157–175.

Bohn, K., Dyke, J., Pavlick, R., Reineking, B., Reu, B., and Kleidon, A. (2011). The relative importance of seed competition, resource competition and perturbations on community structure. *Biogeosciences*, 8(5):1107–1120.

Bond, B. J., Meinzer, F. C., and Brooks, J. R. (2008). *How trees influence the hydrological cycle in forest ecosystems*. John Wiley & Sons Ltd: Hoboken, NJ.

Bond-Lamberty, B., Wang, C., Gower, S., and Norman, J. (2002). Leaf area dynamics of a boreal black spruce fire chronosequence. *Tree Physiology*, 22(14):993–1001.

Botkin, D. B., Janak, J. F., and Wallis, J. R. (1972a). Rationale, limitations, and assumptions of a northeastern forest growth simulator. *IBM Journal of Research and Development*, 16(2):101–116.

Botkin, D. B., Janak, J. F., and Wallis, J. R. (1972b). Some ecological consequences of a computer model of forest growth. *The Journal of Ecology*, 60(3):849–872.

Boulangeat, I., Philippe, P., Abdulhak, S., Douzet, R., Garraud, L., Lavergne, S., Lavorel, S., Van Es, J., Vittoz, P., and Thuiller, W. (2012). Improving plant functional groups for dynamic models of biodiversity: at the crossroads between functional and community ecology. *Global Change Biology*, 18(11):3464–3475.

Brando, P. M., Balch, J. K., Nepstad, D. C., Morton, D. C., Putz, F. E., Coe, M. T., Silvério, D., Macedo, M. N., Davidson, E. A., Nóbrega, C. C., et al. (2014). Abrupt increases in Amazonian tree mortality due to drought–fire interactions. *Proceedings of the National Academy of Sciences*, 111(17):6347–6352.

Brando, P. M., Nepstad, D. C., Balch, J. K., Bolker, B., Christman, M. C., Coe, M., and Putz, F. E. (2012). Fire-induced tree mortality in a neotropical forest: the roles of bark traits, tree size, wood density and fire behavior. *Global Change Biology*, 18(2):630–641.

Braun-Blanquet, J. et al. (1932). Plant sociology. The study of plant communities. *Plant Sociology. the Study of Plant Communities. First Ed.*

Brook, B. W., Sodhi, N. S., and Ng, P. K. (2003). Catastrophic extinctions follow deforestation in Singapore. *Nature*, 424(6947):420–423.

Brovkin, V., Ganopolski, A., and Svirezhev, Y. (1997). A continuous climate-vegetation classification for use in climate-biosphere studies. *Ecological Modelling*, 101(2-3):251–261.

Bugmann, H. (2001). A review of forest gap models. *Climatic Change*, 51(3):259–305.

Bugmann, H. and Bigler, C. (2011). Will the CO_2 fertilization effect in forests be offset by reduced tree longevity? *Oecologia*, 165(2):533–544.

Burton, C., Betts, R., Cardoso, M., Feldpausch, T. R., Harper, A., Jones, C. D., Kelley, D. I., Robertson, E., and Wiltshire, A. (2019). Representation of fire, land-use change and vegetation dynamics in the Joint UK Land Environment Simulator vn4. 9 (JULES). *Geoscientific Model Development*, 12(1):179–193.

Calle, L. and Poulter, B. (2021). Ecosystem age-class dynamics and distribution in the LPJ-wsl v2. 0 global ecosystem model. *Geoscientific Model Development*, 14(5):2575–2601.

Canham, C. D., Finzi, A. C., Pacala, S. W., and Burbank, D. H. (1994). Causes and consequences of resource heterogeneity in forests: interspecific variation in light transmission by canopy trees. *Canadian Journal of Forest Research*, 24(2):337–349.

Carvalhais, N., Forkel, M., Khomik, M., Bellarby, J., Jung, M., Migliavacca, M., Saatchi, S., Santoro, M., Thurner, M., Weber, U., et al. (2014). Global covariation of carbon turnover times with climate in terrestrial ecosystems. *Nature*, 514(7521):213–217.

Chambers, J. Q., Negron-Juarez, R. I., Marra, D. M., Di Vittorio, A., Tews, J., Roberts, D., Ribeiro, G. H., Trumbore, S. E., and Higuchi, N. (2013). The steady-state mosaic of disturbance and succession across an old-growth Central Amazon forest landscape. *Proceedings of the National Academy of Sciences*, 110(10):3949–3954.

Chaturvedi, R., Raghubanshi, A., and Singh, J. (2012). Effect of grazing and harvesting on diversity, recruitment and carbon accumulation of juvenile trees in tropical dry forests. *Forest Ecology and Management*, 284:152–162.

Chave, J., Andalo, C., Brown, S., Cairns, M. A., Chambers, J. Q., Eamus, D., Fölster, H., Fromard, F., Higuchi, N., Kira, T., et al. (2005). Tree allometry and improved estimation of carbon stocks and balance in tropical forests. *Oecologia*, 145(1):87–99.

Chave, J., Réjou-Méchain, M., Búrquez, A., Chidumayo, E., Colgan, M. S., Delitti, W. B., Duque, A., Eid, T., Fearnside, P. M., Goodman, R. C., et al. (2014). Improved allometric models to estimate the aboveground biomass of tropical trees. *Global Change Biology*, 20(10):3177–3190.

Chuvieco, E., Pettinari, M., Lizundia Loiola, J., Storm, T., and Padilla Parellada, M. (2019). ESA Fire Climate Change Initiative (FIRE_CCI): MODIS FIRE_CCI Burned Area Grid product, version 5.1. doi:10.5285/3628cb2fdba443588155e15dee8e5352.

Clark, J. S. (1988). Effect of climate change on fire regimes in northwestern Minnesota. *Nature*, 334(6179):233–235.

Clark, J. S. (1990). Fire and climate change during the last 750 yr in northwestern Minnesota. *Ecological Monographs*, 60(2):135–159.

Clements, F. E. (1916). *Plant succession: an analysis of the development of vegetation*. Number 242. Carnegie Institution of Washington.

Coomes, D. A. and Allen, R. B. (2007). Mortality and tree-size distributions in natural mixed-age forests. *Journal of Ecology*, 95(1):27–40.

Coomes, D. A., Duncan, R. P., Allen, R. B., and Truscott, J. (2003). Disturbances prevent stem size-density distributions in natural forests from following scaling relationships. *Ecology Letters*, 6(11):980–989.

Coomes, D. A., Lines, E. R., and Allen, R. B. (2011). Moving on from Metabolic Scaling Theory: hierarchical models of tree growth and asymmetric competition for light. *Journal of Ecology*, 99(3):748–756.

Coutinho, L. M. (1990). Fire in the ecology of the Brazilian cerrado. In *Fire in the tropical biota*, pages 82–105. Springer.

Cox, P., Huntingford, C., and Harding, R. (1998). A canopy conductance and photosynthesis model for use in a GCM land surface scheme. *Journal of Hydrology*, 212:79–94.

Cox, P. M. (2001). Description of the "TRIFFID" dynamic global vegetation model. Technical Report 24, Met Office.

Cox, P. M., Betts, R., Collins, M., Harris, P. P., Huntingford, C., and Jones, C. (2004). Amazonian forest dieback under climate-carbon cycle projections for the 21st century. *Theoretical and Applied Climatology*, 78(1):137–156.

Cox, P. M., Betts, R. A., Jones, C. D., Spall, S. A., and Totterdell, I. J. (2000). Acceleration of global warming due to carbon-cycle feedbacks in a coupled climate model. *Nature*, 408(6809):184–187.

Cramer, W., Bondeau, A., Woodward, F. I., Prentice, I. C., Betts, R. A., Brovkin, V., Cox, P. M., Fisher, V., Foley, J. A., Friend, A. D., et al. (2001). Global response of terrestrial ecosystem structure and function to CO2 and climate change: results from six dynamic global vegetation models. *Global Change Biology*, 7(4):357–373.

Cunha, A. P. M., Alvalá, R. C., Sampaio, G., Shimizu, M. H., and Costa, M. H. (2013). Calibration and validation of the integrated biosphere simulator (IBIS) for a Brazilian semiarid region. *Journal of Applied Meteorology and Climatology*, 52(12):2753–2770.

Curran, L. M., Trigg, S. N., McDonald, A. K., Astiani, D., Hardiono, Y., Siregar, P., Caniago, I., and Kasischke, E. (2004). Lowland forest loss in protected areas of Indonesian Borneo. *Science*, 303(5660):1000–1003.

Curtis, J. T. and McIntosh, R. P. (1951). An upland forest continuum in the prairie-forest border region of Wisconsin. *Ecology*, 32(3):476–496.

da Costa, A. C. L., Galbraith, D., Almeida, S., Portela, B. T. T., da Costa, M., Junior, J. d. A. S., Braga, A. P., de Gonçalves, P. H., de Oliveira, A. A., Fisher, R., et al. (2010). Effect of 7 yr of experimental drought on vegetation dynamics and biomass storage of an eastern Amazonian rainforest. *New Phytologist*, 187(3):579–591.

Da Silveira Lobo Sternberg, L. (2001). Savanna–forest hysteresis in the tropics. *Global Ecology and Biogeography*, 10(4):369–378.

Dai, A., Trenberth, K. E., and Qian, T. (2004). A global dataset of Palmer Drought Severity Index for 1870–2002: Relationship with soil moisture and effects of surface warming. *Journal of Hydrometeorology*, 5(6):1117–1130.

Dale, V. H., Doyle, T. W., and Shugart, H. H. (1985). A comparison of tree growth models. *Ecological Modelling*, 29(1-4):145–169.

Dale, V. H., Joyce, L. A., McNulty, S., Neilson, R. P., Ayres, M. P., Flannigan, M. D., Hanson, P. J., Irland, L. C., Lugo, A. E., Peterson, C. J., et al. (2001). Climate change and forest disturbances: climate change can affect forests by altering the frequency, intensity, duration, and timing of fire, drought, introduced species, insect and pathogen outbreaks, hurricanes, windstorms, ice storms, or landslides. *Bioscience*, 51(9):723–734.

Daly, C., Bachelet, D., Lenihan, J. M., Neilson, R. P., Parton, W., and Ojima, D. (2000). Dynamic simulation of tree–grass interactions for global change studies. *Ecological Applications*, 10(2):449–469.

Dashti, H., Pandit, K., Glenn, N. F., Shinneman, D. J., Flerchinger, G. N., Hudak, A. T., de Graaf, M. A., Flores, A., Ustin, S., Ilangakoon, N., et al. (2021). Performance of the ecosystem demography model (EDv2. 2) in simulating gross primary production capacity and activity in a dryland study area. *Agricultural and Forest Meteorology*, 297:108270.

de L. Dantas, V., Batalha, M. A., and Pausas, J. G. (2013). Fire drives functional thresholds on the savanna–forest transition. *Ecology*, 94(11):2454–2463.

Dewar, R. C. (1993). A mechanistic analysis of self-thinning in terms of the carbon balance of trees. *Annals of Botany*, 71(2):147–159.

Díaz, S. and Cabido, M. (2001). Vive la différence: plant functional diversity matters to ecosystem processes. *Trends in Ecology & Evolution*, 16(11):646–655.

Dickinson, R. E. (1984). Modeling evapotranspiration for three-dimensional global climate models. *Climate Processes and Climate Sensitivity*, 29:58–72.

Dorfman, R. (1979). A formula for the Gini coefficient. *The Review of Economics and Statistics*, 61(1):146–149.

Dorman, J. and Sellers, P. J. (1989). A global climatology of albedo, roughness length and stomatal resistance for atmospheric general circulation models as represented by the simple biosphere model (SiB). *Journal of Applied Meteorology and Climatology*, 28(9):833–855.

Dorrough, J. and Moxham, C. (2005). Eucalypt establishment in agricultural landscapes and implications for landscape-scale restoration. *Biological Conservation*, 123(1):55–66.

Doughty, C. E., Metcalfe, D., Girardin, C., Amezquita, F. F., Cabrera, D. G., Huasco, W. H., Silva-Espejo, J., Araujo-Murakami, A., Da Costa, M., Rocha, W., et al. (2015). Drought impact on forest carbon dynamics and fluxes in Amazonia. *Nature*, 519(7541):78–82.

Doyle, T. W. (1981). The role of disturbance in the gap dynamics of a montane rain forest: an application of a tropical forest succession model. In *Forest succession*, pages 56–73. Springer.

Drew, T. J. and Flewelling, J. W. (1977). Some recent Japanese theories of yield-density relationships and their application to Monterey pine plantations. *Forest Science*, 23(4):517–534.

Drijfhout, S., Bathiany, S., Beaulieu, C., Brovkin, V., Claussen, M., Huntingford, C., Scheffer, M., Sgubin, G., and Swingedouw, D. (2015). Catalogue of abrupt

shifts in Intergovernmental Panel on Climate Change climate models. *Proceedings of the National Academy of Sciences*, 112(43):E5777–E5786.

Eamus, D. and Jarvis, P. G. (1989). The direct effects of increase in the global atmospheric CO2 concentration on natural and commercial temperate trees and forests. *Advances in Ecological Research*, 19:1–55.

Eller, C. B., Rowland, L., Mencuccini, M., Rosas, T., Williams, K., Harper, A., Medlyn, B. E., Wagner, Y., Klein, T., Teodoro, G. S., et al. (2020). Stomatal optimization based on xylem hydraulics (SOX) improves land surface model simulation of vegetation responses to climate. *New Phytologist*, 226(6):1622–1637.

Eller, C. B., Rowland, L., Oliveira, R. S., Bittencourt, P. R., Barros, F. V., da Costa, A. C., Meir, P., Friend, A. D., Mencuccini, M., Sitch, S., et al. (2018). Modelling tropical forest responses to drought and El Niño with a stomatal optimization model based on xylem hydraulics. *Philosophical Transactions of the Royal Society B: Biological Sciences*, 373(1760):20170315.

Enquist, B. J., Brown, J. H., and West, G. B. (1998). Allometric scaling of plant energetics and population density. *Nature*, 395(6698):163–165.

Enquist, B. J., West, G. B., and Brown, J. H. (2009). Extensions and evaluations of a general quantitative theory of forest structure and dynamics. *Proceedings of the National Academy of Sciences*, 106(17):7046–7051.

Enright, N. J., Fontaine, J. B., Lamont, B. B., Miller, B. P., and Westcott, V. C. (2014). Resistance and resilience to changing climate and fire regime depend on plant functional traits. *Journal of Ecology*, 102(6):1572–1581.

Erb, K.-H., Fetzel, T., Plutzar, C., Kastner, T., Lauk, C., Mayer, A., Niedertscheider, M., Körner, C., and Haberl, H. (2016). Biomass turnover time in terrestrial ecosystems halved by land use. *Nature Geoscience*, 9(9):674–678.

Espírito-Santo, F. D., Gloor, M., Keller, M., Malhi, Y., Saatchi, S., Nelson, B., Junior, R. C. O., Pereira, C., Lloyd, J., Frolking, S., et al. (2014). Size and frequency of natural forest disturbances and the Amazon forest carbon balance. *Nature Communications*, 5(1):1–6.

Esseen, P.-A. (1994). Tree mortality patterns after experimental fragmentation of an old-growth conifer forest. *Biological Conservation*, 68(1):19–28.

Fahrig, L. (2002). Effect of habitat fragmentation on the extinction threshold: a synthesis. *Ecological Applications*, 12(2):346–353.

Fauset, S., Baker, T. R., Lewis, S. L., Feldpausch, T. R., Affum-Baffoe, K., Foli, E. G., Hamer, K. C., and Swaine, M. D. (2012). Drought-induced shifts in the floristic and functional composition of tropical forests in Ghana. *Ecology Letters*, 15(10):1120–1129.

Fauset, S., Gloor, M., Fyllas, N. M., Phillips, O. L., Asner, G. P., Baker, T. R., Patrick Bentley, L., Brienen, R. J., Christoffersen, B. O., del Aguila-Pasquel, J., et al. (2019). Individual-based modeling of Amazon forests suggests that climate controls productivity while traits control demography. *Frontiers in Earth Science*, 7:83.

Feeley, K. J., Davies, S. J., Perez, R., Hubbell, S. P., and Foster, R. B. (2011). Directional changes in the species composition of a tropical forest. *Ecology*, 92(4):871–882.

Feldpausch, T. R., Banin, L., Phillips, O. L., Baker, T. R., Lewis, S. L., Quesada, C. A., Affum-Baffoe, K., Arets, E. J., Berry, N. J., Bird, M., et al. (2011). Height-diameter allometry of tropical forest trees. *Biogeosciences*, 8(5):1081–1106.

Feldpausch, T. R., Lloyd, J., Lewis, S. L., Brienen, R. J., Gloor, M., Monteagudo Mendoza, A., Lopez-Gonzalez, G., Banin, L., Abu Salim, K., Affum-Baffoe, K., et al. (2012). Tree height integrated into pantropical forest biomass estimates. *Biogeosciences*, 9(8):3381–3403.

Fischer, R., Bohn, F., de Paula, M. D., Dislich, C., Groeneveld, J., Gutiérrez, A. G., Kazmierczak, M., Knapp, N., Lehmann, S., Paulick, S., et al. (2016). Lessons learned from applying a forest gap model to understand ecosystem and carbon dynamics of complex tropical forests. *Ecological Modelling*, 326:124–133.

Fisher, J. I., Hurtt, G. C., Thomas, R. Q., and Chambers, J. Q. (2008). Clustered disturbances lead to bias in large-scale estimates based on forest sample plots. *Ecology Letters*, 11(6):554–563.

Fisher, R., McDowell, N., Purves, D., Moorcroft, P., Sitch, S., Cox, P., Huntingford, C., Meir, P., and Woodward, F. I. (2010). Assessing uncertainties in a second-generation dynamic vegetation model caused by ecological scale limitations. *New Phytologist*, 187(3):666–681.

Fisher, R. A., Koven, C. D., Anderegg, W. R., Christoffersen, B. O., Dietze, M. C., Farrior, C. E., Holm, J. A., Hurtt, G. C., Knox, R. G., Lawrence, P. J., et al. (2018). Vegetation demographics in Earth System Models: A review of progress and priorities. *Global Change Biology*, 24(1):35–54.

Fisher, R. A., Muszala, S., Verteinstein, M., Lawrence, P., Xu, C., McDowell, N. G., Knox, R. G., Koven, C., Holm, J., Rogers, B. M., et al. (2015). Taking off the training wheels: the properties of a dynamic vegetation model without climate envelopes, CLM4. 5 (ED). *Geoscientific Model Development*, 8(11):3593–3619.

Foley, J. A., Prentice, I. C., Ramankutty, N., Levis, S., Pollard, D., Sitch, S., and Haxeltine, A. (1996). An integrated biosphere model of land surface processes, terrestrial carbon balance, and vegetation dynamics. *Global Biogeochemical Cycles*, 10(4):603–628.

Forkel, M., Drüke, M., Thurner, M., Dorigo, W., Schaphoff, S., Thonicke, K., von Bloh, W., and Carvalhais, N. (2019). Constraining modelled global vegetation dynamics and carbon turnover using multiple satellite observations. *Scientific Reports*, 9(1):1–12.

Franklin, J. F. and Van Pelt, R. (2004). Spatial aspects of structural complexity in old-growth forests. *Journal of Forestry*, 102(3):22–28.

Franklin, O., Harrison, S. P., Dewar, R., Farrior, C. E., Brännström, Å., Dieckmann, U., Pietsch, S., Falster, D., Cramer, W., Loreau, M., et al. (2020). Organizing principles for vegetation dynamics. *Nature Plants*, 6(5):444–453.

Freedman, H. I. (1980). *Deterministic mathematical models in population ecology*, volume 57. Marcel Dekker Incorporated.

Friedlingstein, P., Bopp, L., Ciais, P., Dufresne, J.-L., Fairhead, L., LeTreut, H., Monfray, P., and Orr, J. (2001). Positive feedback between future climate

change and the carbon cycle. *Geophysical Research Letters*, 28(8):1543–1546.

Friedlingstein, P., Meinshausen, M., Arora, V. K., Jones, C. D., Anav, A., Liddicoat, S. K., and Knutti, R. (2014). Uncertainties in CMIP5 climate projections due to carbon cycle feedbacks. *Journal of Climate*, 27(2):511–526.

Friedlingstein, P., O'Sullivan, M., Jones, M. W., Andrew, R. M., Hauck, J., Olsen, A., Peters, G. P., Peters, W., Pongratz, J., Sitch, S., et al. (2020). Global carbon budget 2020. *Earth System Science Data*, 12(4):3269–3340.

Friend, A., Schugart, H., and Running, S. W. (1993). A physiology-based gap model of forest dynamics. *Ecology*, 74(3):792–797.

Friend, A., Stevens, A., Knox, R., and Cannell, M. (1997). A process-based, terrestrial biosphere model of ecosystem dynamics (Hybrid v3. 0). *Ecological Modelling*, 95(2-3):249–287.

Friend, A. D., Lucht, W., Rademacher, T. T., Keribin, R., Betts, R., Cadule, P., Ciais, P., Clark, D. B., Dankers, R., Falloon, P. D., et al. (2014). Carbon residence time dominates uncertainty in terrestrial vegetation responses to future climate and atmospheric CO2. *Proceedings of the National Academy of Sciences*, 111(9):3280–3285.

Friend, A. D. and White, A. (2000). Evaluation and analysis of a dynamic terrestrial ecosystem model under preindustrial conditions at the global scale. *Global Biogeochemical Cycles*, 14(4):1173–1190.

Fyllas, N. M., Gloor, E., Mercado, L., Sitch, S., Quesada, C. A., Domingues, T., Galbraith, D., Torre-Lezama, A., Vilanova, E., Ramírez-Angulo, H., et al. (2014). Analysing Amazonian forest productivity using a new individual and trait-based model (TFS v. 1). *Geoscientific Model Development*, 7(4):1251–1269.

Gasser, T., Crepin, L., Quilcaille, Y., Houghton, R. A., Ciais, P., and Obersteiner, M. (2020). Historical CO 2 emissions from land use and land cover change and their uncertainty. *Biogeosciences*, 17(15):4075–4101.

Gaudel, R. et al. (2019). Canopy gap characteristics, their size-distribution and spatial pattern in a mountainous cool temperate forest of Japan.

Gifford, R. M. (1993). Implications of CO 2 effects on vegetation for the global carbon budget. In *The global carbon cycle*, pages 159–199. Springer.

Gleason, H. A. (1926). The individualistic concept of the plant association. *Bulletin of the Torrey Botanical Club*, 53(1):7–26.

Goodbody, T. R., Tompalski, P., Coops, N. C., White, J. C., Wulder, M. A., and Sanelli, M. (2020). Uncovering spatial and ecological variability in gap size frequency distributions in the Canadian boreal forest. *Scientific Reports*, 10(1):1–12.

Gora, E. M. and Esquivel-Muelbert, A. (2021). Implications of size-dependent tree mortality for tropical forest carbon dynamics. *Nature Plants*, 7(4):384–391.

Grime, J. (1998). Benefits of plant diversity to ecosystems: immediate, filter and founder effects. *Journal of Ecology*, 86(6):902–910.

Gustafson, E. J. (2013). When relationships estimated in the past cannot be used to predict the future: using mechanistic models to predict landscape ecological dynamics in a changing world. *Landscape Ecology*, 28(8):1429–1437.

Haddad, N. M., Brudvig, L. A., Clobert, J., Davies, K. F., Gonzalez, A., Holt, R. D., Lovejoy, T. E., Sexton, J. O., Austin, M. P., Collins, C. D., et al. (2015). Habitat fragmentation and its lasting impact on Earth's ecosystems. *Science Advances*, 1(2):e1500052.

Hallé, F., Oldeman, R. A., and Tomlinson, P. B. (2012). *Tropical trees and forests: an architectural analysis*. Springer Science & Business Media.

Hansen, M. and Song, X. (2018). Vegetation Continuous Fields (VCF) Yearly Global 0.05 Deg. *NASA EOSDIS Land Processes DAAC*, 645.

Hansen, M. C., Potapov, P. V., Moore, R., Hancher, M., Turubanova, S. A., Tyukavina, A., Thau, D., Stehman, S., Goetz, S. J., Loveland, T. R., et al. (2013). High-resolution global maps of 21st-century forest cover change. *Science*, 342(6160):850–853.

Harding, D., Lefsky, M., Parker, G., and Blair, J. (2001). Laser altimeter canopy height profiles: Methods and validation for closed-canopy, broadleaf forests. *Remote Sensing of Environment*, 76(3):283–297.

Harper, A. B., Cox, P. M., Friedlingstein, P., Wiltshire, A. J., Jones, C. D., Sitch, S., Mercado, L. M., Groenendijk, M., Robertson, E., Kattge, J., et al. (2016). Improved representation of plant functional types and physiology in the Joint UK Land Environment Simulator (JULES v4. 2) using plant trait information. *Geoscientific Model Development*, 9(7):2415–2440.

Harper, A. B., Powell, T., Cox, P. M., House, J., Huntingford, C., Lenton, T. M., Sitch, S., Burke, E., Chadburn, S. E., Collins, W. J., et al. (2018). Land-use emissions play a critical role in land-based mitigation for Paris climate targets. *Nature Communications*, 9(1):1–13.

Harte, J. (2011). *Maximum entropy and ecology: a theory of abundance, distribution, and energetics*. OUP Oxford.

Haverd, V., Smith, B., Nieradzik, L., Briggs, P. R., Woodgate, W., Trudinger, C. M., Canadell, J. G., and Cuntz, M. (2018). A new version of the CABLE land surface model (Subversion revision r4601) incorporating land use and land cover change, woody vegetation demography, and a novel optimisation-based approach to plant coordination of photosynthesis. *Geoscientific Model Development*, 11(7):2995–3026.

Haverd, V., Smith, B., Nieradzik, L. P., and Briggs, P. R. (2014). A stand-alone tree demography and landscape structure module for Earth system models: integration with inventory data from temperate and boreal forests. *Biogeosciences*, 11(15):4039–4055.

Haxeltine, A. and Prentice, I. (1996). A general model for the light-use efficiency of primary production. *Functional Ecology*, 10(5):551–561.

Heinrich, V. H., Dalagnol, R., Cassol, H. L., Rosan, T. M., de Almeida, C. T., Junior, C. H. S., Campanharo, W. A., House, J. I., Sitch, S., Hales, T. C., et al. (2021). Large carbon sink potential of secondary forests in the Brazilian Amazon to mitigate climate change. *Nature Communications*, 12(1):1–11.

Higgins, S. I., Scheiter, S., and Sankaran, M. (2010). The stability of African savannas: insights from the indirect estimation of the parameters of a dynamic model. *Ecology*, 91(6):1682–1692.

Higuchi, P., Oliveira-Filho, A. T., Bebber, D. P., Brown, N. D., Silva, A. C., and Machado, E. L. (2008). Spatio-temporal patterns of tree community dynamics in a tropical forest fragment in South-east Brazil. *Plant Ecology*, 199(1):125–135.

Hirose, T. (2005). Development of the Monsi–Saeki theory on canopy structure and function. *Annals of Botany*, 95(3):483–494.

Holdridge, L. R. (1947). Determination of world plant formations from simple climatic data. *Science*, 105(2727):367–368.

Honnay, O., Verheyen, K., Butaye, J., Jacquemyn, H., Bossuyt, B., and Hermy, M. (2002). Possible effects of habitat fragmentation and climate change on the range of forest plant species. *Ecology Letters*, 5(4):525–530.

Houghton, R. A. (2005). Tropical deforestation as a source of greenhouse gas emissions. *Tropical Deforestation and Climate Change*, 13.

Hurtt, G. C., Dubayah, R., Drake, J., Moorcroft, P. R., Pacala, S. W., Blair, J. B., and Fearon, M. G. (2004). Beyond potential vegetation: Combining lidar data and a height-structured model for carbon studies. *Ecological Applications*, 14(3):873–883.

Igea, J., Miller, E. F., Papadopulos, A. S., and Tanentzap, A. J. (2017). Seed size and its rate of evolution correlate with species diversification across angiosperms. *PLoS Biology*, 15(7):e2002792.

Iida, Y., Kohyama, T. S., Swenson, N. G., Su, S.-H., Chen, C.-T., Chiang, J.-M., and Sun, I.-F. (2014). Linking functional traits and demographic rates in a subtropical tree community: the importance of size dependency. *Journal of Ecology*, 102(3):641–650.

Jain, A. K., Meiyappan, P., Song, Y., and House, J. I. (2013). CO2 emissions from land-use change affected more by nitrogen cycle, than by the choice of land-cover data. *Global Change Biology*, 19(9):2893–2906.

Jenkins, T. A., Mackie, E. D., Matthews, R. W., Miller, G., Randle, T. J., and White, M. E. (2011). FC woodland carbon code: Carbon assessment protocol. *Forestry Commission, Edinburgh*.

Jennings, S., Brown, N., and Sheil, D. (1999). Assessing forest canopies and understorey illumination: canopy closure, canopy cover and other measures. *Forestry: an International Journal of Forest Research*, 72(1):59–74.

Johnson, M. O., Galbraith, D., Gloor, M., De Deurwaerder, H., Guimberteau, M., Rammig, A., Thonicke, K., Verbeeck, H., Von Randow, C., Monteagudo, A., et al. (2016). Variation in stem mortality rates determines patterns of above-ground biomass in A mazonian forests: implications for dynamic global vegetation models. *Global Change Biology*, 22(12):3996–4013.

Jones, S., Rowland, L., Cox, P., Hemming, D., Wiltshire, A., Williams, K., Parazoo, N. C., Liu, J., da Costa, A. C., Meir, P., et al. (2020). The impact of a simple representation of non-structural carbohydrates on the simulated response of tropical forests to drought. *Biogeosciences*, 17(13):3589–3612.

Jönsson, M. T., Fraver, S., Jonsson, B. G., Dynesius, M., Rydgård, M., and Esseen, P.-A. (2007). Eighteen years of tree mortality and structural change in an experimentally fragmented Norway spruce forest. *Forest Ecology and Management*, 242(2-3):306–313.

Kadavỳ, J., Kneifl, M., Fedorová, B., and Bartuněk, J. (2017). Evaluation of transformation from even-aged to selection forest by means of Gini index. *Journal of Forest Science*, 63(10):476–484.

Kane, V. R., Gersonde, R. F., Lutz, J. A., McGaughey, R. J., Bakker, J. D., and Franklin, J. F. (2011). Patch dynamics and the development of structural and spatial heterogeneity in Pacific Northwest forests. *Canadian Journal of Forest Research*, 41(12):2276–2291.

Kato, E., Kinoshita, T., Ito, A., Kawamiya, M., and Yamagata, Y. (2013). Evaluation of spatially explicit emission scenario of land-use change and biomass burning using a process-based biogeochemical model. *Journal of Land Use Science*, 8(1):104–122.

Kattge, J., Diaz, S., Lavorel, S., Prentice, I. C., Leadley, P., Bönisch, G., Garnier, E., Westoby, M., Reich, P. B., Wright, I. J., et al. (2011). TRY–a global database of plant traits. *Global Change Biology*, 17(9):2905–2935.

Kelley, D., Betts, N., Burton, C., Oliver, R., Argles, A., Williams, K., Jones, C., Blyth, E., Adzhar, R., Gerard, F., Guangqi, L., Mercado, L., and Clark, D. (2021). The Virtual Trees of UKESM Improving Our Simulations. https://ukesm.ac.uk/portfolio-item/virtual-trees-of-ukesm-improving-our-simulations/. Accessed: 2021-06-30.

Kinnaird, M. F. and O'Brien, T. G. (1998). Ecological effects of wildfire on lowland rainforest in Sumatra. *Conservation Biology*, 12(5):954–956.

Kinzig, A. P., Ryan, P., Etienne, M., Allison, H., Elmqvist, T., and Walker, B. H. (2006). Resilience and regime shifts: assessing cascading effects. *Ecology and Society*, 11(1).

Kleidon, A. and Mooney, H. A. (2000). A global distribution of biodiversity inferred from climatic constraints: results from a process-based modelling study. *Global Change Biology*, 6(5):507–523.

Kohyama, T., Suzuki, E., Partomihardjo, T., Yamada, T., and Kubo, T. (2003). Tree species differentiation in growth, recruitment and allometry in relation to maximum height in a Bornean mixed dipterocarp forest. *Journal of Ecology*, 91(5):797–806.

Koppen, W. d. (1936). Das geographische system der klimat. *Handbuch Der Klimatologie*, Band I, Teil C.:46.

Koven, C., Chambers, J., Georgiou, K., Knox, R., Negron-Juarez, R., Riley, W., Arora, V., Brovkin, V., Friedlingstein, P., and Jones, C. (2015). Controls on terrestrial carbon feedbacks by productivity versus turnover in the CMIP5 Earth System Models. *Biogeosciences*, 12(17):5211–5228.

Krause, A., Pugh, T. A., Bayer, A. D., Li, W., Leung, F., Bondeau, A., Doelman, J. C., Humpenöder, F., Anthoni, P., Bodirsky, B. L., et al. (2018). Large uncertainty in carbon uptake potential of land-based climate-change mitigation efforts. *Global Change Biology*, 24(7):3025–3038.

Kucharik, C. J., Barford, C. C., El Maayar, M., Wofsy, S. C., Monson, R. K., and Baldocchi, D. D. (2006). A multiyear evaluation of a Dynamic Global Vegetation Model at three AmeriFlux forest sites: Vegetation structure, phenology, soil

temperature, and CO_2 and H_2O vapor exchange. *Ecological Modelling*, 196(1-2):1–31.

Laurance, W. F., Ferreira, L. V., Rankin-de Merona, J. M., and Laurance, S. G. (1998). Rain forest fragmentation and the dynamics of Amazonian tree communities. *Ecology*, 79(6):2032–2040.

Laurance, W. F. and Williamson, G. B. (2001). Positive feedbacks among forest fragmentation, drought, and climate change in the Amazon. *Conservation Biology*, 15(6):1529–1535.

Lavorel, S. and Garnier, E. (2002). Predicting changes in community composition and ecosystem functioning from plant traits: revisiting the Holy Grail. *Functional Ecology*, 16(5):545–556.

Leemans, R. and Prentice, I. C. (1987). Description and simulation of tree-layer composition and size distributions in a primaeval Picea-Pinus forest. *Vegetatio*, 69(1):147–156.

Lenton, T. M., Held, H., Kriegler, E., Hall, J. W., Lucht, W., Rahmstorf, S., and Schellnhuber, H. J. (2008). Tipping elements in the Earth's climate system. *Proceedings of the National Academy of Sciences*, 105(6):1786–1793.

Leuning, R. (1995). A critical appraisal of a combined stomatal-photosynthesis model for C3 plants. *Plant, Cell & Environment*, 18(4):339–355.

Levine, N. M., Zhang, K., Longo, M., Baccini, A., Phillips, O. L., Lewis, S. L., Alvarez-Dávila, E., de Andrade, A. C. S., Brienen, R. J., Erwin, T. L., et al. (2016). Ecosystem heterogeneity determines the ecological resilience of the Amazon to climate change. *Proceedings of the National Academy of Sciences*, 113(3):793–797.

Lexerød, N. L. and Eid, T. (2006). An evaluation of different diameter diversity indices based on criteria related to forest management planning. *Forest Ecology and Management*, 222(1-3):17–28.

Li, W., MacBean, N., Ciais, P., Defourny, P., Lamarche, C., Bontemps, S., and Peng, S. (2019). Derivation of plant functional type (PFT) maps from the ESA CCI Land Cover product [Data set]. http://doi.org/10.5281/zenodo.1048163.

Lieberman, M., Lieberman, D., Peralta, R., and Hartshorn, G. S. (1995). Canopy closure and the distribution of tropical forest tree species at La Selva, Costa Rica. *Journal of Tropical Ecology*, 11(2):161–177.

Lines, E. R., Coomes, D. A., and Purves, D. W. (2010). Influences of forest structure, climate and species composition on tree mortality across the eastern US. *PLOS One*, 5(10):e13212.

Littleton, E. W., Harper, A. B., Vaughan, N. E., Oliver, R. J., Duran-Rojas, M. C., and Lenton, T. M. (2020). JULES-BE: representation of bioenergy crops and harvesting in the Joint UK land environment simulator vn5.1. *Geoscientific Model Development*, 13(3):1123–1136.

Liu, Y., Liu, R., Pisek, J., and Chen, J. M. (2017). Separating overstory and understory leaf area indices for global needleleaf and deciduous broadleaf forests by fusion of MODIS and MISR data. *Biogeosciences*, 14(5):1093–1110.

Lobo, E. and Dalling, J. (2013). Effects of topography, soil type and forest age on the frequency and size distribution of canopy gap disturbances in a tropical forest. *Biogeosciences*, 10(11):6769–6781.

Longo, M., Knox, R. G., Levine, N. M., Swann, A. L. S., Medvigy, D. M., Dietze, M. C., Kim, Y., Zhang, K., Bonal, D., Burban, B., Camargo, P. B., Hayek, M. N., Saleska, S. R., da Silva, R., Bras, R. L., Wofsy, S. C., and Moorcroft, P. R. (2019a). The biophysics, ecology, and biogeochemistry of functionally diverse, vertically and horizontally heterogeneous ecosystems: the ecosystem demography model, version 2.2 – part 2: Model evaluation for tropical south america. *Geoscientific Model Development*, 12(10):4347–4374.

Longo, M., Knox, R. G., Medvigy, D. M., Levine, N. M., Dietze, M. C., Kim, Y., Swann, A. L. S., Zhang, K., Rollinson, C. R., Bras, R. L., Wofsy, S. C., and Moorcroft, P. R. (2019b). The biophysics, ecology, and biogeochemistry of functionally diverse, vertically and horizontally heterogeneous ecosystems: the ecosystem demography model, version 2.2 – part 1: Model description. *Geoscientific Model Development*, 12(10):4309–4346.

Lu, R., Qiao, Y., Wang, J., Zhu, C., Cui, E., Xu, X., He, Y., Zhao, Z., Du, Y., Yan, L., et al. (2021). The U-shaped pattern of size-dependent mortality and

its correlated factors in a subtropical monsoon evergreen forest. *Journal of Ecology*, 109(6):2421–2433.

Lugo, A. E. and Scatena, F. N. (1996). Background and catastrophic tree mortality in tropical moist, wet, and rain forests. *Biotropica*, 28(4):585–599.

Lurton, T., Balkanski, Y., Bastrikov, V., Bekki, S., Bopp, L., Braconnot, P., Brockmann, P., Cadule, P., Contoux, C., Cozic, A., et al. (2020). Implementation of the CMIP6 Forcing Data in the IPSL-CM6A-LR Model. *Journal of Advances in Modeling Earth Systems*, 12(4):e2019MS001940.

Maltamo, M., Kangas, A., Uuttera, J., Torniainen, T., and Saramäki, J. (2000). Comparison of percentile based prediction methods and the Weibull distribution in describing the diameter distribution of heterogeneous Scots pine stands. *Forest Ecology and Management*, 133(3):263–274.

Manabe, S. (1969). Climate and the ocean circulation: I. The atmospheric circulation and the hydrology of the earth's surface. *Monthly Weather Review*, 97(11):739–774.

Manabe, S. and Wetherald, R. T. (1967). Thermal equilibrium of the atmosphere with a given distribution of relative humidity. *Journal of Atmospheric Sciences*, 24(3).

Manabe, S. and Wetherald, R. T. (1975). The effects of doubling the CO2 concentration on the climate of a general circulation model. *Journal of Atmospheric Sciences*, 32(1):3–15.

Mao, J., Wang, B., Dai, Y., Woodward, F., Hanson, P. J., and Lomas, M. (2007). Improvements of a dynamic global vegetation model and simulations of carbon and water at an upland-oak forest. *Advances in Atmospheric Sciences*, 24(2):311–322.

Martínez Cano, I., Shevliakova, E., Malyshev, S., Wright, S. J., Detto, M., Pacala, S. W., and Muller-Landau, H. C. (2020). Allometric constraints and competition enable the simulation of size structure and carbon fluxes in a dynamic vegetation model of tropical forests (LM3PPA-TV). *Global Change Biology*, 26(8):4478–4494.

Matthews, E. (1983). Global vegetation and land use: New high-resolution data bases for climate studies. *Journal of Applied Meteorology and Climatology*, 22(3):474–487.

McCarthy, H. R., Oren, R., Finzi, A. C., Ellsworth, D. S., Kim, H.-S., Johnsen, K. H., and Millar, B. (2007). Temporal dynamics and spatial variability in the enhancement of canopy leaf area under elevated atmospheric CO_2. *Global Change Biology*, 13(12):2479–2497.

McDowell, N. G., Beerling, D. J., Breshears, D. D., Fisher, R. A., Raffa, K. F., and Stitt, M. (2011). The interdependence of mechanisms underlying climate-driven vegetation mortality. *Trends in Ecology & Evolution*, 26(10):523–532.

McGill, B. J., Enquist, B. J., Weiher, E., and Westoby, M. (2006). Rebuilding community ecology from functional traits. *Trends in Ecology & Evolution*, 21(4):178–185.

McMahon, T. (1973). Size and shape in biology: elastic criteria impose limits on biological proportions, and consequently on metabolic rates. *Science*, 179(4079):1201–1204.

McMahon, T. A. and Kronauer, R. E. (1976). Tree structures: deducing the principle of mechanical design. *Journal of Theoretical Biology*, 59(2):443–466.

Medeiros, M. and Miranda, H. (2008). Post-fire resprouting and mortality in cerrado woody plant species over a three-year period. *Edinburgh Journal of Botany*, 65(1):53–68.

Medvigy, D., Wofsy, S., Munger, J., Hollinger, D., and Moorcroft, P. (2009). Mechanistic scaling of ecosystem function and dynamics in space and time: Ecosystem Demography model version 2. *Journal of Geophysical Research: Biogeosciences*, 114(G1).

Metcalfe, D. B., Meir, P., Aragão, L. E., Lobo-do Vale, R., Galbraith, D., Fisher, R., Chaves, M. M., Maroco, J., da Costa, A. C. L., de Almeida, S. S., et al. (2010). Shifts in plant respiration and carbon use efficiency at a large-scale drought experiment in the eastern Amazon. *New Phytologist*, 187(3):608–621.

Mitchell, K. J. (1975). Dynamics and simulated yieldof Douglas-fir. *Forest Science*, 21(suppl_1):a0001–z0001.

Monserud, R. A., Ledermann, T., and Sterba, H. (2004). Are self-thinning constraints needed in a tree-specific mortality model? *Forest Science*, 50(6):848–858.

Monsi, M. and Saeki, T. (1953). Uber den Lichtfaktor in den Pflanzengesellschaften und seine Bedeutung fur die Stoffproduktion. *Jap. Journ. Bot.*, 14:22–52.

Moorcroft, P. R., Hurtt, G. C., and Pacala, S. W. (2001). A method for scaling vegetation dynamics: the ecosystem demography model (ED). *Ecological Monographs*, 71(4):557–586.

Moore, J., Cox, P., Harper, A., and Sitch, S. (2013). R.E.D. Robust Ecosystem Demography Model. JULES Science Meeting 19-20th June 2013, University of Edinburgh.

Moore, J. R. (2016). *Aspects of Land Surface Modelling: Role of Biodiversity in Ecosystem Resilience to Environmental Change and a Robust Ecosystem Demography Model*. PhD thesis.

Moore, J. R., Argles, A. P., Zhu, K., Huntingford, C., and Cox, P. M. (2020). Validation of demographic equilibrium theory against tree-size distributions and biomass density in Amazonia. *Biogeosciences*, 17(4):1013–1032.

Moore, J. R., Zhu, K., Huntingford, C., and Cox, P. M. (2018). Equilibrium forest demography explains the distribution of tree sizes across North America. *Environmental Research Letters*, 13(8):084019.

Mrad, A., Manzoni, S., Oren, R., Vico, G., Lindh, M., and Katul, G. (2020). Recovering the metabolic, self-thinning, and constant final yield rules in mono-specific stands. *Frontiers in Forests and Global Change*, 3:62.

Muller-Landau, H. C., Condit, R. S., Chave, J., Thomas, S. C., Bohlman, S. A., Bunyavejchewin, S., Davies, S., Foster, R., Gunatilleke, S., Gunatilleke, N., et al. (2006). Testing metabolic ecology theory for allometric scaling of tree size, growth and mortality in tropical forests. *Ecology Letters*, 9(5):575–588.

Munro, D. D. (1974). Forest growth models-a prognosis. In *Growth models for tree and stand simulation*, volume 30, pages 7–21. Research Note 30. Department of Forest Yield Research, Royal College of Forestry.

Nabel, J. E., Naudts, K., and Pongratz, J. (2020). Accounting for forest age in the tile-based dynamic global vegetation model JSBACH4 (4.20 p7; git feature/forests)–a land surface model for the ICON-ESM. *Geoscientific Model Development*, 13(1):185–200.

Nakai, T., Sumida, A., Matsumoto, K., Daikoku, K., Iida, S., Park, H., Miyahara, M., Kodama, Y., Kononov, A. V., Maximov, T. C., et al. (2008). Aerodynamic scaling for estimating the mean height of dense canopies. *Boundary-layer Meteorology*, 128(3):423–443.

Nakashizuka, T., Katsuki, T., and Tanaka, H. (1995). Forest canopy structure analyzed by using aerial photographs. *Ecological Research*, 10(1):13–18.

Needham, J. F., Chambers, J., Fisher, R., Knox, R., and Koven, C. D. (2020). Forest responses to simulated elevated CO2 under alternate hypotheses of size-and age-dependent mortality. *Global Change Biology*, 26(10):5734–5753.

Neilson, R. P. (1995). A model for predicting continental-scale vegetation distribution and water balance. *Ecological Applications*, 5(2):362–385.

Neilson, R. P., Pitelka, L. F., Solomon, A. M., Nathan, R., Midgley, G. F., Fragoso, J. M., Lischke, H., and Thompson, K. (2005). Forecasting regional to global plant migration in response to climate change. *Bioscience*, 55(9):749–759.

Nelson, B. W., Kapos, V., Adams, J. B., Oliveira, W. J., and Braun, O. P. (1994). Forest disturbance by large blowdowns in the Brazilian Amazon. *Ecology*, 75(3):853–858.

Nepstad, D. C., Stickler, C. M., Filho, B. S., and Merry, F. (2008). Interactions among Amazon land use, forests and climate: prospects for a near-term forest tipping point. *Philosophical Transactions of the Royal Society B: Biological Sciences*, 363(1498):1737–1746.

Nepstad, D. C., Tohver, I. M., Ray, D., Moutinho, P., and Cardinot, G. (2007).

Mortality of large trees and lianas following experimental drought in an Amazon forest. *Ecology*, 88(9):2259–2269.

Niklas, K. J. and Enquist, B. J. (2001). Invariant scaling relationships for interspecific plant biomass production rates and body size. *Proceedings of the National Academy of Sciences*, 98(5):2922–2927.

Niklas, K. J. and Spatz, H.-C. (2004). Growth and hydraulic (not mechanical) constraints govern the scaling of tree height and mass. *Proceedings of the National Academy of Sciences*, 101(44):15661–15663.

O'Hagan, A. (2012). Probabilistic uncertainty specification: Overview, elaboration techniques and their application to a mechanistic model of carbon flux. *Environmental Modelling & Software*, 36:35–48.

Okubu, A. et al. (1982). Diffusion and ecological problems: mathematical models. *Biometrical Journal*, 24(3):272–272.

Oliver, T. H., Brereton, T., and Roy, D. B. (2013). Population resilience to an extreme drought is influenced by habitat area and fragmentation in the local landscape. *Ecography*, 36(5):579–586.

Olivero, J., Fa, J. E., Real, R., Márquez, A. L., Farfán, M. A., Vargas, J. M., Gaveau, D., Salim, M. A., Park, D., Suter, J., et al. (2017). Recent loss of closed forests is associated with Ebola virus disease outbreaks. *Scientific Reports*, 7(1):1–9.

Olson, J. S., Watts, J. A., and Allison, L. J. (1985). Major world ecosystem complexes ranked by carbon in live vegetation: A database. Technical report, Oak Ridge National Lab., TN (USA).

Oswalt, S. N., Smith, W. B., Miles, P. D., and Pugh, S. A. (2014). Forest Resources of the United States, 2012: a technical document supporting the Forest Service 2010 update of the RPA Assessment. *Gen. Tech. Rep. Wo-91. Washington, Dc: Us Department of Agriculture, Forest Service, Washington Office. 218 P.*, 91.

Overpeck, J. T., Rind, D., and Goldberg, R. (1990). Climate-induced changes in forest disturbance and vegetation. *Nature*, 343(6253):51–53.

Pacala, S. W., Canham, C. D., and Silander Jr, J. A. (1993). Forest models defined by field measurements: I. The design of a northeastern forest simulator. *Canadian Journal of Forest Research*, 23(10):1980–1988.

Pach, M. and Podlaski, R. (2015). Tree diameter structural diversity in Central European forests with Abies alba and Fagus sylvatica: managed versus unmanaged forest stands. *Ecological Research*, 30(2):367–384.

Pavlick, R., Drewry, D. T., Bohn, K., Reu, B., and Kleidon, A. (2013). The Jena Diversity-Dynamic Global Vegetation Model (JeDi-DGVM): a diverse approach to representing terrestrial biogeography and biogeochemistry based on plant functional trade-offs. *Biogeosciences*, 10(6):4137–4177.

Peacock, J., Baker, T., Lewis, S., Lopez-Gonzalez, G., and Phillips, O. (2007). The RAINFOR database: monitoring forest biomass and dynamics. *Journal of Vegetation Science*, 18(4):535–542.

Peng, C. (2000). From static biogeographical model to dynamic global vegetation model: a global perspective on modelling vegetation dynamics. *Ecological Modelling*, 135(1):33–54.

Perry, D. A. (1984). A model of physiological and allometric factors in the self-thinning curve. *Journal of Theoretical Biology*, 106(3):383–401.

Perry, D. A. and Borchers, J. G. (1990). Climate change and ecosystem responses. *Northwest Environ. J.*, 6(2):293–313.

Peterson, D. W. and Reich, P. B. (2001). Prescribed fire in oak savanna: fire frequency effects on stand structure and dynamics. *Ecological Applications*, 11(3):914–927.

Phillips, N. A. (1956). The general circulation of the atmosphere: A numerical experiment. *Quarterly Journal of the Royal Meteorological Society*, 82(352):123–164.

Phillips, O. L. (1996). Long-term environmental change in tropical forests: increasing tree turnover. *Environmental Conservation*, 23(3):235–248.

Phillips, O. L., Baker, T. R., Arroyo, L., Higuchi, N., Killeen, T. J., Laurance, W. F., Lewis, S. L., Lloyd, J., Malhi, Y., Monteagudo, A., et al. (2004). Pattern and

process in Amazon tree turnover, 1976–2001. *Philosophical Transactions of the Royal Society of London. Series B: Biological Sciences*, 359(1443):381–407.

Poulter, B., MacBean, N., Hartley, A., Khlystova, I., Arino, O., Betts, R., Bontemps, S., Boettcher, M., Brockmann, C., Defourny, P., et al. (2015). Plant functional type classification for earth system models: results from the European Space Agency's Land Cover Climate Change Initiative. *Geoscientific Model Development*, 8(7):2315–2328.

Powers, J. S., Becknell, J. M., Irving, J., and Perez-Aviles, D. (2009). Diversity and structure of regenerating tropical dry forests in Costa Rica: Geographic patterns and environmental drivers. *Forest Ecology and Management*, 258(6):959–970.

Prentice, I. C., Cramer, W., Harrison, S. P., Leemans, R., Monserud, R. A., and Solomon, A. M. (1992). Special paper: a global biome model based on plant physiology and dominance, soil properties and climate. *Journal of Biogeography*, 19(2):117–134.

Prentice, I. C., Liang, X., Medlyn, B. E., and Wang, Y.-P. (2015). Reliable, robust and realistic: the three R's of next-generation land-surface modelling. *Atmospheric Chemistry and Physics*, 15(10):5987–6005.

Prentice, I. C., Sykes, M. T., and Cramer, W. (1991). The possible dynamic response of northern forests to global warming. *Global Ecology and Biogeography Letters*, 1(5):129–135.

Pretzsch, H. (2006). Species-specific allometric scaling under self-thinning: evidence from long-term plots in forest stands. *Oecologia*, 146(4):572–583.

Prior, L. D., Murphy, B. P., and Russell-Smith, J. (2009). Environmental and demographic correlates of tree recruitment and mortality in north Australian savannas. *Forest Ecology and Management*, 257(1):66–74.

Pugh, T. A., Rademacher, T., Shafer, S. L., Steinkamp, J., Barichivich, J., Beckage, B., Haverd, V., Harper, A., Heinke, J., Nishina, K., et al. (2020). Understanding the uncertainty in global forest carbon turnover. *Biogeosciences*, 17(15):3961–3989.

Purves, D. W., Lichstein, J. W., Strigul, N., and Pacala, S. W. (2008). Predicting and understanding forest dynamics using a simple tractable model. *Proceedings of the National Academy of Sciences*, 105(44):17018–17022.

Quillet, A., Peng, C., and Garneau, M. (2010). Toward dynamic global vegetation models for simulating vegetation–climate interactions and feedbacks: recent developments, limitations, and future challenges. *Environmental Reviews*, 18(NA):333–353.

Ramankutty, N. and Foley, J. A. (1999). Estimating historical changes in global land cover: Croplands from 1700 to 1992. *Global Biogeochemical Cycles*, 13(4):997–1027.

Reich, P. B., Tjoelker, M. G., Machado, J.-L., and Oleksyn, J. (2006). Universal scaling of respiratory metabolism, size and nitrogen in plants. *Nature*, 439(7075):457–461.

Reick, C., Raddatz, T., Brovkin, V., and Gayler, V. (2013). Representation of natural and anthropogenic land cover change in MPI-ESM. *Journal of Advances in Modeling Earth Systems*, 5(3):459–482.

Reineke, L. H. (1933). Perfection a stand-density index for even-aged forest. *Journal of Agricultural Research*, 46:627–638.

Reu, B., Proulx, R., Bohn, K., Dyke, J. G., Kleidon, A., Pavlick, R., and Schmidtlein, S. (2011). The role of climate and plant functional trade-offs in shaping global biome and biodiversity patterns. *Global Ecology and Biogeography*, 20(4):570–581.

Reynolds, J. H. and Ford, E. D. (2005). Improving competition representation in theoretical models of self-thinning: a critical review. *Journal of Ecology*, 93(2):362–372.

Ribbens, E., Silander Jr, J. A., and Pacala, S. W. (1994). Seedling recruitment in forests: calibrating models to predict patterns of tree seedling dispersion. *Ecology*, 75(6):1794–1806.

Rothermel, R. C. (1983). *How to predict the spread and intensity of forest and*

range fires, volume 143. US Department of Agriculture, Forest Service, Intermountain Forest and Range Experiment Station.

Roussin, N. (1949). L'evolution des theories phytosociologiques en Russie. *Vegetatio*, 1(2/3):175–183.

Rowland, L., da Costa, A. C. L., Galbraith, D. R., Oliveira, R., Binks, O. J., Oliveira, A., Pullen, A., Doughty, C. E., Metcalfe, D., Vasconcelos, S. S., et al. (2015). Death from drought in tropical forests is triggered by hydraulics not carbon starvation. *Nature*, 528(7580):119–122.

Rüger, N. and Condit, R. (2012). Testing metabolic theory with models of tree growth that include light competition. *Functional Ecology*, 26(3):759–765.

Running, S., Mu, Q., and Zhao, M. (2015). MOD17A3 MODIS/Terra gross primary productivity yearly L4 global 1 km SIN Grid. *NASA LP DAAC*.

Saatchi, S. S., Harris, N. L., Brown, S., Lefsky, M., Mitchard, E. T., Salas, W., Zutta, B. R., Buermann, W., Lewis, S. L., Hagen, S., et al. (2011). Benchmark map of forest carbon stocks in tropical regions across three continents. *Proceedings of the National Academy of Sciences*, 108(24):9899–9904.

Sahney, S., Benton, M. J., and Falcon-Lang, H. J. (2010). Rainforest collapse triggered Carboniferous tetrapod diversification in Euramerica. *Geology*, 38(12):1079–1082.

Sakschewski, B., von Bloh, W., Boit, A., Rammig, A., Kattge, J., Poorter, L., Peñuelas, J., and Thonicke, K. (2015). Leaf and stem economics spectra drive diversity of functional plant traits in a dynamic global vegetation model. *Global Change Biology*, 21(7):2711–2725.

Saravia, L. A., Doyle, S. R., and Bond-Lamberty, B. (2018). Power laws and critical fragmentation in global forests. *Scientific Reports*, 8(1):1–12.

Sato, H. (2009). Simulation of the vegetation structure and function in a Malaysian tropical rain forest using the individual-based dynamic vegetation model SEIB-DGVM. *Forest Ecology and Management*, 257(11):2277–2286.

Sato, H. and Ise, T. (2012). Effect of plant dynamic processes on African vegetation responses to climate change: Analysis using the spatially explicit

individual-based dynamic global vegetation model (SEIB-DGVM). *Journal of Geophysical Research: Biogeosciences*, 117(G3).

Sato, H., Itoh, A., and Kohyama, T. (2007). SEIB–DGVM: A new Dynamic Global Vegetation Model using a spatially explicit individual-based approach. *Ecological Modelling*, 200(3-4):279–307.

Sato, H., Kobayashi, H., and Delbart, N. (2010). Simulation study of the vegetation structure and function in eastern Siberian larch forests using the individual-based vegetation model SEIB-DGVM. *Forest Ecology and Management*, 259(3):301–311.

Scheiter, S. and Higgins, S. I. (2009). Impacts of climate change on the vegetation of Africa: an adaptive dynamic vegetation modelling approach. *Global Change Biology*, 15(9):2224–2246.

Scheiter, S., Langan, L., and Higgins, S. I. (2013). Next-generation dynamic global vegetation models: learning from community ecology. *New Phytologist*, 198(3):957–969.

Sellar, A. A., Jones, C. G., Mulcahy, J. P., Tang, Y., Yool, A., Wiltshire, A., O'connor, F. M., Stringer, M., Hill, R., Palmieri, J., et al. (2019). UKESM1: Description and evaluation of the UK Earth System Model. *Journal of Advances in Modeling Earth Systems*, 11(12):4513–4558.

Sellers, P. and Dorman, J. (1987). Testing the simple biosphere model (SiB) using point micrometeorological and biophysical data. *Journal of Applied Meteorology and Climatology*, 26(5):622–651.

Seydack, A. H., Durrheim, G., and Louw, J. H. (2011). Spatiotemporally interactive growth dynamics in selected South African forests: Edaphoclimatic environment, crowding and climate effects. *Forest Ecology and Management*, 261(7):1152–1169.

Shante, V. K. and Kirkpatrick, S. (1971). An introduction to percolation theory. *Advances in Physics*, 20(85):325–357.

Sheil, D. and May, R. M. (1996). Mortality and recruitment rate evaluations in heterogeneous tropical forests. *Journal of Ecology*, 84(1):91–100.

Shevliakova, E., Malyshev, S., Martinez-Cano, I., Milly, P., Pacala, S., Ginoux, P., Dunne, K., Dunne, J., Dupius, C., Findell, K., et al. (2020). The land component LM4. 1 of the GFDL Earth System Model ESM4. 1: biophysical and biogeochemical processes and interactions with climate. *J. Adv. Model. Earth Syst., 2019ms002040, in Review*.

Shevliakova, E., Pacala, S. W., Malyshev, S., Hurtt, G. C., Milly, P., Caspersen, J. P., Sentman, L. T., Fisk, J. P., Wirth, C., and Crevoisier, C. (2009). Carbon cycling under 300 years of land use change: Importance of the secondary vegetation sink. *Global Biogeochemical Cycles*, 23(2).

Short, K. C. (2017). Spatial wildfire occurrence data for the United States, 1992-2015 [FPA_FOD_20170508].

Shugart, H., Foster, A., Wang, B., Druckenbrod, D., Ma, J., Lerdau, M., Saatchi, S., Yang, X., and Yan, X. (2020). Gap models across micro-to mega-scales of time and space: examples of Tansley's ecosystem concept. *Forest Ecosystems*, 7(1):1–18.

Shugart, H. and Smith, T. (1996). A review of forest patch models and their application to global change research. *Climatic Change*, 34(2):131–153.

Shugart, H. H. and West, D. C. (1981). Long-term dynamics of forest ecosystems: Computer simulation models, which allow for numerous seedlings and the long lives of large trees, predict how forests will respond to different management techniques. *American Scientist*, 69(6):647–652.

Shukla, P., Skea, J., Calvo Buendia, E., Masson-Delmotte, V., Pörtner, H., Roberts, D., Zhai, P., Slade, R., Connors, S., Van Diemen, R., et al. (2019). IPCC, 2019: Climate Change and Land: an IPCC special report on climate change, desertification, land degradation, sustainable land management, food security, and greenhouse gas fluxes in terrestrial ecosystems.

Sitch, S., Huntingford, C., Gedney, N., Levy, P., Lomas, M., Piao, S., Betts, R., Ciais, P., Cox, P., Friedlingstein, P., et al. (2008). Evaluation of the terrestrial carbon cycle, future plant geography and climate-carbon cycle feedbacks using five Dynamic Global Vegetation Models (DGVMs). *Global Change Biology*, 14(9):2015–2039.

Sitch, S., Smith, B., Prentice, I. C., Arneth, A., Bondeau, A., Cramer, W., Kaplan, J. O., Levis, S., Lucht, W., Sykes, M. T., et al. (2003). Evaluation of ecosystem dynamics, plant geography and terrestrial carbon cycling in the LPJ dynamic global vegetation model. *Global Change Biology*, 9(2):161–185.

Smith, B. (2001). LPJ-GUESS-an ecosystem modelling framework. *Department of Physical Geography and Ecosystems Analysis, Ines, Sölvegatan*, 12:22362.

Smith, T., Shugart, H., Woodward, F., and Burton, P. (1993). Plant functional types. In *Vegetation Dynamics & Global Change*, pages 272–292. Springer.

Smith, T. M. and Shugart, H. (1993). The transient response of terrestrial carbon storage to a perturbed climate. *Nature*, 361(6412):523–526.

Snell, R. S., Huth, A., Nabel, J. E., Bocedi, G., Travis, J. M., Gravel, D., Bugmann, H., Gutiérrez, A. G., Hickler, T., Higgins, S. I., et al. (2014). Using dynamic vegetation models to simulate plant range shifts. *Ecography*, 37(12):1184–1197.

Solé, R. V. and Manrubia, S. C. (1995). Are rainforests self-organized in a critical state? *Journal of Theoretical Biology*, 173(1):31–40.

Spies, T. A., Hemstrom, M. A., Youngblood, A., and Hummel, S. (2006). Conserving old-growth forest diversity in disturbance-prone landscapes. *Conservation Biology*, 20(2):351–362.

Sprintsin, M., Karnieli, A., Sprintsin, S., Cohen, S., and Berliner, P. (2009). Relationships between stand density and canopy structure in a dryland forest as estimated by ground-based measurements and multi-spectral spaceborne images. *Journal of Arid Environments*, 73(10):955–962.

Staal, A., Fetzer, I., Wang-Erlandsson, L., Bosmans, J. H., Dekker, S. C., van Nes, E. H., Rockström, J., and Tuinenburg, O. A. (2020). Hysteresis of tropical forests in the 21st century. *Nature Communications*, 11(1):1–8.

Stark, S. C., Enquist, B. J., Saleska, S. R., Leitold, V., Schietti, J., Longo, M., Alves, L. F., Camargo, P. B., and Oliveira, R. C. (2015). Linking canopy leaf area and light environments with tree size distributions to explain Amazon forest demography. *Ecology Letters*, 18(7):636–645.

Staver, A. C., Bond, W. J., Stock, W. D., Van Rensburg, S. J., and Waldram, M. S. (2009). Browsing and fire interact to suppress tree density in an African savanna. *Ecological Applications*, 19(7):1909–1919.

Staver, A. C., Brando, P. M., Barlow, J., Morton, D. C., Paine, C. T., Malhi, Y., Araujo Murakami, A., and del Aguila Pasquel, J. (2020). Thinner bark increases sensitivity of wetter Amazonian tropical forests to fire. *Ecology Letters*, 23(1):99–106.

Stocker, B. D., Feissli, F., Strassmann, K. M., Spahni, R., and Joos, F. (2014). Past and future carbon fluxes from land use change, shifting cultivation and wood harvest. *Tellus B: Chemical and Physical Meteorology*, 66(1):23188.

Stovall, A. E., Shugart, H., and Yang, X. (2019). Tree height explains mortality risk during an intense drought. *Nature Communications*, 10(1):1–6.

Strigul, N., Pristinski, D., Purves, D., Dushoff, J., and Pacala, S. (2008). Scaling from trees to forests: tractable macroscopic equations for forest dynamics. *Ecological Monographs*, 78(4):523–545.

Suarez, M. L. and Kitzberger, T. (2008). Recruitment patterns following a severe drought: long-term compositional shifts in Patagonian forests. *Canadian Journal of Forest Research*, 38(12):3002–3010.

Svenning, J.-C. and Skov, F. (2007). Could the tree diversity pattern in Europe be generated by postglacial dispersal limitation? *Ecology Letters*, 10(6):453–460.

Swaine, M. (1992). Characteristics of dry forest in West Africa and the influence of fire. *Journal of Vegetation Science*, 3(3):365–374.

Tansley, A. G. (1935). The use and abuse of vegetational concepts and terms. *Ecology*, 16(3):284–307.

Taubert, F., Fischer, R., Groeneveld, J., Lehmann, S., Müller, M. S., Rödig, E., Wiegand, T., and Huth, A. (2018). Global patterns of tropical forest fragmentation. *Nature*, 554(7693):519–522.

Thonicke, K., Venevsky, S., Sitch, S., and Cramer, W. (2001). The role of fire disturbance for global vegetation dynamics: coupling fire into a Dynamic Global Vegetation Model. *Global Ecology and Biogeography*, 10(6):661–677.

Trucco, E. (1965). Mathematical models for cellular systems the von Foerster equation. Part I. *The Bulletin of Mathematical Biophysics*, 27(3):285–304.

Trugman, A., Fenton, N., Bergeron, Y., Xu, X., Welp, L., and Medvigy, D. (2016). Climate, soil organic layer, and nitrogen jointly drive forest development after fire in the North American boreal zone. *Journal of Advances in Modeling Earth Systems*, 8(3):1180–1209.

Valbuena, R., Eerikäinen, K., Packalen, P., and Maltamo, M. (2016). Gini coefficient predictions from airborne lidar remote sensing display the effect of management intensity on forest structure. *Ecological Indicators*, 60:574–585.

Van Der Maarel, E. (1996). Pattern and process in the plant community: Fifty years after AS Watt. *Journal of Vegetation Science*, 7(1):19–28.

Van Nieuwstadt, M. G. and Sheil, D. (2005). Drought, fire and tree survival in a Borneo rain forest, East Kalimantan, Indonesia. *Journal of Ecology*, 93(1):191–201.

Van Sickle, J. (1977). Analysis of a distributed-parameter population model based on physiological age. *Journal of Theoretical Biology*, 64(3):571–586.

Van Uytvanck, J., Maes, D., Vandenhaute, D., and Hoffmann, M. (2008). Restoration of woodpasture on former agricultural land: the importance of safe sites and time gaps before grazing for tree seedlings. *Biological Conservation*, 141(1):78–88.

Van Wilgen, B., Biggs, H., O'regan, S., and Mare, N. (2000). Fire history of the savanna ecosystems in the Kruger National Park, South Africa, between 1941 and 1996. *South African Journal of Science*, 96(4):167–178.

von Foerster, H. (1959). Some remarks on changing populations. *The Kinetics of Cellular Proliferation, Grune and Stratton*, pages 382–407.

Waldrop, T., Buckner, E., Shugart Jr, H., and McGee, C. (1986). FORCAT: a single tree model of stand development following clearcutting on the Cumberland Plateau. *Forest Science*, 32(2):297–317.

Wang, Y., Weinacker, H., and Koch, B. (2008). A lidar point cloud based procedure for vertical canopy structure analysis and 3D single tree modelling in forest. *Sensors*, 8(6):3938–3951.

Watanabe, S., Hajima, T., Sudo, K., Nagashima, T., Takemura, T., Okajima, H., Nozawa, T., Kawase, H., Abe, M., Yokohata, T., et al. (2011). MIROC-ESM 2010: Model description and basic results of CMIP5-20c3m experiments. *Geoscientific Model Development*, 4(4):845–872.

Watt, A. S. (1947). Pattern and process in the plant community. *Journal of Ecology*, 35(1/2):1–22.

Weiner, J. and Solbrig, O. T. (1984). The meaning and measurement of size hierarchies in plant populations. *Oecologia*, 61(3):334–336.

Weiskittel, A. R., Hann, D. W., Kershaw Jr, J. A., and Vanclay, J. K. (2011). *Forest growth and yield modeling*. John Wiley & Sons.

Weng, E., Malyshev, S., Lichstein, J., Farrior, C. E., Dybzinski, R., Zhang, T., Shevliakova, E., and Pacala, S. W. (2015). Scaling from individual trees to forests in an Earth system modeling framework using a mathematically tractable model of height-structured competition. *Biogeosciences*, 12(9):2655–2694.

West, G. B., Brown, J. H., and Enquist, B. J. (1997). A general model for the origin of allometric scaling laws in biology. *Science*, 276(5309):122–126.

West, G. B., Enquist, B. J., and Brown, J. H. (2009). A general quantitative theory of forest structure and dynamics. *Proceedings of the National Academy of Sciences*, 106(17):7040–7045.

Westoby, M. (1984). The self-thinning rule. *Advances in Ecological Research*, 14:167–225.

Whittaker, R. H. (1953). A consideration of climax theory: the climax as a population and pattern. *Ecological Monographs*, 23(1):41–78.

Wigley, T., Briffa, K., and Jones, P. (1984). Atmospheric carbon dioxide: Predicting plant productivity and water resources. *Nature*, 312(5990):102–103.

Williams, A. P., Allen, C. D., Macalady, A. K., Griffin, D., Woodhouse, C. A., Meko, D. M., Swetnam, T. W., Rauscher, S. A., Seager, R., Grissino-Mayer, H. D., et al. (2013). Temperature as a potent driver of regional forest drought stress and tree mortality. *Nature Climate Change*, 3(3):292–297.

Wilson, C. L. and Matthews, W. H. (1971). Inadvertent Climate Modification. Report of Conference, Study of Man's Impact on Climate (SMIC).

Woodward, F. and Lomas, M. (2004). Vegetation dynamics–simulating responses to climatic change. *Biological Reviews*, 79(3):643–670.

Woodward, F., Lomas, M. R., and Betts, R. A. (1998). Vegetation-climate feedbacks in a greenhouse world. *Philosophical Transactions of the Royal Society of London. Series B: Biological Sciences*, 353(1365):29–39.

Wright, D. K. (2017). Humans as agents in the termination of the African Humid Period. *Frontiers in Earth Science*, 5:4.

Wu, D., Piao, S., Liu, Y., Ciais, P., and Yao, Y. (2018). Evaluation of CMIP5 earth system models for the spatial patterns of biomass and soil carbon turnover times and their linkage with climate. *Journal of Climate*, 31(15):5947–5960.

Wu, L., Kato, T., Sato, H., Hirano, T., and Yazaki, T. (2019). Sensitivity analysis of the typhoon disturbance effect on forest dynamics and carbon balance in the future in a cool-temperate forest in northern Japan by using SEIB-DGVM. *Forest Ecology and Management*, 451:117529.

Xiao, X., McGlinn, D. J., and White, E. P. (2015). A strong test of the maximum entropy theory of ecology. *The American Naturalist*, 185(3):E70–E80.

Xu, X., Medvigy, D., Powers, J. S., Becknell, J. M., and Guan, K. (2016). Diversity in plant hydraulic traits explains seasonal and inter-annual variations of vegetation dynamics in seasonally dry tropical forests. *New Phytologist*, 212(1):80–95.

Yoda, K. (1963). Self-thinning in overcrowded pure stands under cultivated and natural conditions (Intraspecific competition among higher plants. XI). *J. Inst. Polytech. Osaka City Univ. Ser. D.*, 14:107–129.

Yue, C., Ciais, P., Luyssaert, S., Li, W., McGrath, M. J., Chang, J., and Peng, S. (2018). Representing anthropogenic gross land use change, wood harvest,

and forest age dynamics in a global vegetation model ORCHIDEE-MICT v8. 4.2. *Geoscientific Model Development*, 11(1):409–428.

Zaehle, S., Sitch, S., Smith, B., and Hatterman, F. (2005). Effects of parameter uncertainties on the modeling of terrestrial biosphere dynamics. *Global Biogeochemical Cycles*, 19(3).

Zemp, D. C., Schleussner, C.-F., Barbosa, H. M., Hirota, M., Montade, V., Sampaio, G., Staal, A., Wang-Erlandsson, L., and Rammig, A. (2017). Self-amplified Amazon forest loss due to vegetation-atmosphere feedbacks. *Nature Communications*, 8(1):1–10.

Zeng, N. (2003). Glacial-interglacial atmospheric CO 2 change—The glacial burial hypothesis. *Advances in Atmospheric Sciences*, 20(5):677–693.

Zeng, N., Qian, H., Munoz, E., and Iacono, R. (2004). How strong is carbon cycle-climate feedback under global warming? *Geophysical Research Letters*, 31(20).

Zhang, K., de Almeida Castanho, A. D., Galbraith, D. R., Moghim, S., Levine, N. M., Bras, R. L., Coe, M. T., Costa, M. H., Malhi, Y., Longo, M., et al. (2015). The fate of Amazonian ecosystems over the coming century arising from changes in climate, atmospheric CO 2, and land use. *Global Change Biology*, 21(7):2569–2587.

Zhang, L. and Liu, C. (2006). Fitting irregular diameter distributions of forest stands by Weibull, modified Weibull, and mixture Weibull models. *Journal of Forest Research*, 11(5):369–372.

Zhang, W.-P., Jia, X., Bai, Y.-Y., and Wang, G.-X. (2011). The difference between above-and below-ground self-thinning lines in forest communities. *Ecological Research*, 26(4):819–825.

Zhou, J. and Lin, G. (2018). Will forest size structure follow the- 2 power-law distribution under ideal demographic equilibrium state? *Journal of Theoretical Biology*, 452:17–21.

Zuleta, D., Duque, A., Cardenas, D., Muller-Landau, H. C., and Davies, S. J.

(2017). Drought-induced mortality patterns and rapid biomass recovery in a terra firme forest in the Colombian Amazon. *Ecology*, 98(10):2538–2546.